UNIVERSITY OF SOUTHAMPTON

FACULTY OF ENGINEERING AND THE ENVIRONMENT

Aerodynamics and Flight Mechanics

Improving Wind Turbine Aerodynamic Performance Using Iterative Learning Control Applied To Smart Rotors

by

Mark W. Blackwell

Thesis for the degree of Doctor of Philosophy

October 2015

ABSTRACT

Currently there is significant research into the inclusion of localised active flow control on wind turbine rotor blades, with the aim, in conjunction with collective and individual pitch control, of improving the aerodynamic performance of the rotor. These blades are termed smart rotors. The unique contribution of this research is the application of Iterative Learning Control to wind turbine smart rotors to reduce blade loading from lift disturbances. The smart devices act locally, at different spanwise positions, and include actuation to manipulate local lift (e.g. trailing edge flaps, blowing/suction, circulation control); sensing to determine the current turbine loading (e.g. pressure sensors, strain gauges, LIDAR); and a suitable control scheme to achieve predefined objectives. The principal objective is to reduce fatigue loads, although mitigating the effects of extreme loads is also of interest. The reduction of these loads leads to lighter, larger and more reliable turbines. Traditionally blade loads have been managed using stall regulation, pitch control, torque control or a combination of all three. Smart rotors are an evolutionary step in the control of turbines and have the advantage of deploying variable control along the blade with quicker response times to variations in flow conditions, leading to a potential increase in energy production, an increase in turbine reliability and a reduced energy requirements. The aerodynamic loads on a wind turbine blade have periodic and non-periodic components, and the nature of these strongly suggests the application of iterative learning control. The research within this PhD thesis employs a 2D computational fluid dynamics model (vortex panel method), with nonlinear wake effects, to represent flow past an aerofoil. The CFD model uses a potential flow approximation which is valid for inviscid and attached flow only. This is acceptable because smart devices typically operate under such conditions. Circulation control (actuation) and pressure sensors (load sensing) are modelled to represent a 2D section of a smart rotor. The model is used in conjunction with a first-order lag actuator model to undertake a detailed investigation into the level of control possible by, as in other areas, combining iterative learning control with classical control action with emphasis on how performance can be effectively measured. Typical turbine flow regimes are simulated by generating multiple upstream vortices, drifting turbine time periods, stochastic inflow conditions and a combination of all three regimes. Results indicate that cyclical and stochastic loadings on turbine blades can be effectively managed using Iterative Learning Control, with significant reductions in both fatigue and extreme loads for a range of flow conditions.

Contents

List of Figures

List of Tables

Declaration of Authorship

I, Mark W. Blackwell , declare that the thesis entitled *Improving Wind Turbine Aerodynamic Performance Using Iterative Learning Control Applied To Smart Rotors* and the work presented in the thesis are both my own, and have been generated by me as the result of my own original research. I confirm that:

- this work was done wholly or mainly while in candidature for a research degree at this University;
- where any part of this thesis has previously been submitted for a degree or any other qualification at this University or any other institution, this has been clearly stated;
- where I have consulted the published work of others, this is always clearly attributed;
- where I have quoted from the work of others, the source is always given. With the exception of such quotations, this thesis is entirely my own work;
- I have acknowledged all main sources of help;
- where the thesis is based on work done by myself jointly with others, I have made clear exactly what was done by others and what I have contributed myself;
- parts of this work have been published as: (Tutty, 2014) and (Blackwell, 2015)

Signed:.....

Date:.....

Acknowledgements

I would like to thank my two primary supervisors Professor Owen Tutty and Professor Richard Sandberg for their ongoing support throughout the PhD and helping me advance my knowledge in a fascinating subject. Also to Eric Rogers in helping inspire some the objectives of the work. Vestas Wind Systems A/S for providing the initial opportunity to undertake the study. Finally, thanks to family and friends who have helped me along the way.

Nomenclature

α	Angle of attack (degrees)
Δ	Small time step
Δ_i	Length of panel i
Ω	Angular velocity (rad/s)
μ	controller gain
μ_0	Phase-lead ILC controller gain
μ_1	P-type ILC controller gain
ν_a	Tangential velocity above the upper trailing edge panel
ν_b	Tangential velocity above the lower trailing edge panel
Γ	Aerofoil circulation
Γ_j	Strength of vortex j
κ	Source panel strength
λ_i	Vortex panel strength
σ	Standard deviation
A	Amplitude of oscillation
$C_{s,p}$	Coefficient between the global lift and the pressure difference $p_s - p_p$
E^k	Error at time step k
H	Airfoil chord
i	Panel number
j	Cycle number
k	Time step $(= jN_c + k_c)$
k_c	Time step within a cycle
L^k	Direct lift at time step k
L_e^k	Estimated lift at time step k
L_r	Target lift
$\mathcal{L}_2$	two norm performance measure
$\mathcal{L}_\infty$	infinity norm performance measure
M	Number of discrete vortices
nt	Maximum number of time steps
N_c	Number of time steps within a period $(= T/\Delta t)$
N	Number of vortex/source panels

p_s	Pressure at sensor on suction side
p_p	Pressure at sensor on pressure side
Q	Number of pressure sensors
r	Radial position along blade (m)
$r_{pL}[i]$	Pearsons correlation factor between panel i pressure and global lift
Δt	time step
t^*	Dimensional time
t	non-dimensional time
T	Period of oscillation
T_0	Lower limit of $\mathcal{L}_2$ integration
T_1	Upper limit of $\mathcal{L}_2$ integration
u^k	Control at time step k
$\hat{u}$	Phase-lead ILC control input
$\bar{u}$	P-type ILC control input
$v(x,t)$	Velocity generated by the freestream
v^*	Dimensional velocity with components v_x and v_y
$v_p(x,t)$	Velocity field generated by the vortex and source panels
$v_\nu(x,t)$	Velocity field generated by the vortices
V_{rel}	Relative velocity onto blade section
V_∞	Mean reestream velocity
V_{0x}	Freestream velocity at time t
V_x	Turbine axial velocity
x_{v1}	Start location of vortex 1
x_{v2}	Start location of vortex 2

AoA	Angle of attack
ACW	Active Compliant Wing
BEM	Blade Element Method
CFD	Computational Fluid Dynamics
DES	Detached eddy simulation
DNS	Direct numerical simulation
DS	Delay Stall
DTEG	Deformable Trailing Edge Geometry
ILC	Iterative learning control
LE	Leading Edge
LES	Large eddy simulation
NS	Navier Stokes
PID	Proportional, integral, differential
RANS	Reynolds averaged Navier Stokes
RLC	Repetitive Learning Control
TE	Trailing Edge

URANS	Unsteady Reynolds Averaged Navier Stokes
VPM	Vortex panel method

Chapter 1

Introduction

1.1 Overview

The cost of energy is always the driving factor in wind turbine design. Cost of energy is defined as the total lifecycle cost (manufacture, transportation, installation, operation, disposal) divided by the total energy capture over the life of the machine. Figures vary widely depending on the factors considered but a levelised cost reference is given in MacDonald (2010) where offshore wind is estimated at £160/MWh; onshore wind at £93/MWh; coal (with carbon capture and storage) at £150/MWh; gas (with carbon capture and storage) at £80/MWh; and nuclear at £99/MWh. Turbines are now manufactured with power ratings of 7MW (∼80m blade length) and designs for 15MW+ turbines are being considered for the offshore environment. These ever increasing rotor sizes are due to the fact that power output is proportional to the swept area and the cube of the velocity. Increasing the rotor size, in combination with the more consistent winds at sea and increased planning restrictions onshore, is leading to turbines becoming more popular offshore. The environment offshore is very harsh and maintenance costs are high. This has led to an increased focus on improving the reliability of turbines, in conjunction with improved energy capture.

A large percentage of the failures on a turbine are associated with the transmitted loads from the blades. The theory is that if the fatigue and extreme loads on the blades can be managed more effectively, then the maintenance requirements will reduce. The blade loads are a direct consequence of the aerodynamic loading, therefore manipulating the aerodynamics of the blade results in control over the loads experienced by the system. Existing production turbines take advantage of collective pitch control (Wright, 2004) and individual pitch control to manage the loads (Thomsen et al., 2008). This method has shown some success but the systems suffer from slow actuation and the lack of ability to mitigate against spanwise load variations. The concept of the smart rotor has been introduced as a remedy to this problem. The idea is to manipulate the lift

Figure 1.1: Impression of wind turbine smart rotor with trailing edge flaps (TuDelft, 2012)

at different positions along the blades to meet set control objectives (e.g. reduce loads, increase power). Methods of controlling the local lift are vast and much can be learnt from the aircraft and rotorcraft industries (Straub, 1996). The most obvious smart rotor actuation method, which is already in use on aircraft wings and helicopter blades, is the use of trailing edge flaps, as shown in Figure 1.1.

Load reduction for reduced maintenance and increased component lifespan is probably the driving force behind the smart rotor but the concept also benefits other aspects of the cost of energy equation. Reducing the loads leads to less material requirements and hence reduced manufacturing costs for a given rotor size. However, less materials also means a reduction in strength and stiffness, and an increase in machine dynamics, which in turn requires higher performance control. The increased flexibility is of significance when considering the fact that changing loads change the airflow over the blade, thus the aerodynamic loading, compounding the complexity of the aeroelastic system. Ng et al., (2015b) investigates this issue using an aeroservoelastic state-space vortex lattice model. Reduced loads also enables an increase in the size of the rotor, which leads to an increase in energy capture. The smart rotor can also be operated to increase energy capture at below rated power by improving aerodynamic efficiency and increasing loads. The disadvantages to smart rotors include added weight and complexity, and increased maintenance and equipment costs. Overall it has yet to be seen whether the added value brought by smart rotors outweighs the added systems costs, but it is certain that

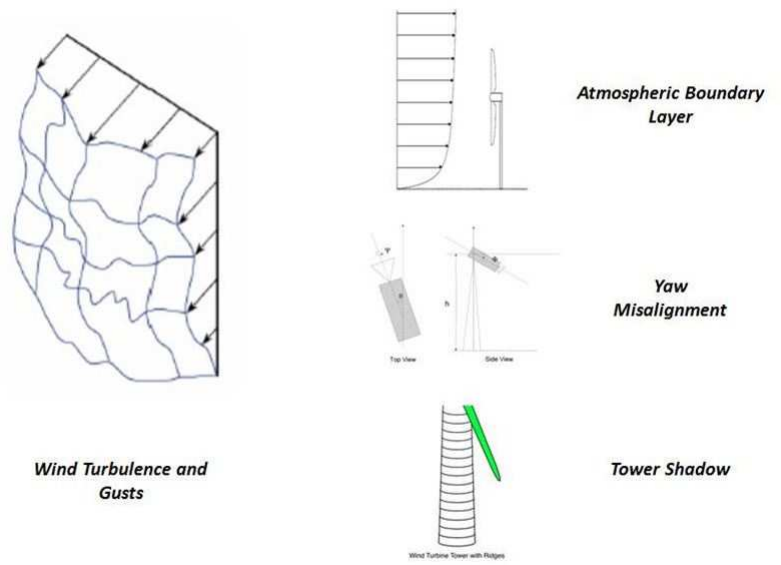

Figure 1.2: Stochastic and deterministic disturbances experience by a wind turbine (TuDelft, 2012)

improvements in smart rotor modelling and controller design are required if progress is to be made. Hal, (2002) gives a thorough analysis of the design of a wind turbine and the environment in which they operate. The critical aspect in terms of active load control is to understand the nature of the system dynamics and the load variations imposed. The loads experienced by the turbine are commonly caused by stochastic and deterministic disturbances. Stochastic components are random, the most of obvious of which is the variable nature of the wind itself. The wind varies in both frequency and magnitude and each change produces a variation in aerodynamic load, which then passes through the turbine system. Deterministic components are fluctuations associated with the periodic nature of a turbine and include factors such as the atmospheric boundary layer, stator-rotor interaction and yaw misalignment, as shown in Figure 1.2.

Both types of disturbances create loads that require managing. Deterministic disturbances tend to be easier to mitigate against as their period and magnitude can be relatively easily estimated from other turbine data (e.g. rotor speed, blade root strain sensors).

The effect of the wind loads onto the turbine can then be categorised into fatigue and extreme loads. As the name suggests, fatigue loads are linked to the repetitive stresses onto the system. The cumulative effect of these relatively smaller disturbances can cause part of the system to fail. Miners rule is used across many industries as a method to estimate the cumulative fatigue loading from a combination of different frequency and magnitude disturbances (Sutherland and Mandell, 2004). Extreme loads are associated with one-off, rare events that cause a significant peak in the blade loading. There are many extreme load sources, for example a freak gust or a sudden system failure. Smart

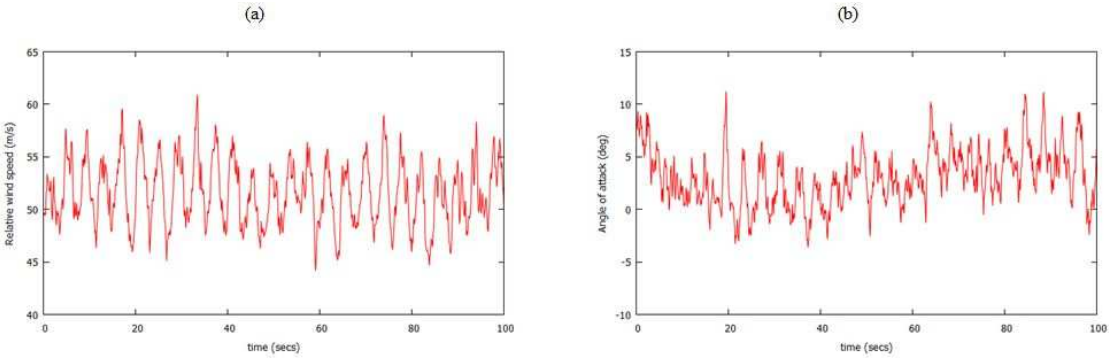

Figure 1.3: Real turbine data time series at 30m span (a) relative wind speed (b) angle of attack

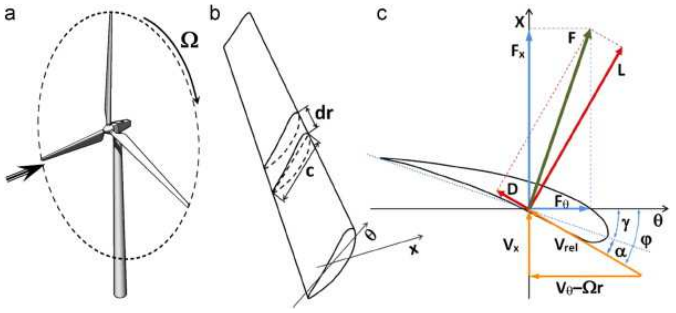

Figure 1.4: Wind turbine parameters associated with the blade element approach (Port-Agel et al., 2011)

rotors are aimed at mitigating against both types of loading. This report considers the local effect of a smart rotor device so it is useful to consider the typical loads onto a blade at a 2D section as shown in Figure 1.3.

The figures shows the variation in angle of attack (α) and relative wind speed (V_{rel}) onto the blade at a cross-section at approximately 30m span along a 45m blade. The relative wind speed comprises of the axial oncoming wind speed (V_x) and the tangential speed due to the rotation of the turbine (Ωr), as shown in Figure 1.4.

The lift on the 2D aerofoil section is proportional to the aerofoil lift coefficient (itself a function of angle of attack) and the square of the relative wind speed. The lift variation, which requires estimation from a choice of sensors, will show a similar fluctuation to the wind speed and AoA variations in the time domain. The rotation speed of the turbine ($\sim$ 15rpm) can be seen in the period of the dominant frequency ($\sim$ 4 seconds), along with higher frequency disturbances. Figure 1.5 shows the mapping of the blade position to the velocity at 30m along the blade.

It is assumed here that a constant lift at all 2D sections results in significant load reduction, therefore the aim of the smart rotor system is to attenuate these disturbances to a constant value. This research will demonstrate the use of Iterative Learning Control

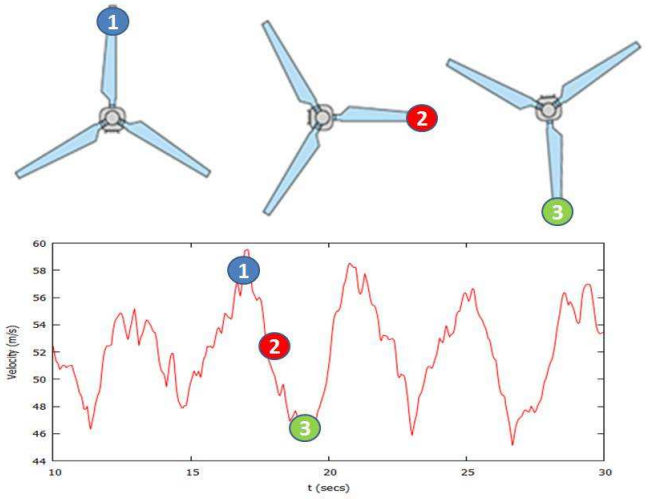

Figure 1.5: Velocity fluctuations at 30m span mapped to approximate blade position

applied to a simple CFD model of a 2D section of a smart rotor device to achieve this aim.

The concept of using smart devices for active load control has been in existence for a number of years, originally developed in the rotorcraft (Straub, 1996) and aerospace industries (Stanewsky, 2001). Johnson et al. (2008) and Barlas and van Kuik (2010) give an overview of the state of the art smart rotor control for wind turbines. The topic is highly interdisciplinary and as such the literature review will be divided into 5 areas; active flow control, actuators, sensors, control and aerodynamic modelling. The introduction also includes an overview of Iterative Learning Control and methods for estimating the lift experienced by a blade. Chapter 2 outlines the flow model used and its verification. Chapter 3 designs simple phase lead and P-type ILC for oscillatory and vortical flow using the direct lift from the model. Chapter 4 describes the pressure sensor arrays used to estimate the lift. Chapter 5 tests the designed ILC scheme for a range of flow conditions using both direct and estimated lift. Chapters 6 and 7 conclude the work and provide suggestions for future work.

1.2 Active Flow Control

There are four parameters in the lift equation that can be manipulated for the purposes of wind turbine load control:

1. Blade incidence angle (variable pitch and/or predetermined blade twist)
2. Flow velocity (variable rotor speed)
3. Blade size (variable blade length)

4. Blade section aerodynamics (active flow control)

Modern turbines take advantage of (1) and (2), while (3) and (4) are concepts that are currently in the prototyping stage. (1), (2) and (3) can be used to mitigate against low frequency fluctuations but higher frequency spanwise fluctuations require the application of (4). These spanwise velocity fluctuations increase in frequency and magnitude as blade diameter increases. (1) can be manipulated by using individual/collective pitch variation but suffers from slow actuation (therefore not quick enough to capture gust effects) and an inability to mitigate against spanwise flow variations. Passive blade/twist (Maheri and Isikveren, 2009) (i.e. blades twisting in a predetermined way when aero loads are applied) can react against spanwise variations but are associated with the disadvantage of reduced energy capture and increased manufacturing costs. (3) has been prototyped but adds significant complexity and cost to the system (Pasupulati, 2005). (4) is therefore being investigated as a means to control low and high frequency, spanwise load variations. Active flow control senses local changes in flow conditions and acts to counter any negative effects. If used incorrectly, active flow control can have a negative impact on performance. Smart structures are an integral part of active flow control and defined by Chopra (2002): "a smart structure involves distributed actuators and sensors and one or more microprocessors that analyse the responses from the sensors and use integrated control theory to command the actuators to apply localized strains/displacements to alter the system response".

The benefits of active flow control have been investigated in the rotorcraft industry for a number of years. Chopra (2002) gives a thorough overview of smart and integrated structures, with application focused towards rotorcraft. Dieterich et al. (2006) shows results from the installation of a full scale rotor with active trailing edge control. In the wind industry a number of studies have been carried out outlining the benefits of active flow control, the European project UPWIND (Barlas et al., 2006) being a good example.

The three main control objectives are to control the torque/power experienced by the drive train; increase fatigue life of components; and maximise energy production. These three needs have to be balanced and the strategy deployed is dependent on the operating region of the turbine, which in turn is dependent on the wind speed. At below rated power the pitch is fixed and the rotor speed varied to control the torque, with the aim of maintaining the optimum tip speed ratio. In contrast, at rated and above rated power, the rotor speed is constant and the blades pitched to keep the turbine within load/torque limits. Active flow control and smart rotors can be beneficial across the operating range; applied at below rated power to increase loads and at/above rated power to reduce load fluctuations, as shown in Figure 1.6.

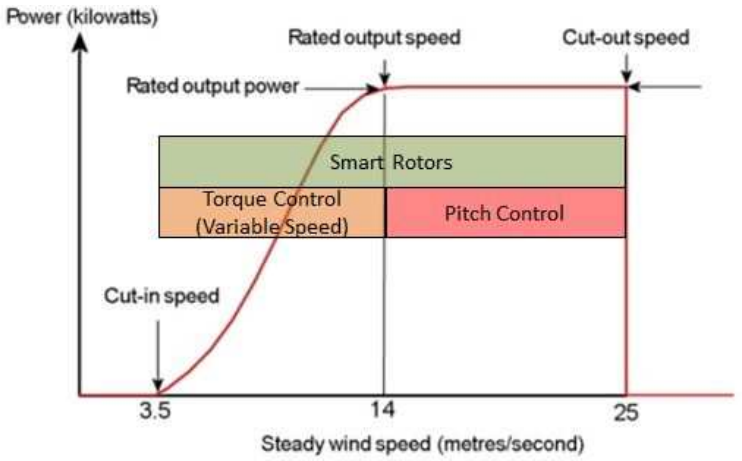

Figure 1.6: Typical turbine power curve showing control system operating ranges (WindPower, 2012)

Flutter is also an important consideration and further research is required into active flow control device performance in flutter conditions as limited studies have been carried out. Politakis et al. (2008) reviews how actuated trailing edge flaps can be used to suppress classical flutter.

In addition to the effects of geometric changes, active flow control can change the flow in three ways - delay/advance transition; suppress/enhance turbulence; and prevent/promote separation. Changing these flow phenomena results in an effect on drag, lift, mixing levels, heat transfer and flow induced noise. These effects tend to be interdependent; therefore design trade-offs in active flow control are often required. Wind turbine application of active flow control mainly concerns the manipulation of lift and noise. Active flow control devices can be split into passive and active (predetermined and interactive). Predetermined active devices are on all the time and independent of any system parameters, while interactive active devices can be either open loop (output not considered) or closed loop (feedback and action based on error between target and actual values). Closed loop active gives better performance and therefore is widely accepted to be the most suitable for smart rotors.

1.3 Actuator Devices

Johnson et al. (2008) gives a thorough overview of potential actuator devices for the smart rotor concept. The report focuses on the devices and the generated flow phenomena. Figure 1.7 summarises the relevant devices for wind turbine application. Delay stall (DS) devices are not suitable for load control because they are not very effective at decreasing lift. A method for using DS devices for load control involves redesigning the blade to operate at lower lift values. The DS devices are then used to increase the lift when required, to balance the loads. However, this involves the costly process

	Devices	Geometric (G) / Fluidic (F) / Plasma (P)	Leading Edge (LE) / Trailing Edge (TE) / Mid-Chord (MC)	Inc. Lift (I) / Dec. Lift (D) / Delay Stall (DS)	Steady (S) / Unsteady (U)
1	Traditional Trailing-Edge Flaps	G	TE	I / D	S / U
2	Nontraditional Trailing-Edge Flaps	G	TE	I / D	S / U
3	Microtabs	G	TE	I / D	S / U
4	Miniature Trailing-Edge Effectors	G	TE	I / D	S / U
5	Microflaps	G	TE	I / D	S / U
6	Active Stall Strips	G	LE	D	S
7	Vortex Generators	G	LE	DS	S
8	Blowing and Suction	F	LE / TE	DS	S / U
9	Circulation Control	F	TE	I / D	S
10	Plasma Actuators	P	LE	DS	S
11	Vortex Generator Jets	F	LE	DS	S / U
12	High-Frequency Micro Vortex Generators	G	LE	DS	U
13	Synthetic Jets	G / F	LE	DS	U
14	Active Flexible Wall	G	LE	DS	U
15	Shape Change Airfoil	G	MC	I	S / U

Figure 1.7: Possible active flow control devices: G = geometric device, F = fluidic device, P = plasma actuators, TE = trailing edge, LE = leading edge, MC = mid-chord, I = device increases lift, D = device decreases lift, DS = delay stall, S = Steady (Johnson et al., 2008) (note circulation control here refers to a aerofoil using the coanda effect on the trailing edge)

of fundamental blade redesign and reduced power output. DS devices can be used to increase the maximum lift coefficient and therefore reduce the chord length but their suitability for control is limited. Consequently, only devices (1) (2) (3) (4) (5) and (9) from Figure 1.7 are considered suitable.

Traditional trailing edge flaps appear to be the favoured device for most turbine manufacturers at present and have been extensively researched in the context of wind turbine load control, for example Frederick et al., (2010). While suitable for proof of concept, traditional trailing edge flaps may not be the final solution. It is possible that one of the other systems in Figure 1.7 will have to be developed further. The compact trailing edge flap seems to be too complex a solution and the adaptive trailing edge geometry has limited deflection range. Both these variations also share the problem of needing a high voltage supply. The active compliant wing appears to be a suitable option with flexsys Inc recently testing their product on a business jet (FlexSys et al., 2012). The active compliant wing offers large deflection rates and improved transient response. The gradual change in shape means a reduction in flap loads and therefore smaller/lighter actuation systems can be used. The ACW also offers improved aerodynamic performance across the operating envelope.

Microflaps also appear to be a promising technology (Eisele et al., 2011). Microtabs, miniature trailing edge effectors and microflaps are all very similar conceptually. Microflaps appear to be superior because they offer greater manipulation of the lift than microtabs and do not require a blunt trailing edge. Microflaps also offer the advantage of being reasonably easy to install and can potentially be retrofitted to existing wind turbines. The downside to microflaps is that limited research has been carried out, although a recent report by TU Berlin (Eisele et al., 2011) indicates promising results. Circulation control (using the coanda effect) is an interesting concept but substantial

air supply requirements and added complexity make it seem impractical. Moreover, no load reduction capability analysis has been carried out (only power improvements were analysed).

A common complaint is that devices lose effectiveness when the separation point moves forward of the device. This is more common on the suction surface as the angle of attack increases. Remedies to this problem include integrating devices at the LE and/or devices on the TE pressure surface. It is clear that the actuator device choice is vast and it is not clear which device turbine manufacturers will favour. However, it is clear that some form of deformable trailing edge geometry device is a distinct possibility. This research will therefore initially be based on the assumption that the actuation device will be of this form. The choice of actuator device is largely irrelevant in the early stages of the modelling process but as the project progresses towards consideration of installation onto actual turbines, the chosen actuation device will have characteristics (bandwidth, range of motion, speed, feedback forces etc.) that will impose limits on the ILC scheme and will need to be accounted for in the ILC algorithm.

1.4 Sensor Devices

Sensors are a critical part of the smart rotor system. Sensors relevant to wind turbines will be reviewed here. The sensors are responsible for determining the fluctuating loads on a blade section. These loads are fed into the controller and a command is then sent to the actuation device on a continuous basis. The total aerodynamic loads cannot be sensed directly, therefore other parameters are monitored and simulation models used to estimate the loading.

Accelerometers measure the acceleration of a set of transducers embedded into the blade, and can therefore be used to deduce the velocity and pressure at a given point. Accelerometers are generally used on wind turbines for maintenance monitoring (vibration analysis and drivetrain monitoring). Their application has not been extended into blade sensing. Strain sensors are a more likely solution for smart rotor sensing. They broadly split into electrical and optical sensors. Electrical strain sensors can work on the principle of resistance, capacitance, photoelectrics or semiconductor physics. The sensors are placed at particular locations to sense local strains. The most common place to find this kind of sensing is at the blade root. The strain measurements from the gauges can be used to calculate fluctuating aerodynamic loads. Strain gauges are mainly used in laboratory tests or on wind turbine prototypes, but not in serial production. With strategic positioning, electrical strain sensors have the required characteristics (bandwidth, time response etc.) for use in a smart rotor system. Other practical factors, such as temperature sensitivity, complex installation and maintenance, lack of robustness, and effects on structural integrity means they are not commonly used for mass blade sensing. There

are a wide range of optical strain sensors available but only fibre optic strain gauges have been proven cost effective for blade sensing. The most common device is the fibre Bragg grating sensor. They work on the principle of illuminating a fibre core with a spatially varying pattern of UV light. As the blade and fibre flex, the light is partially reflected by different variations at each location and from this the deformation and loads on the blade can be calculated.

Fibre optics are currently used for structural health monitoring of blades and it is expected application could be extended to aerodynamic load sensing. Fibre optics offer a number of practical advantages over the traditional electrical sensors: lightweight, wide bandwidth, simple installation and maintenance, high measurement sensitivity, and high levels of robustness. The main problem with fibre optic sensing is their sensitivity to temperature fluctuations, they struggle to distinguish between the effects of temperature and strain effects. However, this problem can be overcome by integrating a second temperature filter element to compensate for local temperature fluctuations.

When a material undergoes a small displacement, an acoustic wave is emitted. Acoustic sensors use transducers, located at strategic locations, to detect these waves. Acoustic sensing systems can be embedded into blade material but tend to be more suited to smaller blades. Larger blades means acoustic attenuation starts to become a problem and obtaining accurate load information may not be possible. Acoustic sensors tend to be more focused on applications such as test/fatigue monitoring and damage detection.

Pitot tubes and Light Detection And Ranging (LIDAR) technology are other devices that can be used to give information about inflow disturbances and used as an input to a smart rotor system. Pitot tubes are commonly used as instrumentation on aircraft and are used to measure the flow onto the blade. LIDAR is a remote sensor that emits a laser into the turbine upstream. From the light reflected back off air molecules and aerosols, estimates can be made about the wind conditions. Lidar technology has the capability to give accurate information about 3D wind velocities and insights into turbulence, which could be used to control smart rotor actuators (Wang et al., 2012). The technology is relatively new and benefits to smart rotors are yet to be quantified.

Pressure sensors located at positions along the blade can be an effective method of estimating the lift. An understanding of the frequency of the lift fluctuations is required, as this parameter will determine the number of pressure sensors required. Gaunna and Andersen (2009) describes a simple thin aerofoil theory based model with trailing edge flaps that uses two pressure measurements on the upper and lower surface of a 2D aerofoil as a control input. Andersen (2010) outlines similar experimental studies into using two pressure sensors near the leading edge to estimate the lift. The excitation frequencies in the experiment correspond to the once per rotation and 1st flapwise eigenfrequency of a large turbine. Harmonic trailing edge flap motions were used at low frequencies (1/5 Hz) and low incidence (+/- 2 deg). These two studies conclude that pressure measurements

on the leading edge can be used as a control input for simple, low frequency inflow conditions. Whilst most of the other sensing devices are reasonably unproven in the field of wind energy, there is evidence that pressure sensors can be used for smart rotor control. Pressure sensors are reasonably easy to simulate in the flow model proposed in this report and therefore initially chosen as the sensing device.

1.5 Control

Kim and Bewley (2007) gives an overview of linear systems and control theory to the fluid mechanics community. Two different definitions of flow control are proposed: "any mechanism that manipulates a fluid flow into a state with desired flow properties" and "the application of a systems and control theory to the Navier-Stokes equations". The paper focuses on linear model-based control theory and is focused primarily on the feedback problem of inherent time lag within the system. Feedforward controllers navigate around this problem but they require high fidelity models which can cope with all possible sensor inputs. The wide range of disturbance types for the smart rotor problem means pure feedforward control would be too complex.

Preliminary research studies into smart rotor control suggest that controller reliability has so far been overlooked and the design for optimal controllers is not yet completely solved (Rice and Verhaegen, 2010). Controller reliability (software and hardware), in terms of the ability to reduce loads for the entire turbine lifecycle, is a major barrier to the adoption of smart control on full scale turbines due to the current industry emphasis on reliability. Effective controllers have been designed but not with inbuilt design driver factors and questions remain over the reliability of the models to accurately simulate operation in all operating conditions (Buhl et al., 2005), (Hand et al., 2006). Rice and Verhaegen (2010) has done some basic work on addressing design drivers by introducing control cost functions to represent power consumption.

The control objectives of smart rotors tend to focus on load control (fatigue and extreme) using traditional proportional (P), integral (I) and differential (D) control. Andersen (2005) simulates PD controlled flaps in three dimensions. The study claims significant reduction in flapwise blade root moment (60% reduction without signal noise, and 40% with). However, PID controllers cannot be easily extended to multi-input-multi-output (MIMO) systems. Attempts to make them MIMO may lead to individual systems competing with each other and lead to poor performance. Feedback control reacts to the measured effects of inputs and disturbances, and therefore has a time lag. The time taken for the air to pass over the blade chord is very small (<1 sec at the tip), therefore the time lag associated with feedback control could have a detrimental effect on local smart rotor control performance. Research has also been carried out to assess the viability of using smart rotors to increase and regulate power. Joncas et al. (2005) indicates

a 2% increase in power production using flaps, whilst Lackner and van Kuik (2009) a reduction in power when flaps used at low speeds. Another research requirement lies in balancing multiple, and possibly conflicting control objectives using smart rotors.

Rice and Verhaegen (2010) generates a smart blade model in a form suitable for the analysis and design of a feedback controller that is robust to uncertainties and non-linearities. The paper stresses the difficulty in designing robust/computationally efficient controllers for distributed systems. The model is basic and more detail is required by implementing finer discretisation and knowledge of modern distributed control methods. The author aims to demonstrate how modern robust control techniques can be used on simple models. The results are qualitative conclusions that can be extended to more complicated and realistic models. The author does not aim to design a controller for a real turbine or prove certain control schemes are better than others.

Robust control methods for distributed networks are still in the early stages of development and have not yet been implemented on problems like smart rotors. Rice and Verhaegen (2010) shows how to incorporate uncertainties and bounded non-linearities into a model suitable for the design of robust control techniques (centralised and distributed). The feedback control system design is only for coarse grids and centralized computational techniques.

Rice and Verhaegen (2010) states that models at present do not take into consideration fundamental limitations of control, reliability and robustness. Wind turbine models do not fully capture 3D aeroelastic coupling, which means errors in the feedback control design methods. The impact of time lags on controlling higher modes is highlighted.

Assuming cheap, reliable actuators and sensors, two other main problems have been identified (Rice and Verhaegen, 2010). Firstly, handling the non-linear dynamics and aerodynamic coupling is an issue, due to the lack of established optimal controllers for non-linear systems. Controllers are usually not very robust for non-linear systems can and become unstable for small deviations from the original model. Wind turbines are predominantly non-linear and smart control actuators could add additional non-linearity. A need is identified to add robustness margins to accommodate actual turbine behaviour. Secondly, the scale of the wind turbine problem and the complexities and unexpected behaviour when scaling are an issue. Local models have been created but it has been suggested they are unlikely to work for large turbine blades. Also, distributed systems on a decentralized structure have been shown to be closed loop unstable (Rice and Verhaegen, 2010).

1.6 Aerodynamic Modelling

Wind turbines, by their very nature, interact with the wind in a non-linear manner and exhibit uncertain dynamics. This makes accurate modelling very difficult, which is particularly important in the advancement of the smart rotor concept. The wind industry is conservative and will not test full scale smart rotors until prototypes are verified against improved simulations.

In Marrant and van Holten (2006), a 3D time varying model of a smart rotor is benchmarked against a 6MW turbine using a time marching blade element model. It is assumed that the smart rotor reacts instantaneously to the loads and no direct control is used. Lackner (2009) generates an aeroelastic model with embedded deformable trailing edge geometries for a 5MW turbine. Unsteady aerodynamics are modelled and a control scheme implemented. Andersen et al. (2009) integrates a deformable trailing edge flap controller into a simulation model of a MW scale variable speed turbine. Ng et al., (2015a) investigates wind turbine load control using a combination of aeroelastic tailoring and trailing edge flaps.

Barlas and van Kuik (2010) highlights the main problems in modelling smart rotors as "defining the unsteady aerodynamic environment; calculating changing aerodynamic loads; calculating forces under non-attached flow; predicting device wakes; merging device and rotor aerodynamics, dynamic inflow and time delay on blade loading; and transferring aerospace knowledge, including macro wind field models." The author also identifies the importance of modelling the structural dynamics with the inclusion of smart devices. Lackner and van Kuik (2010) supports the claim of a gap in aeroelastic modelling, identifying the need to include unsteady aerodynamic and dynamic stall models. The author analyses the performance of a smart rotor controller, designed for alleviating fatigue load, during extreme loading events. The author concludes that the use of trailing edge flaps during above rated conditions reduces loads due to gusts.

Rice and Verhaegen (2010) designs transfer functions for a generic actuator and indicates the need to model specific actuator/sensors properly to achieve reliable controllers. The author also states that actuator bandwidth and aerodynamic settling time may be limiting factors, and proposes that the accuracy of modelling actuators is as important as the actuator design.

Methods used to calculate dynamic loads on deformable trailing edge geometries (DTEG) from a 2D perspective, can be split into the following categories (with increasing levels of complexity):

1. Unsteady classical aerofoil theory can be used to calculate the pressure distribution along a given aerofoil with a DTEG (rigid or flexible). Integrating across the DTEG section will then yield the loads. These models are only valid for the inviscid/attached

flow region (i.e. the effects of dynamic stall and separation are not captured). Vortex panel methods provide more accurate results for similar flow conditions.

2. Dynamic stall models capture viscous effects for aerofoils with DTEGs but only for global aerodynamic forces (i.e. Cl, Cm, Cd etc.). Accurate dynamic pressure distributions are not obtainable from these models.

3. Quasi-steady viscous models can capture pressure distributions for aerofoils with DTEGs at set points in a flap cycle. Corrections can be added for the unsteady effects. Only applicable for low frequency flap movements and low free stream velocities. XFOIL (1985) is a panel method that can be used in this way.

4. Navier-Stokes CFD can capture dynamic pressure distributions for blades with DTEGs at different spanwise locations and can capture 3D cross flow effects. Disadvantages include questionable accuracy in deep dynamic stall and associated computational cost.

1.6.1 2D Unsteady Classical Thin Aerofoil Theory

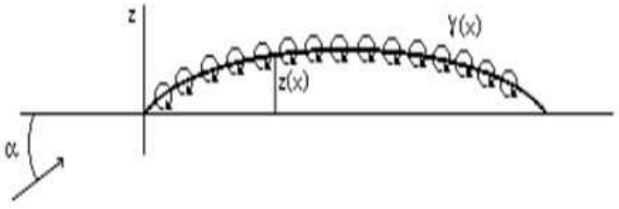

Figure 1.8: Classical thin aerofoil theory (AppliedAero, 2012)

The method models the aerofoil as a number of vortices located along the aerofoil camber line, Figure 1.8. Theodorsen (1935) was the first to calculate unsteady aerodynamic forces on an oscillating aerofoil with a aileron for potential flow. All theories in this section are modifications of Theodorsen (1935) and known as unsteady classical aerofoil theory. The 2D potential flow assumptions are valid for simulations where the Reynolds number is high, the Mach number low, the angles of attack small and the aerofoil relatively thin. These conditions can be found for a proportion of turbine operating states (Re$\sim$1,000,000, tip speed $<$0.3M). Peters (2008) gives a thorough overview of 2D incompressible unsteady aerofoil theory. The paper analyses different approaches for calculating aerofoil and flow field responses due to step responses, aerofoil oscillations and general motion. Most are based around unsteady classical aerofoil theory (i.e. not valid at high angles of attack and dynamic stall). The limitations of potential flow are clearly highlighted. Significant simplifications are present but the models are useful to gain important information about aeroelastic behaviour and unsteady aerodynamic phenomena.

The 70s/80s brought the introduction of rotary wing aerodynamics with returning wakes. In the 90s, Peters rewrote the 2D theory (Peters, 2008) so the states represented inflow disturbances, i.e. a feedback system in which the inflow due to the shed wake is an open loop transfer function. Peters theory can be thought of in terms of two closed loop problems. Firstly, the backwards loop: given the bound circulation, what is the induced flow due to the wake. Secondly, the forward loop: given the disturbance of the angle of attack, what will be the lift (i.e. the bound circulation). The closed loop expressions can be expressed as transfer functions (Laplace and Fourier domain) and step responses (time domain). The potential flow equations used stem from the conservation of mass and momentum principles.

Codes and papers on application of unsteady thin aerofoil theory are readily available. Mateescu and Abdo (2003) and Sanders et al. (2003) claim pressure distributions (and therefore loads) for a flexible aerofoil in unsteady conditions. Johnston (2003) calculates energy requirements of a morphing wing, which implies chordwise loads are calculated. Gaunaa (2006) proposes a modification of Theodorsen (1935) in the context of wind turbine smart rotors. Gaunaa (2006) has adapted Theodorsen (1935) for a flexible aerofoil rather than a rigid flap. Peters (2007) is similar in principle to Gaunaa (2006) in that it advances classical thin aerofoil theory to include the effects of flexible aerofoils. The work is based on the potential flow equations and therefore not applicable in dynamic stall. Advantages over Gaunaa (2006) include the inclusion of 3D wake effects and reverse flow. The paper places itself between steady blade element theory and more advanced CFD approaches. Peters (2007) states that the classic theory proposed can easily be coupled with dynamic models. The wake / dynamic stall model requires the global lift as an input from the unsteady aerofoil theory and returns a modified value that includes dynamic stall effects. The dynamic stall models are not implemented in this paper. Another advantage of Peters (2007) is its hierarchical format, which requires only a limited number of terms to capture the essential physics. Vortex panel methods are a more detailed and accurate modelling method and are discussed in Chapter 2.

1.6.2 Dynamic Stall Models

Larsen (2007) proposes a simplified dynamic stall model for wind turbine aerofoils and draws comparisons to other common models. It is a good reference in understanding the mechanisms involved with dynamic stall modelling. Beddoes-Leishman, Oye, Riso, ONERA and Boeing-Vertol models are all explained and analysed. Larsen (2007) outlines the physical phenomena associated with dynamic stall and splits the available models into three categories: effects of phenomena modelled (reduced lift curve) (Oye, BL, Riso); hybrid lift curves (attached and separated flow) (ONERA model); and modifications to α (Boeing-Vertol model). Larsen (2007) states the goal of these semi-empirical models are not to capture every variation in the load, but to model the main characteristics in

a fast way. A complete physical model of dynamic stall based on first principles has not been developed.

Hansen et al. (2004) presents a dynamic stall model as discussed in Larsen (2007). It predicts global unsteady forces and moments on the 2D section undergoing arbitrary motion (heave, lead-lag, and pitch). Effects of shed vortices from the TE and a moving TE separation point are captured. The non-linear governing equations are linearized about a steady state for application in stability analysis (with the linearized model giving the same results for small oscillations). The model is validated against inviscid solutions and known aerofoil data.

Andersen and Gaunaa (2007) then develops the method in Hansen et al. (2004) to include the effects of a DTE.G. The model covers an aerofoil in arbitrary motion (heave, lead-lag, pitch) and TE flapping. The model gives the global unsteady aerodynamic forces. The models validity is limited to flap deflection of +/- 5 degrees. Andersen and Gaunaa (2007) expresses that only two state variables in the BL model are used to describe the dynamic behaviour of the separation point and that the separation point is related to the pressure distribution over the aerofoil. However, no model is proposed to correlate these two variables and the association is purely descriptive.

1.6.3 Unsteady Panel Method

The models discussed thus far do not offer the capability to calculate dynamic loads on DTEGs across all flow conditions, although local dynamic loads for attached flow and/or global dynamic loads for dynamic stall can be calculated. One option to approximate the local dynamic loads in the separated region is to create a quasi-steady panel method capable of outputting pressure distributions at snapshots in the flap cycle. XFOIL (1985) is a publicly available panel code that can give steady pressure distributions in attached and separated regions for aerofoils with DTEGs. However, this method would be limited to low flap frequencies. Lafountain (2010) utilises a similar method. Garca et al. (2011) is a Quasi 3D code that incorporates both viscous and inviscid effects.

1.6.4 Navier-Stokes CFD

Figure 1.9: CFD visualisation of flow past a 2D section with a deformable trailing edge Garca et al. (2011)

Navier-Stokes CFD is the most accurate method of calculating dynamic loads on DTEGs. Calculating dynamic loads on DTEG aerofoils can be performed using NS-CFD with varying degrees of complexity, and with it computational cost. The simplest being 2D dynamic analysis and progressing in complexity towards full turbine modelling with aeroelastic coupling. 2D dynamic analysis comprises of a DTEG aerofoil operating across the full range of flow conditions (i.e. attached to deep stall and various inflow models). Dynamic forces can then be calculated by integrating the pressure distribution across the DTEG section. Correction factors for 3D effects and aeroelastic effects can be incorporated. The inputs required for such an analysis are readily available from the standard blade element method.

Srensen (2010) gives a useful overview of CFD applications in wind energy. It explains the 2D and 3D EllipSys code (RANS, LES or DES) and its ability to capture dynamic stall in a moving frame. Srensen (2010), Page 12, shows an animation of dynamic 2D stall pressure distribution and Srensen (2010), Page 13, a visualisation of the 2D dynamic DTEG prediction of shaft torque for the NREL phase VI are compared with experimental data. The usual cases are considered (yaw flow, shear effects, deep stall, nacelle flow, stand still loads). Uncertainty remains about the onset of stall and the behaviour in this flow region.

In terms of global wind turbine CFD modelling, Rotor Embedded Actuator Control Technology (REACT) (TSB, 2008) is a helicopter rotor project that could serve as a useful reference for the wind industry. REACT will likely have developed some efficient CFD codes for calculating dynamic loads on DTEGs for all flow conditions. Spentzos et al. (2005) is a generic paper on modelling 3D dynamic stall using CFD. Barakos (2010) argues that CFD will become more relevant to wind turbine design as Mach numbers go above 0.3 and enter flow regimes where blade element theory is not valid. However, it is likely that with increasing rotor size, the rotor speed will be reduced to maintain optimum tip speed ratio. Another clear disadvantage of the blade element method is the internal dynamic stall models inability to give dynamic loads in separated flow condition. This leads to an argument of whether it is worth replacing the blade element model with an efficient NS-CFD tool coupled with a structural dynamics model. Results from TSB (2008) may indicate if this is realistic in the near future.

Iradi and Barakos (2010) compares local flow angles calculated from CFD with an instrumented NREL turbine. The URANS equations are solved using a multi-block structured grid with a sliding mesh algorithm. The local flow angles calculated can then be used in the BEM model if required. Iradi and Barakos (2010) also compares the surface pressure distribution of the NREL turbine with the CFD model. Iradi and Barakos (2008) indicates it is possible to obtain chordwise pressure distributions for different spanwise locations.

Cesnik (2009) compares NS-CFD calculations with low order models for a rotating blade with a section of DTEG aerofoil. The pressure coefficient on each cell face that lies on the blade surface is computed within the CFD code. This theory would need to be modified to include the effects of a dynamic DTEG Barakos (2005b) compares pressure distributions for a helicopter blade with a trailing edge flap but again, dynamic effects are not included. Barakos (2009) shows a full wind turbine CFD model with good results for attached and semi stalled flow. Barakos (2006) offers a more efficient way to model 3D dynamic stall using neural networks. The neural network method is claimed to be less computer intensive than the ONERA dynamic stall model. Barakos research profile indicates a move towards a unified CFD code to predict dynamic pressure distributions on rotating blades with DTEG aerofoil sections. M Potsdam (2010), Chopra (2010), R Steijl and Barakos (2010) and R Steijl and Barakos (2009) are other relevant works in this area.

Wall (1999) gives some info about validating CFD against experimental data for unsteady flow over a helicopter rotor with aerodynamic flaps and Behrens et al. (2011) obtains unsteady pressure distributions for DTEG aerofoils using an incompressible immersed boundary method.

1.7 Iterative Learning Control

There are three major problems inherent with the smart rotor controllers discussed; lack of robustness and reliability; time delays associated with the feedback loop; and dependency on complex aero models. A controller is sought that is effective with a simple model, stable in all conditions and not affected by time delays. Iterative learning control can provide such a solution. The initial solution will operate at a local, 2D level with the view to integrating such schemes into full turbine control.

Repetitive learning control (RLC) could be an effective solution as fluctuating loads on a turbine are to a large extent periodic. This type of control rejects unknown periodic disturbances which cause fluctuations in a given parameter. However, RLC is effectively a feedback controller and therefore carries the problem of the inherent time lag. RLC also requires knowledge of the disturbance period, and is therefore not suitable for gust alleviation. Closely linked to RLC is Iterative Learning Control (ILC). ILC acts in a similar manner to a feedforward controller, therefore the time lag problem is not present and ILC can potentially eliminate the need for a high fidelity model (Cai, 2009). ILC is seen as a controller that can have an adaptable control strategy during operation and handle a sufficiently wide range of disturbance types.

ILC uses information from previous execution(s) to modify the control input to be used on the next execution and iteratively improve the controller performance. Modifying the control input is different to most other forms of adaptive control where the parameters in

a pre-set model are modified. The ILC algorithm produces a control law that generates a signal to the actuators that will force the error (difference between actual and target output) to zero after an infinite number of iterations. ILC uses a fixed model and adjusts its response by filtering the input signal (e.g. pressure sensor data), and is capable of handling large model uncertainties. Thus, a relatively simple model structure could be used, giving the required fast response, with the ability to cope successfully with a variable and not particularly well defined input signal, while continually refining its action to achieve the desired objective. ILC is therefore well matched to the smart rotor problem.

A recent survey of the ILC field can be found in Bristow et al. (2006). Note that this survey concentrates on control of a process with a signal which repeats on a regular basis, such as a robot that is required to perform the same operation over and over again (the original framework for ILC). This would be applicable to some scenarios encountered by a turbine blade (e.g. oscillatory velocity fluctuations associated with yawed flow), but obviously not others (e.g. wind gusts). However, recent developments in ILC have led to schemes which can cope with non-deterministic signals (Bristow et al., 2006). Figure 1.10 shows the principles behind a 2D 1st order ILC system (Bristow et al., 2006).

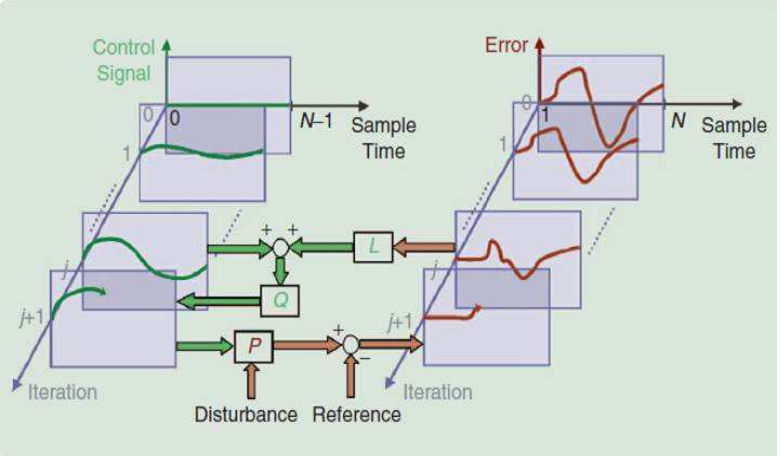

Figure 1.10: ILC principles (Bristow et al., 2006)

ILC can be applied in terms of P-type, D-type and anticipatory approaches. The D-type ILC is given as:

$$u_{j+1}[k] = u_j[k] + \frac{g(E_j[k] - E_j[k-1])}{dt} \tag{1.1}$$

Where u is the control input; j the iteration number; k the time step number within an iteration; g the gain; E the error (between the target and actual value); and dt the time step. All values are taken at time t, therefore the relationship is algebraic. If there is a lack of uncertainty and minimum noise in the system, this form of ILC can be used to

converge the tracking error to zero. However, high order signal derivatives are usually required which means a D-type ILC algorithm can be difficult to implement. Higher order derivatives tend to be difficult to measure (robots are usually equipped with joint position sensors) and signals become noisy when differentiated. The bound size on the tracking error is proportional to the amount of noise.

P-type ILC controller is given, with a forgetting factor, as:

$$u_{j+1}[k] = u_j[k] + gE_j[k] \tag{1.2}$$

In this case, the learning law does not take into consideration the direction of error trends. This means that if the error is zero, the controller stops learning. The forgetting factor is used to give the controller robustness against uncertainties. In general, the smaller the forgetting factor, the larger the tracking bound errors. However, the forgetting factor should be small enough to forget the arbitrary initial guess, therefore a compromise has to be made.

P and D-type ILC controllers both have shortcomings, therefore an anticipatory ILC algorithm is introduced:

$$u_{j+1}[k] = u_j[k] + gE_j[k + \Delta] \tag{1.3}$$

Where Δ is a small time step. A causal linked pair in the jth iteration is used to give the action in the $j + 1$ iteration. Trends and directional information are captured and higher order terms avoided. It is critical that noise levels are kept to a minimum in the measurement to ensure easy implementation.

Freeman et al. (2007) offers a framework in which ILC structures have been evaluated experimentally for a non-minimum phase plant. Torsionally flexible turbine blades can become non-minimum phase systems. Phase lead update laws and forgetting factors are used to overcome problems of instability and convergence of final errors. The algorithm initially requires a model but is then reformulated to not need a model. Methods for capturing higher frequencies and practical limitations are considered and the algorithm performance analysed. Chi et al. (2008) offers an adaptive iterative learning control (AILC) scheme that introduces a parametric adaption law in the learning process (recursive least squares algorithm). This method could be useful for stochastic disturbances. Saab (2001) and Saab (2003) introduce ILC algorithms into a stochastic environment, while Cai (2009) tests stochastic ILC algorithms experimentally.

1.8 Thesis Goals

This work aims to add to the understanding of how smart rotor systems can reduce fatigue and extreme load fluctuations on wind turbine blades across typical operating conditions with particular focus on the application of iterative learning control. Specific goals are listed below:

1. Aerodynamic model. Most other research into wind turbine smart rotors thus far have used simple thin aerofoil theory or indicial methods. This work aims to develop a 2D computationally efficient aerodynamic model that accounts for the aerofoil shape and circulation control using the vortex panel method.

2. Iterative learning control. Previously ILC has been mostly used in the world of robotics. The research in this thesis aims to extend the application of ILC into deterministic and stochastic flow control.

3. Smart Rotors. Develop a method of lift estimation that is an adequate input to the ILC algorithm with the intent of reducing fatigue and extreme loads. Additionally an understanding of how actuator response rates effect attenuation will be achieved.

Chapter 2

Flow Model

2.1 Validity

The lift of an aerofoil/wing section comes primarily from the pressure exerted by the fluid on the surface of the airfoil. In normal turbine operating conditions, the angle of attack is not high enough to provoke separation so the flow remains attached, and the pressure distribution on the surface of the blade can be calculated by assuming the flow is inviscid. This greatly simplifies the calculation, and is the approach used here. However, this does exclude extreme cases such as rapid changes of direction or shear when separation is provoked. In such extreme situations, any simple model of the flow of the type considered here may produce inaccurate results. However, full Navier-Stokes simulations, which will give a complete picture of the flow, are too expensive computationally to allow detailed investigation of the control methods. Thus, a relatively simple but usually accurate flow model is employed to investigate feasible control schemes which could eventually be applied to full scale simulations or experiments. A discrete vortex method for the two-dimensional incompressible Navier-Stokes equations is used, as previously developed by Clarke and Tutty (1994).

2.2 Dimensions

Flow past a wind turbine blade has two characteristic time scales, that of the period of rotation (around 4s for a modern turbine blade) and that for the typical time for the flow to pass the blade section. While the former remains relatively constant, the latter varies along the blade, due to both the change in the chord length and velocity over the blade section. The chord decreases along the blade, from 4m near the hub to around 1m near the tip for a turbine which with a blade length of 55 m (Vestas V112-3.0MW), while the velocity increases along the blade. This results in a significant

variation in the characteristic time for the flow to pass the blade. Here we are interested in situations in which, using the blade as a reference, disturbances are convected past the blade. Hence the problem is cast in non-dimensional form using the mean free stream velocity V_∞ on a blade section and the chord length of the airfoil H as reference values, as is standard aerodynamic practice. $\mathbf{v}^* = V_\infty \mathbf{v} = V_\infty(\nu_x, \nu_y)$ are the velocity components in $\mathbf{x}^* = H\mathbf{x} = H(x, y)$, where the asterisk denotes a dimensional quantity. Time is nondimensionalized using H/V_∞ so that $t^* = \frac{H}{V_\infty}t$. The variation of time scales along the blade is now represented by a change in the non-dimensional period of the rotation, increasing with radius. Non-dimensional quantities will be used in Chapters 3 and 4, and Sections 5.1 and 5.2 where simulated turbine data is used. In Section 5.3, where real turbine data is used, dimensional values will be applied throughout. When real turbine flow conditions are used, a specific spanwise position is chosen (i.e. H is fixed and V_∞ is known from the simulink model output) and there is no requirement to non-dimensionalise the data.

2.3 Vortex Panel Method

A vortex panel method is used to model the incompressible potential flow over a thick 2D aerofoil. The vortex panel method is used extensively throughout aerospace and forms the basis of standard aerofoil modelling tools such as XFOIL (1985). The method divides the 2D aerofoil curvature into a number of straight lines and assigns vortex and source panels to these segments. In the model used throughout this report, vortex panels are placed at a small distance just above the aerofoil surface and source panels just below, as shown in figure 2.1:

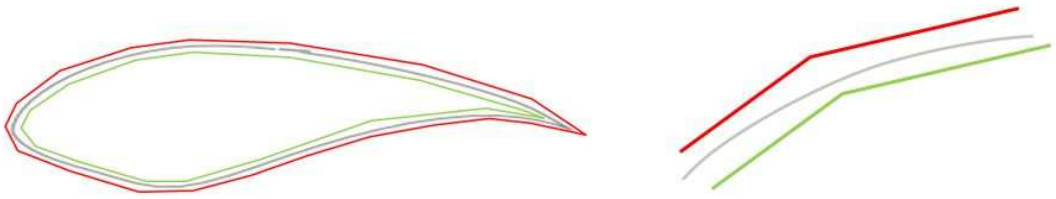

Figure 2.1: Aerofoil curvature (grey) modelled by vortex (red) and source (green) panels

The panel method is used to satisfy the boundary conditions on the surface of the body and together the panels simulate the boundary layer around the aerofoil, by creating circulation and hence lift. A set of 2N discrete panels are used to enforce the boundary conditions at the surface of the body. There are N vortex panels with constant vorticity on each panel λ_i, but with the strength varying between the panels. The vortex panels operate by setting the tangential velocity at the surface to zero, from which it follows

that, in principle, the kinematic boundary condition of zero normal velocity is satisfied, but only within numerical error (see Clarke and Tutty (1994) for details). Here the vortex panels are augmented by a similar set of N source panels, of strength κ_i, placed just below the surface, so that zero normal velocity at the surface is explicitly enforced. For a body with a smooth shape, usually only vortex panels are used as the source panels contribute little (κ_i will be small and tend to zero as N increases), but increase the computational effort. However, in this work there is a sharp trailing edge, and a jump in circulation at the trailing edge which is used as actuation. Both of these can give rise to relatively large numerical errors with vortex panels only. Hence source panels are also used to improve the accuracy and the numerical conditioning of the procedure. Details of the vortex and source panels and the velocity fields they generate can be found in many standard texts (Andersen, 1985).

Combined the source and vortex panels produce a set of 2N linear equations in 2N unknowns, i.e. λ_i and κ_i. However, this problem is not well posed and the matrix will be singular (within numerical error). This reflects the fact that there is an infinite set of solutions to the problem of inviscid flow past a body with zero flow across the surface of the body, with the solution varying with the (arbitrary) lift on the body. Usually, the physically relevant solution is that with the flow leaving the trailing edge smoothly, aligned with the trailing edge, known as the Kutta condition (see Andersen (1985) for details). Although the wall normal velocity is zero, there is a nonzero tangential (slip) velocity just above the surface. Numerically, the Kutta condition implies that $\nu_a = \nu_b$, where ν_a and ν_b are the tangential velocities in the direction of the trailing edge at midpoints of the panels adjacent to the trailing edge, as shown in Figure 2.2.

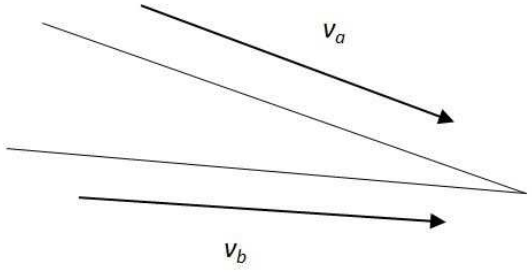

Figure 2.2: Flow at the trailing edge

The system of equations is now overdetermined, with 2N + 1 equations in 2N unknowns. A well-behaved approximate solution is obtained using a least-squares approach, as in Clarke and Tutty (1994). The trailing edge condition is satisfied explicitly with this procedure and the aerofoil pressure distribution can be calculated to obtain the lift.

2.4 Control Simulation

Trailing edge devices used for lift control act by modifying the flow near the trailing edge, generating vorticity, and thereby altering the circulation on the body and hence the lift. For example, a trailing edge flap redirects the flow. This can be modelled in a simple manner in the current framework by allowing a jump in the tangential velocity at the trailing edge rather than applying the Kutta condition, which will directly change the way the flow leaves the aerofoil at the trailing edge. That is, by using $u = \nu_b - \nu_a$ as the control input and the lift as the output of the system. The control scheme is shown in Figure 2.3.

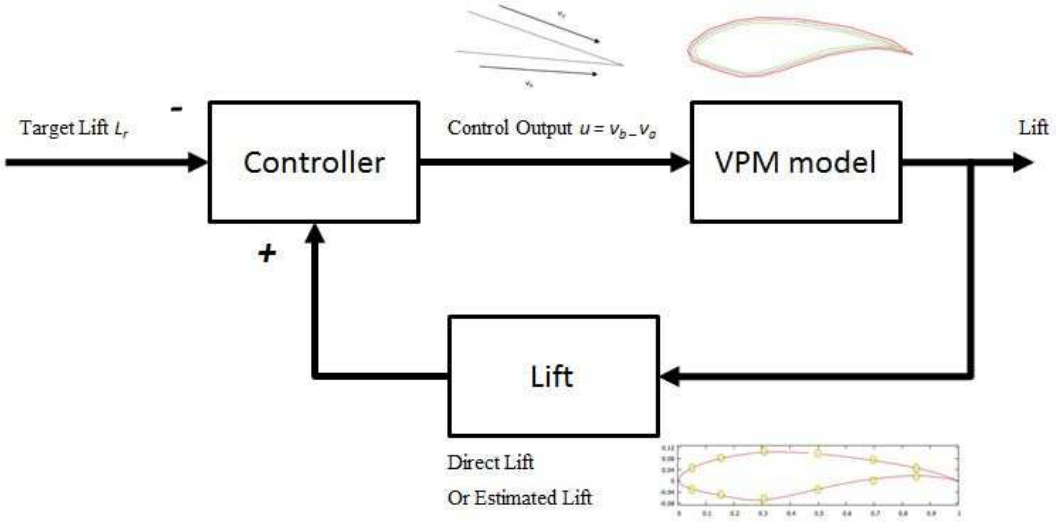

Figure 2.3: Simple control scheme

A non-zero value of u directly forces a change in the flow at the trailing edge, and hence a change in circulation and lift. This provides a relatively simple (compared to a full Navier-Stokes simulation) but realistic model of the flow and actuation which can be used to investigate control schemes using trailing edge devices for load control. The target lift L_r is defined as the lift value that the controller drives the aerofoil lift towards, with the aim of keeping the error (actual lift - target lift) to a minimum. The target lift is obtained by running the model at the required angle of attack in undisturbed flow conditions. This method of modelling the trailing edge device also has the advantage of not having to specify a particular flow control device.

2.5 Vortices (Stochastic Flow)

The base flow consists of the free-stream velocity $\mathbf{V}_0(t) = (V_o x(t), 0)$ and the velocity field generated by the vortex and source panels $\mathbf{v}_p(\mathbf{x}, t) = (\nu_p x, \nu_p y)$, the latter including

the effects of the actuation. In addition, disturbances are introduced into the flow in the form of discrete vortices. The Euler equations governing two-dimensional inviscid incompressible flow can be written in vorticity form as

$$\frac{D\omega}{Dt} = \frac{\partial\omega}{\partial t} + \nu_x \frac{\partial\omega}{\partial x} + \nu_y \frac{\partial\omega}{\partial y} = 0 \tag{2.1}$$

where

$$\omega \;=\; \frac{\partial v_y}{\partial x} - \frac{\partial v_x}{\partial v_y} \tag{2.2}$$

is the (single component of) vorticity, and $D/Dt = \partial/\partial t + v_x\partial/\partial x + v_y\partial/\partial y$ is the material derivative, i.e. the rate of change with time of a material quantity convected with the flow.

Equation 2.1 is a statement of the fact that in two-dimensional inviscid flow, vorticity is convected with the flow at the local fluid velocity. Hence the motion of an individual discrete vortex can be tracked by solving

$$\frac{d\mathbf{x}_\nu}{dt} = \mathbf{v}(\mathbf{x}_\nu, t) \tag{2.3}$$

where x_ν is the position of the (core of the) vortex. The complete velocity field v is now given by the sum of three components

$$\mathbf{v}(\mathbf{x}, t) = \mathbf{V}_0 + \mathbf{v}_p + \mathbf{v}_\nu \tag{2.4}$$

which are the velocities generated by the freestream, vortex/source panels and vortices respectively, with

$$v_\nu = \sum_{M}^{j=1} \mathbf{v}_\nu j \tag{2.5}$$

where there are M discrete vortices. $\mathbf{v}_\nu j$ is the velocity field generated by an individual vortex, given by

$$\mathbf{v}_{vj} \;=\; \Gamma_j \frac{(-(y - y_{vj}), x - x_{vj})}{|\,\mathbf{x} - \mathbf{x}_{vj}\,|^2} F(|\,\mathbf{x} - \mathbf{x}_{vj}\,|) \tag{2.6}$$

where Γ_j is the strength of vortex j, $F(s) = \int_0^s \gamma(s)ds$, and $\gamma(s)$ is the vorticity distribution of the core of the vortex. Setting $F = \frac{1}{2\pi}$ gives the classic point vortex representation. However, this is singular at its center $\mathbf{x} = \mathbf{x}_{vj}$, and for more than a small number of vortices (three) produces an unstable system. Hence, an axi-symmetric

distribution of vorticity with zero velocity at the center, reflecting the fact that a vortex generates a rotational motion, is used in practice. Here the standard model with a Gaussian distribution is employed, with

$$\gamma(s) = \frac{1}{\pi\sigma^2} e^{-s^2/\sigma^2}, \qquad F(s) = \frac{1}{2\pi}\left[1 - e^{-s^2/\sigma^2}\right]$$

Also $2\pi \int_0^\infty \gamma(s)ds = 1$ and therefore Γ_j is the circulation of the vortex.

The interaction between the discrete vortices and with the body produces a system of equations for which no closed form solution exists. A numerical solution can be produced by applying any standard time-stepping method to (2.3) for each of the M discrete vortices, using the velocity at the center of the vortex from (2.4). Here, as in Clarke and Tutty (1994), a second order Runge-Kutta method is used to move the vortices,

$$\hat{\mathbf{x}}_{vj} = \mathbf{x}^k_{vj} + \frac{1}{2}\Delta t\, \mathbf{v}(\mathbf{x}^k_{vj}, t_k) \tag{2.7}$$

$$\mathbf{x}^{k+1}_{vj} = \mathbf{x}^k_{vj} + \Delta t\, \mathbf{v}(\hat{\mathbf{x}}_{vj}, t_{k+1/2}) \tag{2.8}$$

where $t_k = k\Delta t$.

2.6 Calculating the System Output (Lift)

The jump in the tangential velocity at the trailing edge u is used as the control input to the system, with the aim of damping the variation in the lift due to the unsteady nature of the free stream velocity $V_0 x(t)$ and the influence of the vortices on the airfoil as they are convected past the body. The lift, which will be used as the output to the system, is most conveniently calculated from

$$L(t) = -\frac{1}{2}\sum_{i=1}^{N} \lambda_i \Delta_i v_x(\mathbf{x}_{ci}, t) \tag{2.9}$$

where Δ_i is the length of panel i and $v_x(\mathbf{x}_{ci}, t)$ is the streamwise component of velocity at $\mathbf{x} = \mathbf{x}_{ci}$, which is in the flow just above the midpoint of the panel.

2.7 Model Verification

The basic panel code was tested against publically available 2D aerofoil analysis software. In particular, the lift coefficients and pressure distributions for inviscid flow past the aerofoil obtained from the method presented above were compared with those found using XFOIL (1985), a well validated code commonly used for aerofoil calculations.

Pressure distributions for the NREL S825 aerofoil profile at different angles of attack are shown in Figure 2.4.

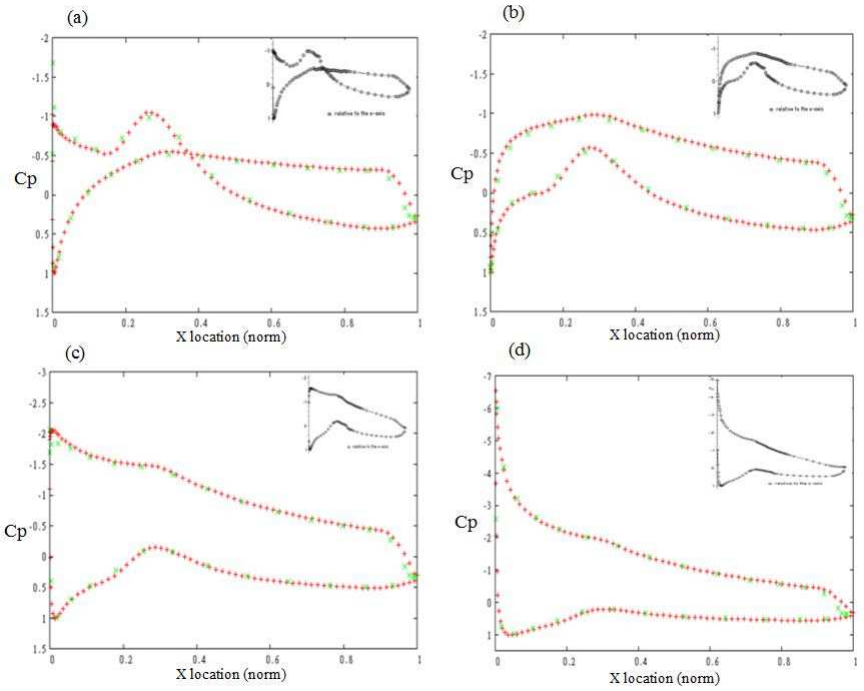

Figure 2.4: VPM model (green) verified against Xfoil (red) and experimental (black) for non-dimensional freestream velocity $U = 1$: (a) -5 degrees (b) 0 degrees (c) 5 degrees (d) 10 degrees

On the basis of the comparison, initially 404 source and 404 vortex panels were used. As usual, the panels were clustered towards the trailing and leading edges where the curvature is largest. As the analysis moved forward it became clear that the control performance did not deteriorate when fewer panels were used and as a result the number of panels were reduced to 130 (total), with the aim of improving computational efficiency. The next stage is to understand the relationship between the control input u and the global lift under a steady sinusoidal disturbance. As expected, increasing u results in a reduction in the mean lift in a linear manor as shown in Figure 2.5.

2.8 Aerofoil Profile

The aerofoil chosen for initial analysis is the NREL S825, as shown in Figure 2.6. The aerofoil is typically used on the outboard section of a 15m blade, which makes it a good choice because this is the location where the majority of the lift is generated, hence the location where flow control devices are most effective. Additionally, a large amount of experimental data is available for the S825 aerofoil (S825, 2001). The aerofoil shape is read from a text file in the VPM code, therefore changing the aerofoil at a later date is not a problem.

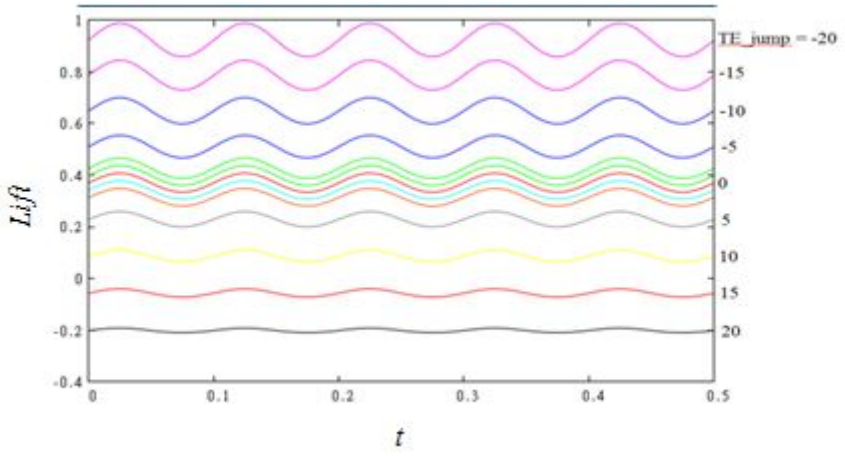

n

Figure 2.5: Lift changes due to variation in the control input $u = \nu_b - \nu_a$ for a sinwave freestream velocity disturbance

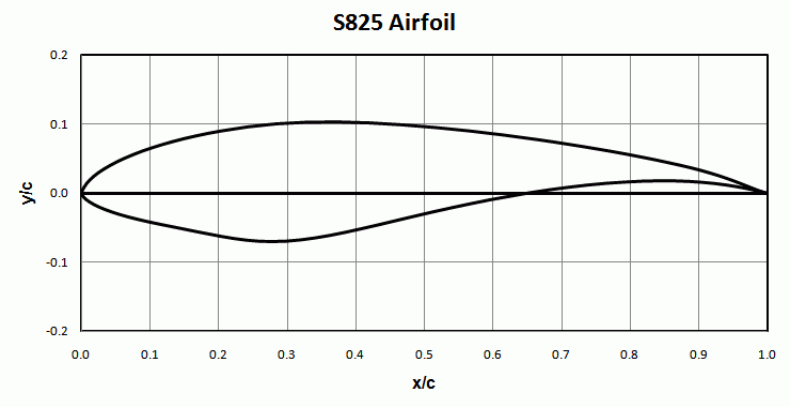

Figure 2.6: NREL S825 airfoil

2.9 Performance Measurements

Two measures have been used to estimate the degree of attenuation, a 2-norm and infinity norm:

$$L_2 = \left[\frac{1}{T_1 - T_0} \int_{T_0}^{T_1} (L(t) - L_r)^2 dt \right]^{\frac{1}{2}}$$

$$L_\infty = \max_k |L^k - L_r|$$

In general terms, L_2 can be thought of as measuring the fatigue load, and L_∞ the peak load on the blade. If the mean value of the lift is the target value L_r, then L_2 gives

the standard deviation of the lift. The results here aim to keep the mean value of the lift close to the target value, so that the standard deviation of the lift is close to the L_2 value. Also, the range of values for the lift lies within L_r plus or minus the value of L_∞. The integration for L_2 was performed over the time the vortices pass the aerofoil, beginning at a time after a number of freestream oscillations have passed to allow time for the controller to settle.

2.10 Wake Model

As discussed above, the introduction of a wake model adds a realistic non-linearity that simulates the Wagner effect. The vortex panels produce a set of N linear equations in N unknowns (the κ_i). However, this problem is not well posed and the matrix will be singular (within numerical error). This reflects the fact that there is an infinite set of solutions to the problem of inviscid flow past a body with zero flow across the surface across the body, with the solution varying with the (arbitrary) lift on the body. Here Kelvins circulation theorem is used to provide an extra condition, whereas previously the Kutta condition was used to close the solution. This states that the total circulation in the flow is constant. Note here that the circulation is minus the integral of the vorticity over the field, and the circulation for a vortex panel is $-\kappa_i L_i$ where L_i is the length of panel i. The system of equations is now overdetermined, with $N+1$ equations in N unknowns. A well-behaved approximate solution is obtained using a least-squares approach, as in Clarke and Tutty (1994). Conservation of circulation/vorticity is satisfied exactly.

The base flow consists of the free-stream velocity $\mathbf{V}_0(t) = (V_{0x}(t), 0)$ and the velocity field generated by the vortex panels $\mathbf{v}_p(\mathbf{x}, t) = (v_{px}, v_{py})$, the vortices shed into the wake from the trailing edge, and in addition, disturbances introduced into the flow upstream of the airfoil, also in the form of discrete vortices. The Euler equations governing two-dimensional inviscid incompressible flow and the Runge-Kutta method is used to move the vortices, as dsicussed above.

At each time step a new vortex is created a distance 1% of the chord length immediately downstream of the trailing edge. For an airfoil without actuation, the strength of the new vortex is given by,

$$\Gamma_s = -\frac{1}{2}\Delta t(v_a^2 - v_b^2) \tag{2.10}$$

where v_a and v_b are the magnitudes of the velocity tangential to the surface at the trailing edge, as shown in Figure 2.7.

Trailing-edge devices used for lift control act by modifying the flow near the trailing-edge, generating vorticity, which is shed into the wake, and thereby alters the circulation

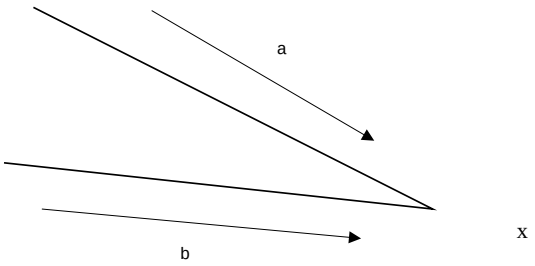

Figure 2.7: Flow at the trailing edge. The $\times$ marks the vortex creation point.

on the body and hence the lift. For example, a trailing edge flap redirects the flow. This can be modeled in a simple manner in the current framework by altering the strength of the new vortex generated at each time step by applying the Kutta condition, which will directly change the way the flow leaves the airfoil at the trailing edge. That is, by generating a new vortex of strength

$$\Gamma_n = \Gamma_s - u \tag{2.11}$$

where u in the control input of the system, with the lift as output. The lift is calculated in standard fashion from the pressure on the surface of the airfoil.

The model outlined above provides a relatively simple (compared to a full Navier-Stokes simulation) but realistic model of the flow and actuation which can be used to investigate control schemes aimed at damping fluctuations in the lift using trailing-edge devices for load control.

The basic panel code was tested against results from standard sources. In particular, the lift coefficients and pressure distributions for inviscid flow past the airfoil obtained from the method presented above were compared with those found using XFOIL (1985), a well validated code commonly used for airfoil calculations. On the basis of the comparison, 404 vortex panels were used. As usual, the panels were clustered towards the trailing-edge, where the curvature is largest.

Chapter 3

ILC Applied to 2D Non-Wake Vortex Model

3.1 Oscillatory Flow (Deterministic)

3.1.1 Flow Structure (Case Flow-1)

Section 3 is aimed at verifying the plant and controller models are functioning correctly before the introduction of the more complex and physically realistic wake model in section 4. The results in this section will establish the flow structures to be analysed, the ILC algorithms to be developed and a fundamental understanding of the practical implementation of smart rotor control. Consider the case with no vortices so that the variation in the lift comes from the variation in the freestream velocity, and the aim is to damp this fluctuation. The flow past the airfoil is assumed to be periodic with velocity,

$$V_{0x} \;=\; 1 + A\sin(2\pi t/T) \tag{3.1}$$

Where all dimensions are non-dimensionalised as discussed in section 2.2, A is the amplitude of the oscillation and T its period. A time step of $\Delta t = 0.005$ is used throughout this section to ensures adequate fidelity for the model parameters used, while keeping the computational runtimes reasonable. Case Flow-1 initiates a period of $T = 0.25$ and $A = 0.1$. An amplitude of $A = 0.1$ is very large relative to the expected amplitude variation on a typical turbine, which is approximately an order of magnitude less during operation. Using a large amplitude and small period is more of a challenge to attenuate so the results hereafter are considered conservative. Since there are no vortices in the flow, the problem is linear in the unknowns (the vortex panel strengths λ_i and source panel strengths κ_i).

3.1.2 Integral-Type ILC

At each step the latest values are used to update the control input. First, consider Integral-Type ILC of the form

$$u^k = u^{k-1} + \mu E^{k-1} \tag{3.2}$$

where u^k is the control input for time step k, and E^k is the error for step k given by

$$E^k = L^k - L_r \tag{3.3}$$

where L_k is the lift at step k and L_r is the target value for the lift, obtained by taking $A = 0$ in (3.1). Figure 3.1(a) shows the control input u_k (green) and the error E^k (red control, blue no control) for the controller in (3.2) with $\mu = 20$. A better result is obtained with a larger gain of $\mu = 50$, as shown in Figure 3.1(b), although, early in the run, there is short term high frequency (time step) fluctuation in the solution. Taking a gain much larger gain causes the scheme to become unstable.

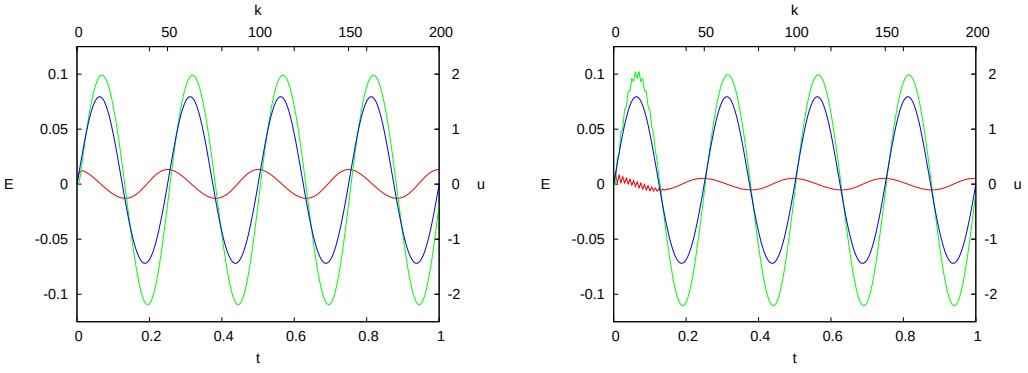

Figure 3.1: Simple Integral-type ILC control with gain (a) $\mu = 20$ and (b) $\mu = 50$. Error; no control (blue), error; control (red) and control input (green).

3.1.3 Phase-lead ILC

The flow has a forced oscillatory component, the effect of which on the lift is only partially damped by the integral control. The oscillation occurs over N_c steps where $N_c = T/\Delta t$. Label the cycles as j, j = 0,1, . . . , and the step within the cycle as $k_c, k_c = 0, 1, ..., N_c - 1$ so that $k = jN_c + k_c$. Consider phase-lead ILC of the form

$$u_j^{k_c} = u_{j-1}^{k_c} + \mu E_{j-1}^{k_c+\Delta} \tag{3.4}$$

where the shift caused by Δ is allowed since the complete signal involved is already known (one of the critical features of ILC; such control action has found widespread use in many successful applications as described in the survey papers Ahn et al. (2007) and Bristow et al. (2006)). As the problem is linear, the stability of the control can be investigated directly.

3.1.4 Stability Analysis

For the phase-lead case in the previous sub-section, as the only vorticity in the flow field is bound to the surface of the vortex panels, the lift may be calculated directly from $L = -V_{0x}\Gamma$, where Γ is the circulation, i.e. the sum of the bound vorticity on the surface, given by $\Gamma = \sum_{i=1}^{N} \lambda_i \Delta_i$. Linearity implies that

$$\Gamma \ = A\, V_{0x} + B\, u \tag{3.5}$$

and

$$L \ = \ - A\, V_{0x}^2 - B\, V_{0x} u \tag{3.6}$$

In discrete form

$$L_j^{k_c} \ = \ - A(V_{0x}^{k_c})^2 - B\, V_{0x}^{k_c} u_j^{k_c} \tag{3.7}$$

and therefore

$$\begin{aligned} E_j^{k_c} &= -A\,(V_{0x}^{k_c})^2 - B\, V_{0xj} u_j^{k_c} - L_r \\ &= -A\,(V_{0x}^{k_c})^2 - B\, V_{0x} u_{j-1}^{k_c} - L_r - \mu B\, V_{0x}^{k_c}\, E_{j-1}^{k_c+\Delta} \\ &= E_{j-1}^{k_c} - \mu B\, V_{0x}^{k_c}\, E_{j-1}^{k_c+\Delta} \end{aligned}$$

Hence

$$\frac{E_j^{k_c}}{E_{j-1}^{k_c}} \ = \ 1 - \mu B\, V_{0x}^{k_c} \frac{E_{j-1}^{k_c+\Delta}}{E_{j-1}^{k_c}} \tag{3.8}$$

Stability in this context is defined as no growth in the forward error used in the ILC algorithm. For $\Delta = 0$, the control will be stable if $0 < \mu B\, V_{0x}^{k_c} < 2$, but the error will decay monotonically only if $0 < \mu B\, V_{0x}^{k_c} \leq 1$. The error changes sign throughout the cycle, so that stability cannot be guaranteed for any other value of Δ. With the maximum value of V_{0x} of 1.1, monotonic decay will be obtained with $\Delta = 0$ if $\mu < 25$, as B = 0.03635. Calculations were performed using this value as a guide, with the results as predicted; for $\mu = 25$ the disturbance was damped almost instantaneously, for values between 25 and 50, the error decayed but with overshoots, while for $\mu > 50$, the error increased monotonically in magnitude over cycles.

The performance of the control with $\Delta = 0$ and $\mu = 10$, with the disturbance decaying to zero and the actuation taking a periodic form, is shown in Figures 3.2(a) and 3.2(b) for times early in the simulation, and for the error at larger times, in Figure 3.2(c).

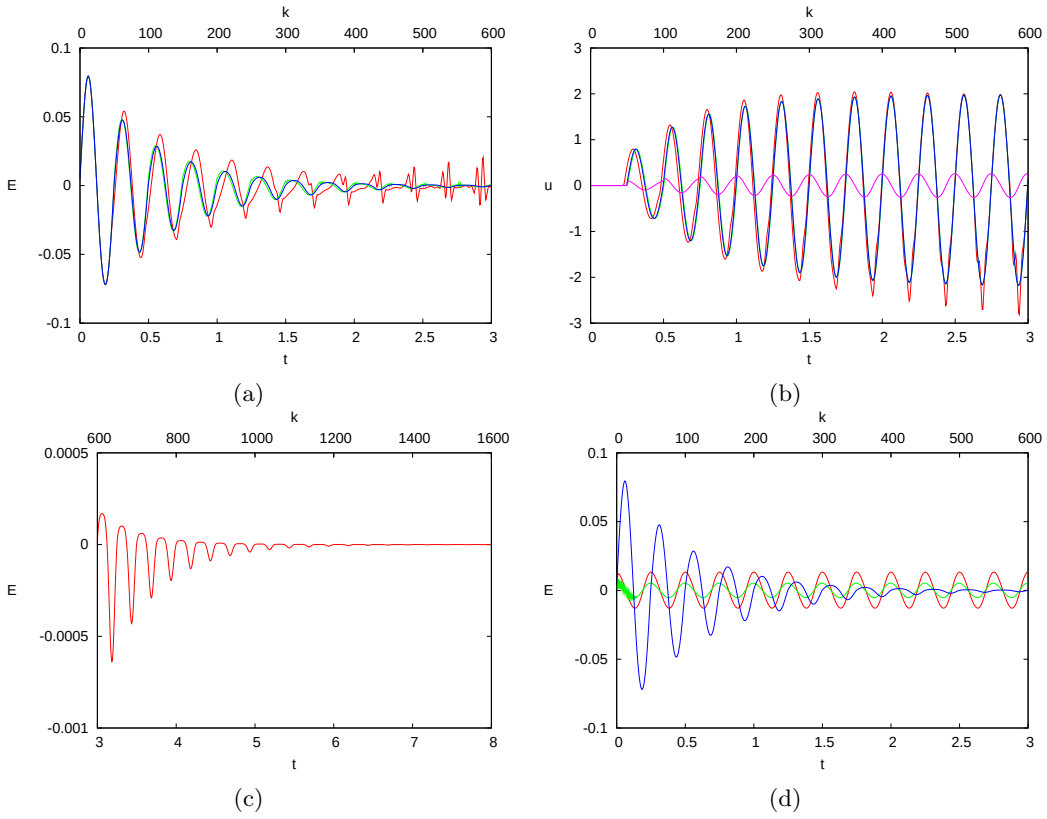

Figure 3.2: Phase-lead ILC with $\mu = 10$ and $\Delta = 0$(blue), $\Delta = -1$(red), $\Delta = 4$(green). (a) Error (b) Actuation (c) extended time for $\mu = 10$ and $\Delta = 0$ (d) Error for Integral-Type, $\mu = 20$ (red), Integral-Type, $\mu = 50$ (green), phase-lead $\mu = 10$ and $\Delta = 0$ (blue)

However, as expected from the stability analysis, the disturbance does not decay to zero for both larger and smaller values of Δ. With $\Delta = 4$ a small, high frequency oscillation, which is growing by $t = 3$, can be seen in the error (Figure 3.2(a) - green). If the calculation is continued, this disturbance grows exponentially in magnitude. Taking Δ = -1 or 1 (not shown), initially the control appears to succeed, as shown in Figures 3.2(a) and (b) - red. However, again there is a high frequency component to the solution which grows as the calculation proceeds. Figure 3.2(b) also shows the change in the control input at each step, $u^k - u^{k-1}$(magenta) for the case with $\Delta = 0$, which operates 90 degrees out of phase with u and at an order of magnitude lower in amplitude. A number of simulations were performed with different parameters (amplitude A, period T, and gain μ), and for all cases with $\Delta \neq 0$, the same pattern was found, with initial decay followed by uncontrolled growth. A comparison of the Error E^k for the different controllers is shown in Figure 3.2(d), showing the superior performance of the phase-lead ILC. Below, $\mu = 10$ will be used for the phase-lead ILC control as it provides good attenuation of the error but with an allowance for non-deterministic effects. Δ is set

to zero in the remainder of this section but kept in the notation as it is standard ILC convention. Additionally, section 4 uses a different flow model and studies the effect of cases with $\Delta \neq 0$.

3.2 Vortical Flow (Non-Deterministic)

3.2.1 Flow Structure (Case Flow-2)

In this section vortices will be introduced into the flow so that the flow is no longer just periodic, although it still has a periodic component from the freestream, the problem is now non-deterministic. The stability analysis for the phase-lead ILC given above does not apply, as it assumes both linearity and periodicity. Consider the flow with an oscillatory freestream with $A = 0.1$ and $T = 0.25$, as above, and with two vortices introduced into the flow upstream of the aerofoil, one with strength $\Gamma = 0.1$ placed at x_{v1} =(−15,0.25) and the other also with strength $\Gamma = 0.1$ but at x_{v2} = (−9,−0.35) at the start of the simulation (t = 0). With these starting values, vortex 1 will pass above the aerofoil and vortex 2 below it, generating a significant disturbance in the lift in addition to that from the oscillation in the freestream velocity. Figure 3.3(a) shows the error for this flow with no control for the time that the vortices are passing the aerofoil. In addition to the oscillation in lift arising from the freestream, large disturbances are generated by the vortices at approximately $t = 10$ and $t = 15$.

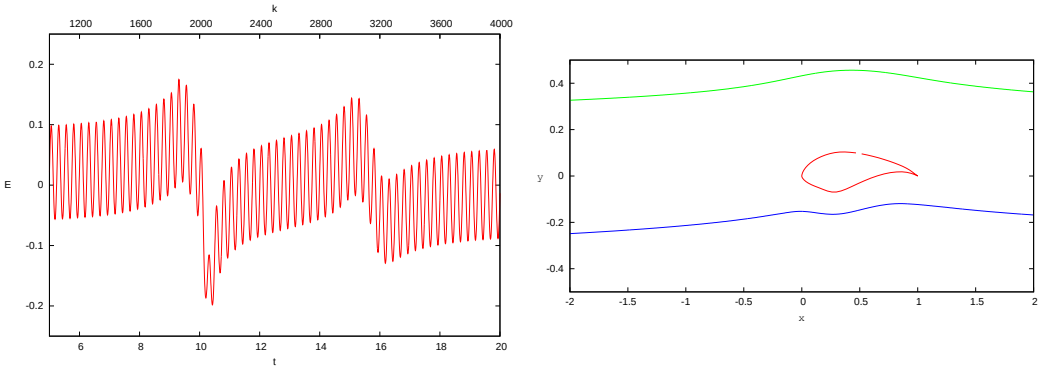

(a) (b)

Figure 3.3: (a) Error for uncontrolled flow with 2 vortices and sinusoidal freestream disturbance (b) Vortex 1 (green) and vortex 2 (blue) centres passing the aerofoil

3.2.2 Two-term ILC

The phase-lead ILC controller (3.4), with $\Delta = 0$ and $\mu = 10$ and a target value of the lift for undisturbed flow ($L_r = 0.379$), was applied to Case Flow-2. This suppressed most of the effect of the oscillation in the freestream, but not the disturbance due to the vortices,

as can be seen in Figure 3.4(b). This is an expected result because the phase-lead control only considers information from the previous cycle and nothing to capture the effects of disturbances within the current cycle. The variation of lift between cycles as the vortices are passing is significant enough to not be captured by the phase-lead ILC. The Integral-type ILC reduced the magnitude of the fluctuations in the lift when applied to the oscillatory flow and when applied to the current case with two vortices, it damps much of the disturbance generated by the vortices but leaves a residual oscillation, as shown for $\mu = 20$ in Figure 3.4(a). This again is expected as we have shown in the previous section that the Integral-type ILC is not capable of completely attenuating the periodic disturbances.

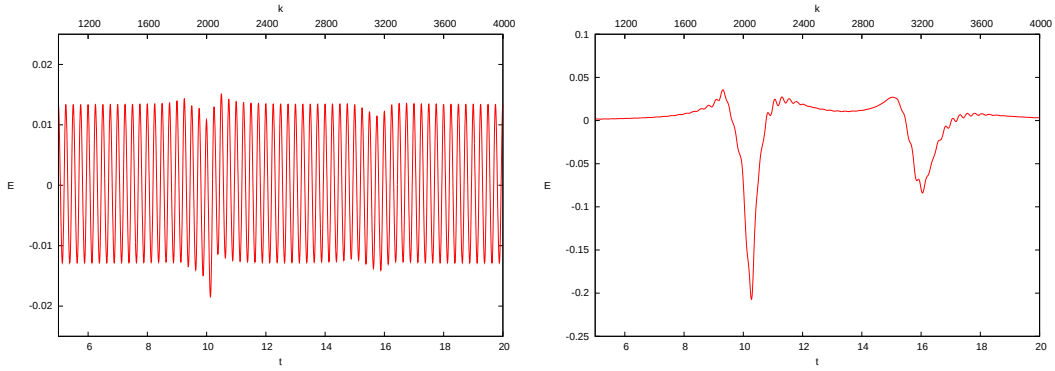

(a) (b)

Figure 3.4: Control applied to flow with sinusoidal disturbance and two vortices, (a) Integral-type ILC $\mu = 20$ (b) Phase-lead ILC $\mu = 10$

This residual oscillation can be largely suppressed by applying a controller incorporating both Integral-type and phase-lead ILC, also referred to as two-term ILC. Specifically,

$$\hat{u}_j^{k_c} = u_{j-1}^{k_c} + \mu_0 E_{j-1}^{k_c+\Delta} \tag{3.9}$$

$$\bar{u}^k = \bar{u}^{k-1} + \mu_1 E^{k-1} \tag{3.10}$$

and

$$u_j^{k_c} = \hat{u}_j^{k_c} + \bar{u}^k \tag{3.11}$$

$k = jN_c + k_c$ as discussed previously in section 3.1.3. The two-term ILC algorithm is a function of both the control input and error from the same point in the previous cycle and the previous time step. The error for this controller with $\mu_0 = 10, \Delta = 0, \mu_1 = 20$ is shown in Figure 3.5(a). The oscillatory component of the fluctuation has been almost completely eliminated, while the disturbance from the vortices has been heavily damped. The control input u^k, shown in Figure 3.5(b), closely tracks the lift for the uncontrolled flow (Figure 3.3(a)), generating a counterbalancing force to the inherent fluctuation in the lift. Increasing the values of the gains above these values did not significantly affect the performance of the controller, and these values will be used for all cases presented

below. Also, taking $\Delta \neq 0$ did not give a stable algorithm, as for the case of pure oscillatory flow.

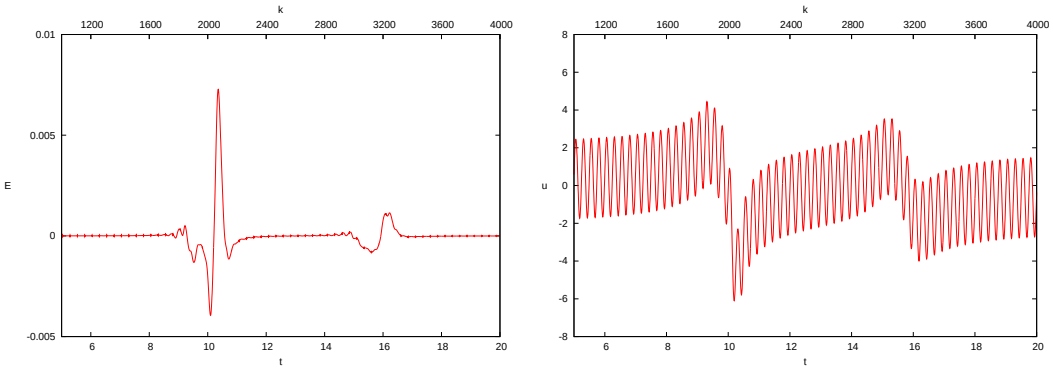

(a) (b)

Figure 3.5: Two-term ILC applied to oscillatory flow with 2 vortices (a) error, (b) control

3.3 Lift Estimator

3.3.1 Lift and Pressure Correlation

Thus far the lift has been used directly from the vortex panel model as an input to the controller. This is not feasible in reality so to bring the analysis a step closer to implementation, the following section analyses the feasibility of using a pressure sensor array configured across the aerofoil to predict the lift and then use this estimate as an input to the controller instead of the actual or direct lift. This can be done in the current vortex panel model because the pressure is available at each vortex panel. To simulate a pressure sensor, the pressure across a particular panel can be used directly. The first step in designing a suitable pressure sensor array to estimate the lift used as the output of the controller, is to understand the correlation between the pressure at different chordwise locations and the global lift. Pearsons correlation factor r_{pL} (as explained in Rogers (1988)) is calculated for all panels to quantify this correlation,

$$r_{pL}[i] = \frac{\sum_{k=1}^{nt}(p_k - \bar{p})(L_k - \bar{L})}{\sqrt{\sum_{k=1}^{nt}(p_k - \bar{p})^2 \sum_{k=1}^{nt}(L_k - \bar{L})^2}} \tag{3.12}$$

where nt = maximum number of time steps; p_k is the panel pressure at time step k; $\bar{p}$ is the mean panel pressure; L_k is the global lift at time k and $\bar{L}$ is the mean global lift. Note that as the modulus of r_{pL} approaches 1, the relationship between the two variables

approaches linearity. The sign of r_{pL} indicates the direction of the correlation. r_{pL} is calculated for all panels, under various different flow conditions, to gain an understanding of which sensor positions are the most suitable for estimating the lift. Linear systems obviously exhibit perfect correlation, i.e. a value of r_{pL}= 1 or -1 for all panels. The more informative cases are when the inflow contains non-deterministic vortex disturbances. Figure 3.6(a) shows the correlation factors for each panel when random actuation is applied to the 2D cross section. Figure 3.6(b) shows the correlation factor for when two vortices are passing the aerofoil.

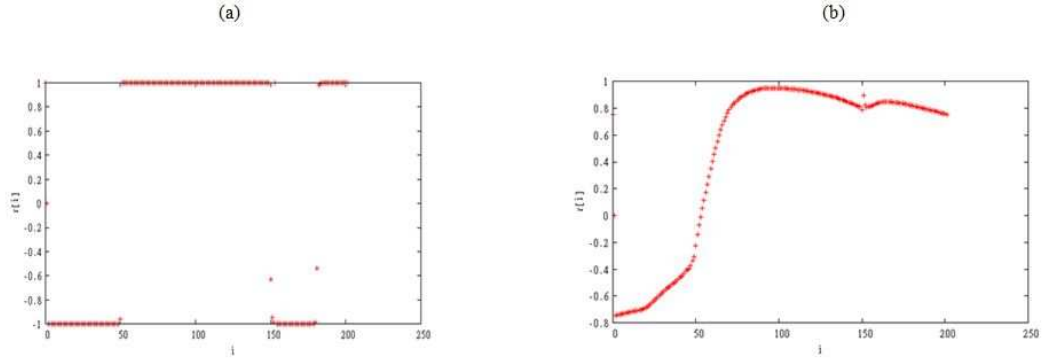

Figure 3.6: Correlation factors for (a) random actuation (b) two vortices

Note that r_{pL} values are calculated for all panel points to gain adequate detail concerning the correlation behaviour across the aerofoil. The co-ordinate system starts at the centre of the suction surface (i=0) and moves to the leading edge (i=100); through the centre of the pressure surface (i=200); then to the trailing edge (i=300) and back to the centre of the suction surface (i=404). As expected, in the deterministic case (random actuation), there is near perfect correlation for all points along the aerofoil. Introducing the non-deterministic effects of the vortices displaces the r_{pL} values away from -1 and 1 correlations. It is clear that the correlation between the lift and the pressure at points around the leading edge drops off when the vortices are introduced (i.e. as $i \rightarrow 100$). Also, there is reduced correlation on the points near the trailing edge (i=300) and the upper aft section ($300 < i < 404$). Figure 3.7 shows a visual representation of the correlation strength across the S825 aerofoil for the 2 vortex case in 3.6(b).

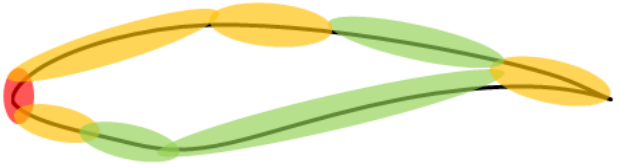

Figure 3.7: S825 Correlation Factor Visual Representation, green = good correlation, orange = ok correlation, red = poor correlation for a flow case with two vortices

The Pearson correlation distribution across the aerofoil varies depending on the vortex structure used. For example, two vortices passing over the top of the aerofoil result in better correlation on the suction surface panels of the aerofoil than the pressure side. Figure 3.8 shows a visual representation of an averaged Pearson correlation for a range of vortex configurations.

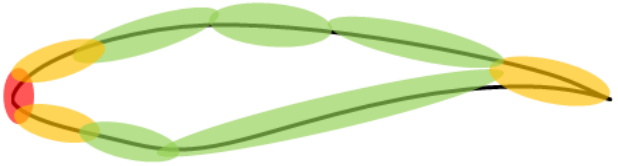

Figure 3.8: S825 Correlation Factor Visual Representation, green = good correlation, orange = ok correlation, red = poor correlation averaged for multiple non-deterministic flow configurations

Overall, it is favourable to place pressure sensors as far away from the leading and trailing egde as possible while retaining enough fidelity to ensure the effect of the vortices are capture as they move along the aerofoil. Larger panel gradients, in relation to the horizontal axis, result in less correlation between the pressure at the panel location and the global lift. This makes sense because vertical panels do not act as lifting surfaces. As the gradient reduces and the panels tend towards the horizontal axis, a greater proportion of the panel is acting in the direction of lift. It therefore makes physical sense that these panels would correlate to the lift more accurately.

Since the lift is calculated as a component of the integral of the pressure across the aerofoil, increasing the number of pressure sensors used to estimate the lift will improve the accuracy of the estimate. It makes sense that the more information we have about the flow, the more accurately we can predict the forces imparted on the aerofoil. The correlation analysis above indicates that measurement points away from the leading and trailing edges yield the best results, and this will be considered when designing pressure sensor arrays as discussed in the proceeding subsection. If we were considering more complex aerodynamic models with boundary layer sub-models, fluctuating shear stress would be considered to obtain information about turbulent wall bounded flow. In the simplified flow model used in this work, the local flow states where the panels are placed are all that is considered. The advantage of using wall pressure fluctuations is that the real world boundary layer can be measured non-intrusively.

3.3.2 Pressure Sensor Arrays

The direct lift cannot be used as the controller output when considering implementation on a turbine, therefore a robust method is required to estimate the lift. Obtaining the complete pressure distribution around a turbine section is not practical; therefore

it is proposed that the lift is estimated from a number of pressures sensor readings at different chordwise positions. Lift is created from the difference in pressures between the upper and lower surface, therefore the lift estimate is based on pressure differences between upper and lower points. The time series pressure measurements can easily be extracted from the flow model for all panel control points. The simplest sensor array is one sensor on the suction surface p_s and one on the pressure surface p_p, where the lift estimate is calculated from $L_e = C_1(p_s - p_p)$. The coefficient C_1 is obtained by running the model with no flow disturbances at the desired angle of attack. The angle of attack varies during a turbine cycle but for simplicity it is assumed that the angle of attack is constant during each simulation throughout this report. This two-sensor array is adequate for global and predictable changes in flow field velocity but does not capture the effects of local pressure changes due to non- deterministic effects, e.g. vortices in the inflow. Figure 3.9 shows the pressure distribution variation as a vortex passes over the aerofoil. The lift fluctuation associated with these changes in pressure is shown in Figure 3.10. To counteract these local pressure changes, more pressure sensors are positioned at different chordwise positions.

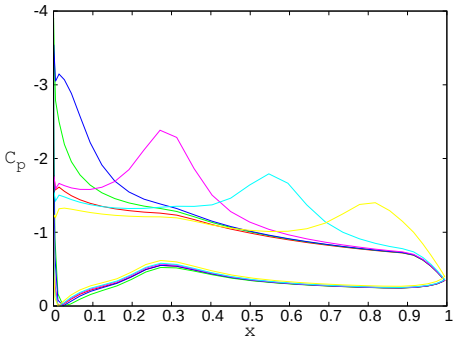

(a) t = 0, red solid; 3.8, green; 4, blue; 4.2, purple; 4.4, light blue; 4.6, yellow

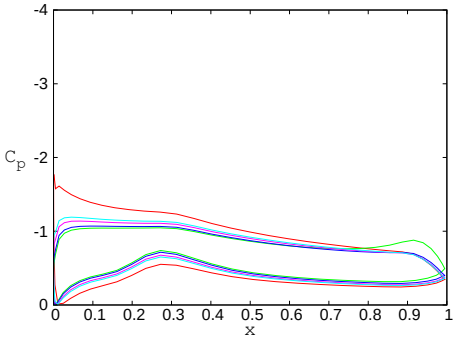

(b) t = 0, red solid; 4.8, green; 5, blue; 5.2, purple; 5.4, light blue

Figure 3.9: Aerofoil pressure distribution at different times showing the effect of a vortex passing the aerofoil. Leading edge ($x = 0$), trailing edge ($x = 1$).

All arrays are arranged reasonably symmetrically, while avoiding points too close to the leading and trailing edge for reasons discussed in the previous section. Figure 3.11 shows the range of pressure sensor arrays used in the subsequent analysis and Table 3.1 the matrix of coefficients $C_{s,p}$ for the 12 sensor array at 7^o AoA.

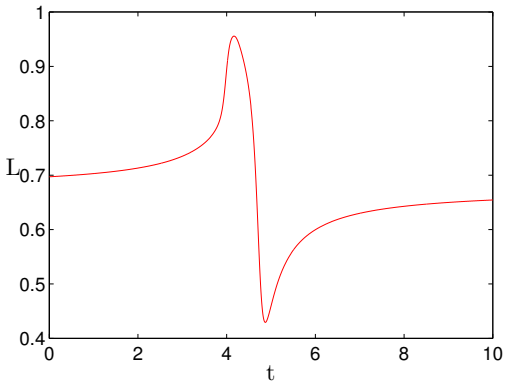

Figure 3.10: Lift fluctuation caused by a single vortex passing the aerofoil (from pressure distribution variations in Figure 3.9)

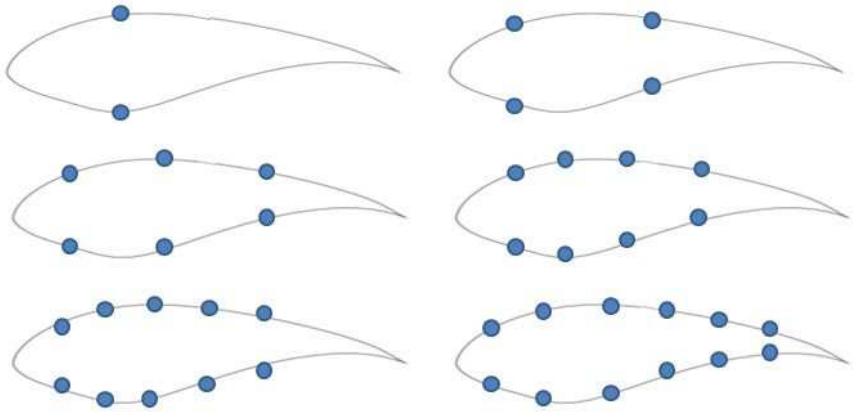

Figure 3.11: Pressure sensor arrays for estimating lift

		Pressure Panel Number					
		107	129	157	195	242	272
Suction Panel Number	95	0.454	0.516	0.625	0.559	0.527	0.722
	73	0.549	0.642	0.821	0.7111	0.660	0.649
	45	0.600	0.713	0.941	0.799	0.736	7.157
	7	0.763	0.955	1.414	1.116	0.996	0.971
	364	0.969	1.302	2.332	1.620	1.379	1.331
	334	1.094	1.538	3.219	2.003	1.648	1.579

Table 3.1: Coefficients for 12 sensor array

The total lift estimate using Q pressure sensors is calculated from the average of the individual lift estimates,

$$\frac{\sum_{s=1....Q/2} \sum_{p=1....Q/2} C_{sp}(p_s - p_p)}{\frac{1}{2}Q^2} \tag{3.13}$$

This calculation assumes a symmetrical distribution of sensors, ie. the same number

of sensors on the upper and lower aerofoil surface. For example, a 12 sensor array will estimate the lift by taking the average of 36 pressure differences multiplied by the corresponding correlation coefficients. 36 pressure differences because 6 sensors on the lower surface for every sensor (x6) on the upper surface, i.e. $\frac{1}{2}Q^2$. The coefficients are calculated from the lift and pressure differences from a simulation with a steady flow and no vortices or control at 7^o AoA, as shown in Figure 3.1.

3.3.3 Validation

The simplest method to validate the lift estimates calculated from the above sensor arrays is to compare the estimated lift from the sensors with the direct lift from the vortex panel method calculation (Equation 2.9), for a range of flow conditions. Figures 3.12, 3.13, 3.14, 3.15 shows comparisons for flow with a periodic disturbance; flow with vortical disturbances; and a combination of both with and without control at a angle of attack of 7^0.

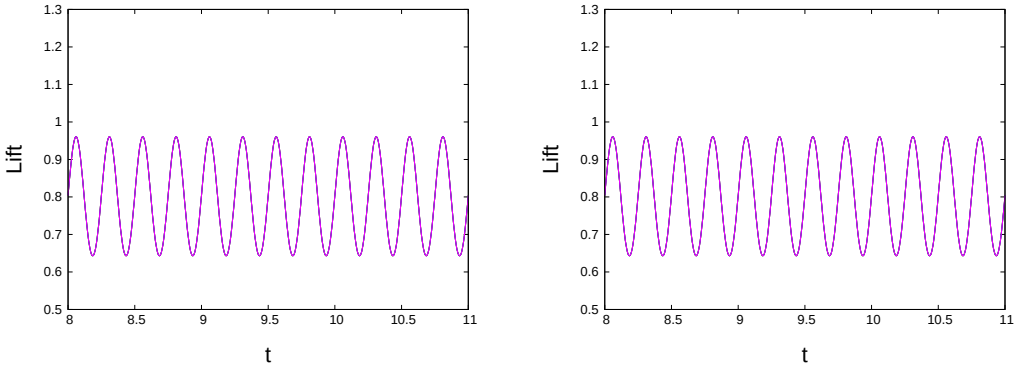

(a) (b)

Figure 3.12: Estimated lift for different pressure sensor arrays for a periodic flow ($T = 0.25$, $A = 0.1$). (a) Direct lift [red], Number of sensors Q = 2 [green]; 4 [blue]; 6 [purple] and (b) Direct lift [red], Q = 8 [green]; 10 [blue]; 12 [purple]

Figure 3.12 shows no error between the estimated lift response, for all sensor arrays, and the direct lift. This result is expected because the model does not contain any nonlinearities, therefore a global change in lift is a result of a proportional change in all pressure measurements at each panel. The only parameter effecting the velocity at each panel is the change in freestream velocity, which effects all panels linearly. By introducing stochastic effects in the form of one vortex, as shown in Figure 3.13, the difference in the accuracy of the lift estimates between each sensor array becomes evident. Using just 2 sensors results in a large peak over prediction of the lift of almost 50% as the vortex passes. However, the peak error begins to rapidly decrease below 10% as the number of sensors increases beyond 4. In Figure 3.13(b) the peak error is at approximately t=9.6 where the estimates appear to lag behind the direct lift. The gradient here is moderate and the peak error does not exceed 5% but as the gradient of the direct lift increases

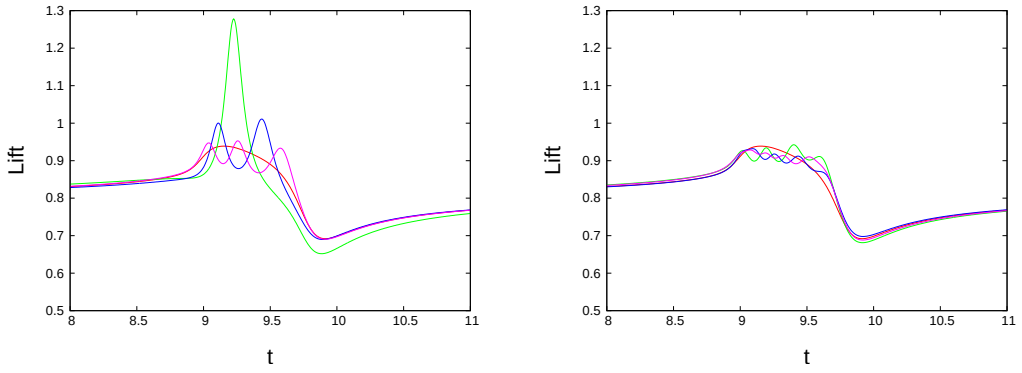

(a) (b)

Figure 3.13: Estimated lift for different pressure sensor arrays for a flow with a vortex passing the aerofoil (strength $\Gamma = 0.1$). (a) Direct lift [red], Number of sensors Q = 2 [green]; 4 [blue]; 6 [purple] and (b) Direct lift [red], Q = 8 [green]; 10 [blue]; 12 [purple]

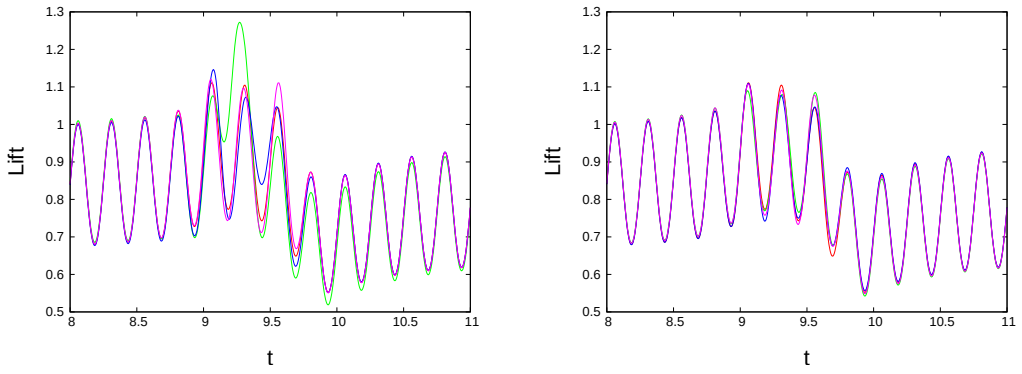

(a) (b)

Figure 3.14: Estimated lift for different pressure sensor arrays for a periodic flow with a vortex passing the aerofoil ($T = 0.25$, $A = 0.1$, $\Gamma = 0.1$). (a) Direct lift [red], Number of sensors Q = 2 [green]; 4 [blue]; 6 [purple] and (b) Direct lift [red], Q = 8 [green]; 10 [blue]; 12 [purple]

in magnitude, the error may become more significant and is something to be aware of when running the simulation for different vortex structures. Figure 3.14 shows the flow condition when the periodic signal and vortex disturbance are combined. The sensors perform well at estimating the lift, with only the case with 2 sensors showing significant deviation from the direct lift (peak error of approximately 40% at t=9.2). It is clear that when estimating the lift for flows with vortices, the two sensor array is not suitable. The peak errors for the other sensor arrays decrease as the number of sensors increases, with the peak error for the 12 sensor array of 4.8% at t=9.7, which is a at a similar time to the peak error for the same array when considering vortex flow only. This implies that adding the periodic disturbance has little effect on the location of the peak error and the vortex is the driving factor behind the quality of the lift estimates. Finally, Figure 3.15 shows the lift estimates when two-term ILC is applied to the periodic vortex flow. A similar trend is seen as more sensors results in greater accuracy in the lift estimate.

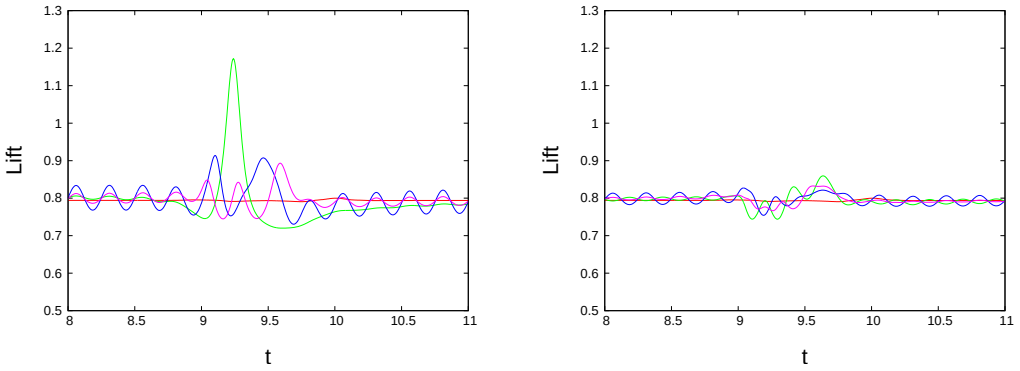

(a) (b)

Figure 3.15: Estimated lift for different pressure sensor arrays with two-term ILC applied to the disturbance in Figure 3.14. (a) Direct lift [red], Number of sensors Q = 2 [green]; 4 [blue]; 6 [purple] and (b) Direct lift [red], Q = 8 [green]; 10 [blue]; 12 [purple]

The lift estimate responses have been simulated for a range of flow (periodic inflow and vortices) and control (random, ILC with different parameters) configurations and all have resulted in similar patterns of accuracy with peak errors not exceeding much more than 5% for the 12 sensor array.

As mentioned, the optimum sensor array positions the sensors away from the leading and trailing edge while maintaining adequate fidelity along both surfaces to capture the effect of the vortices. When trying to attenuate both sources of disturbance (global lift and local vortices), it is worth balancing these two conflicting requirements to optimise the estimate for a particular application. Pressure sensor distribution of an even density have been used because results using density variations discovered poor estimates of the lift driven by a votex moving into an area of reduced sensor density. Assuming a clockwise moving vortex passing over the upper surface of the aerofoil, this makes physical sense because in an area of high density sensors, the effect of the lift will be amplified and as the vortex passes an area of reduced density the relative influence of the vortex will be reduced. This causes the estimator to under and over predict the lift as a vortex passes.

3.3.4 Two-term ILC (Case Flow-2)

To understand the effectiveness of the ILC controller when using the estimated lift, the estimated lift is used as the input to the two-term ILC control law. Results for all sensor arrays are shown for the flow condition (oscillatory flow, 2 vortices case flow-2) and two-term ILC ($\mu_0 = 10, \Delta = 0, \mu_1 = 20$) from Figure 3.5 with the aerofoil set at 7^o. Figure 3.16 shows the error response when using the lift estimates from each array compared to the controller using direct lift.

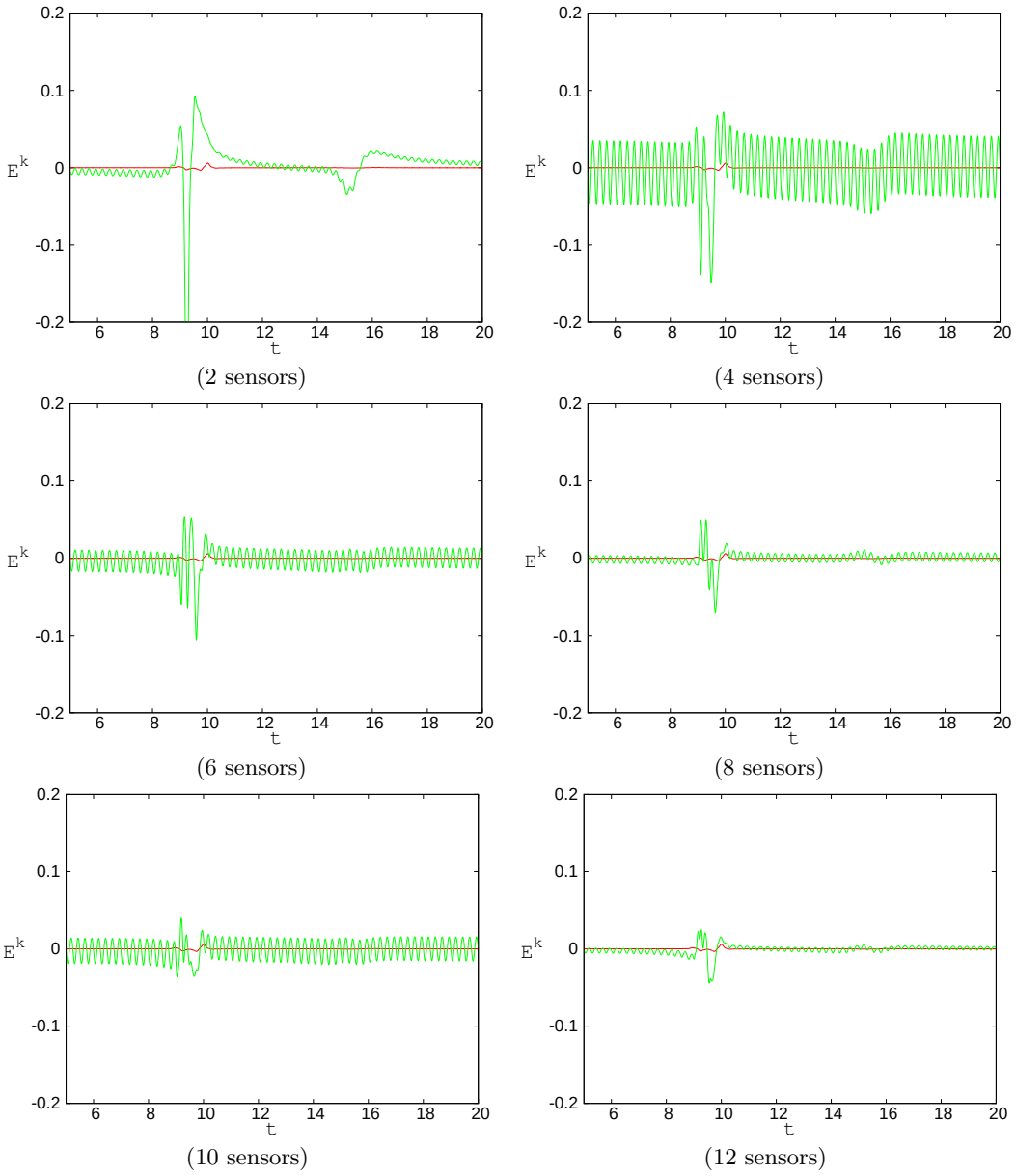

Figure 3.16: Error response when using two-term ILC ($\mu_0 = 10, \Delta = 0, \mu_1 = 20$) with different pressure sensor arrays (green) for a oscillatory flow with 2 vortices ($T = 0.25, A = 0.1, \Gamma = 0.1$) compared to direct lift (red)

The error responses indicate a general trend that the more sensors used, the greater the reduction in peak error (L_∞) and overall deviation from 0 error (L_2). The marginal exception to this trend is the attenuation of the periodic oscillation when using 10 sensors, which appears to be slightly less than when using 8 sensors. This could be due to the lack of array optimisation when positioning the sensors for the 10 sensor array and refining the sensor locations would improve results further. Figure 3.17 shows the L_2 and L_∞ reduction percentages for the cases in Figure 3.16. The corresponding L_2 and L_∞ values for the controller using direct lift for the same flow are 0.5% and 1.9% respectively.

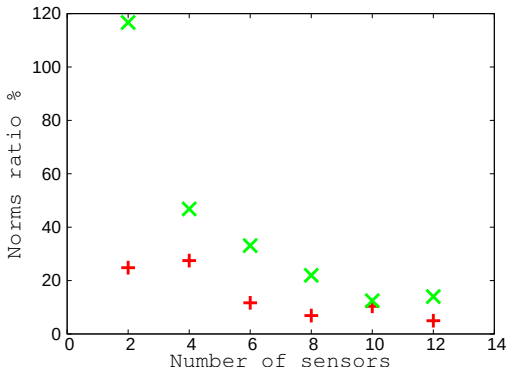

Figure 3.17: Norm ratio % (100 * controlled norm / uncontrolled norm) for different pressure sensor arrays: L_2 (red) and L_∞ (green). Flow: $A = 0.1$, $T = 0.25$, 2 vortices, $\Gamma = 0.1$. Control: two-term ILC ($\mu_0 = 10, \Delta = 0, \mu_1 = 20$)

Increasing the number of sensors improves the accuracy of the lift estimation and results in improved load reduction, with the greatest reduction, using 12 sensors, of approximately 5%(L_2) and 14%(L_∞) of the uncontrolled case. In practical terms, the number of pressure sensors chosen will depend on the turbine cost model and whether the turbine design drivers are the fatigue or extreme loads. If the fatigue loads are the design driver then potentially less pressure sensors can be deployed as the results in Figure 3.17 indicate reasonable fatigue load reduction with fewer sensors. If extreme loads are the design driver then more sensors would be required as Figure 3.17 indicates poor extreme load reduction for cases with four or less sensors. Section 3.9 (complete model) incorporates the lift estimator for realistic turbine conditions over large run times to add evidence that the lift estimation technique is stable and accurate for the intended purpose.

3.4 Flow Configurations

A controller has been successfully designed for deterministic and non-deterministic flow structures using both the direct and estimated lift with the intent of establishing code and analysis methods that will be developed in more detail in section 4. The analysis in previous sections has focused on a few specific cases but does not test the robustness of the controller for a range of variation in flow parameters. In this section, each parameter will be varied in turn and results for the complete model are shown in section 3.8. Varying the angle of attack, vortex strength, number of vortices, target lift and permutations of these variables will add further verification evidence that the plant model responds as expected. Figure 4.3 shows the parameter settings for the representative test cases (note the flow cases numbers are a continuation from the previous sections). Initially,

the same two-term ILC as described above is applied ($\mu_0 = 10$, $\Delta = 0$ $\mu_1 = 20$) using the direct lift.

Case	Description	Vortex strength	AoA	Amplitude	Period	Target Lift
5A	AoA+	medium	7°	0.1	0.25	0.801
5B	AoA-	medium	−7°	0.1	0.25	-0.024
6	Vortex Strength +	strong	7°	0.1	0.25	0.801
7A	Period +	medium	0°	0.1	10	0.379
7B	Period +, AoA +	medium	7°	0.1	10	0.801
8	Target Lift +	medium	0°	0.1	0.25	0.474
9	Multiple Vortices	weak x 12	0°	0.1	20	0.379

Table 3.2: Flow Configurations for Robustness Test of Two-Term ILC with gains $\mu_0 = 10, \Delta = 0, \mu_1 = 20$

Case	Description	norm	ratio x 100
5A	AoA+	$\mathcal{L}_2$	1.9%
		$\mathcal{L}_\infty$	0.7%
5B	AoA-	$\mathcal{L}_2$	6.4%
		$\mathcal{L}_\infty$	2.3%
6	Vortex Strength +	$\mathcal{L}_2$	4.2%
		$\mathcal{L}_\infty$	9.1%
7A	Period +	$\mathcal{L}_2$	0.5%
		$\mathcal{L}_\infty$	2.5%
7B	Period+ AoA+	$\mathcal{L}_2$	0.2%
		$\mathcal{L}_\infty$	0.9%
8	Target Lift +	$\mathcal{L}_2$	1.2%
		$\mathcal{L}_\infty$	2.9%
9	Multiple Vortices	$\mathcal{L}_2$	0.5%
		$\mathcal{L}_\infty$	9.3%

Table 3.3: Performance Metrics for Robustness Test of Two-Term ILC with gains $\mu_0 = 10, \Delta = 0, \mu_1 = 20$

3.4.1 Steady State Angle of Attack (Case Flow-5A and Flow-5B)

For case flow-2 (section 3.2), the two-term ILC produces a reduction of two orders of magnitude in L_2, and a value of L_∞ less than 3% of that for the uncontrolled flow, and is the flow condition used in the previous two chapters. The aerofoil is at zero degrees angle of attack in case flow-2. Pitch control (adjusting the AoA) can be used in order to maintain a near constant loading on the turbine as the mean flow rate varies so it is likely the aerofoil will operate across a range of different angles of attack. For 7^o AoA, with the same flow parameters as above and two vortices starting in the same positions, the values of L_2 and L_∞ slightly improve with an increase in reduction to $1.9\%(L_2)$ and $0.7\%(L_\infty)$. In this case the target value $Lr = 0.801$, obtained from running the code with undisturbed flow, $V_{0x} = 1$ and 7^o AoA. The fact the uncontrolled performance metrics are higher for an increase in AoA is the reason behind the reduced metrics ratio. Repeating the simulation with the same conditions and controller with the exception of the AoA been set to -7^o, results in much higher performance metrics. This is understandable because the initial no-controller case metrics are much smaller. The controller appears to be stable across different steady state changes in AoA with a

similar level of effectiveness when vortices are present. The range of AoA chosen roughly represents the typical range the aerofoil will operate in under normal conditions with attached flow.

3.4.2 Vortex Strength (Case Flow-6)

A more extreme case is obtained by changing the strength of vortex one to $\Gamma = 0.4$. As this vortex contains (in magnitude) approximately half of the circulation of that bound to the aerofoil in the reference condition, this case can be regarded as a very severe test of the control scheme. The error for the uncontrolled case is shown in figure 3.18(a) and that with the two-term ILC in figure 3.18(b).

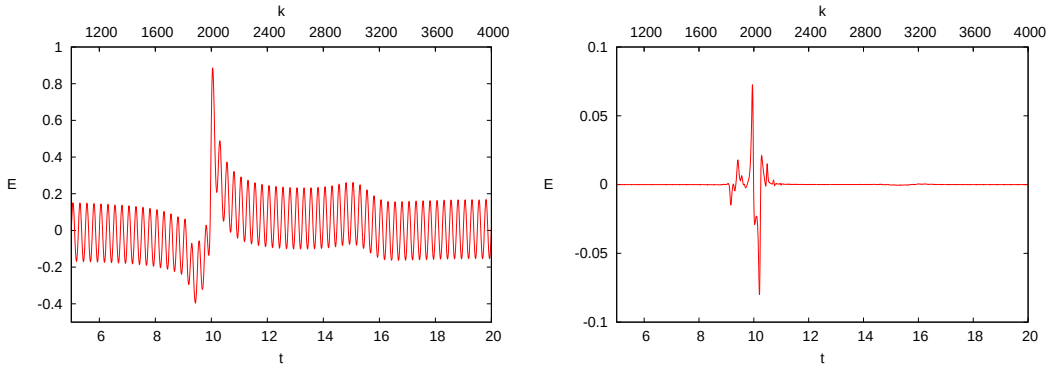

(a) (b)

Figure 3.18: Case Flow-6 response - (a) uncontrolled error and (b) two-term ILC applied

There is now a much larger deviation from the reference value of the lift, with the maximum value of the lift more than double the reference value, reflecting the strength of vortex 2, but, again, given the extreme nature of this test, the control performs very well. Note the change in the E^k axis scale in Figure 3.18(b), emphasising the significant reduction in the peak load. However, for both L_2 and L_∞, the values with the control relative to those for the uncontrolled case (case 6, 3.3) are larger than for the original two vortex case (i.e. that with $\Gamma_2 = 0.1$).

3.4.3 Variable Period Flow (Case Flow-7A and Flow-7B)

As mentioned above, both the chord length H and the reference velocity V_∞ vary along a turbine blade, which implies an increase in the nondimensional period of the oscillation T, moving towards the tip. All the calculations so far have used T=0.25 which represents a relatively fast rotating, unsteady flow where the frequency of the vortices to period of rotation is smaller than would be expected on an actual turbine. This enabled the interaction between the forced oscillation, the convective disturbance represented by the vortices and the control scheme to be investigated with a relatively small computational

effort, but in practice, T would be much larger and therefore a higher frequency of stochastic disturbances per period. Figure 3.19(a) shows the error for a run with two vortices, no control, 0∘ AoA and $T = 10$, over the time that the vortices pass the aerofoil (case flow-7A, 3.3).

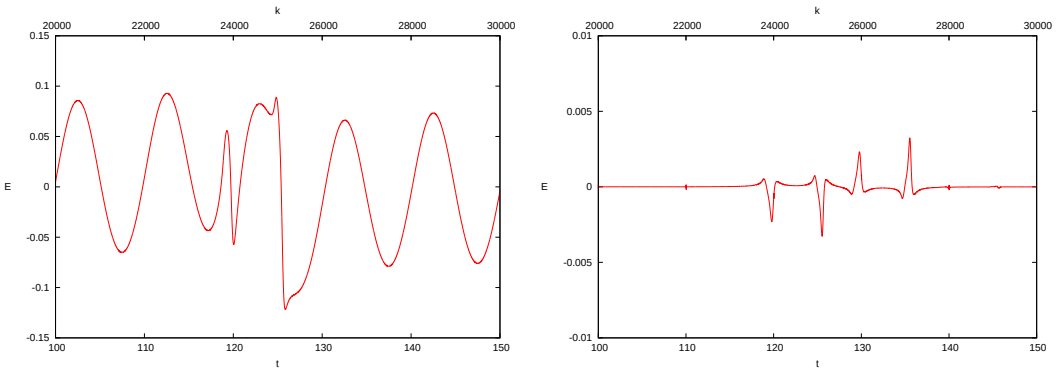

(a) (b)

Figure 3.19: Error E^k for oscillatory flow past the aerofoil at 0^o AoA with two vortices, T=10 and (a) no control (b) two-term ILC

The vortices now start much further upstream, at (125,0.25) and (119,0.25), both with strength $\Gamma = 0.1$. Again there is a relatively large fluctuation as the vortices pass, but this now occurs over a short time relative to the period. Figure 3.19(b) shows the same case with the two-term ILC. Note the change in the E^k axis scale in Figure 3.18(b), emphasising the significant reduction in the peak load. Again the disturbances are largely attenuated, with a two order of magnitude reduction in L_2 and L_∞. Figures 3.20(a) and 3.20(b) show the error without and with control for a similar case but with the aerofoil at 7^o.

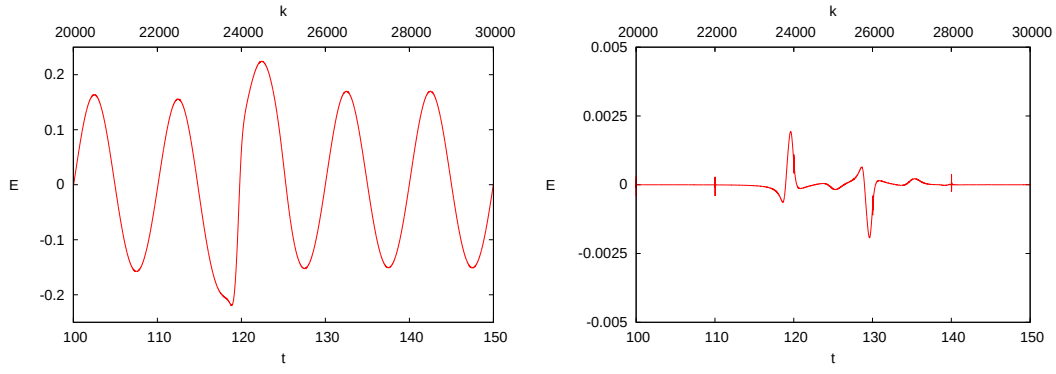

(a) (b)

Figure 3.20: Error E^k for oscillatory flow past the aerofoil at 7^o AoA with two vortices, T=10 and (a) no control (b) two-term ILC

3.4.4 Target Lift (Case Flow-8)

The reference value used in the results presented above is the lift on the aerofoil with a steady mean velocity, but there is also interest in using smart blades to increase aerodynamic performance, particularly at low speeds. A number of simulations were run using different values as the target. Figure 3.21(a) shows the error when the control is applied to a flow with A = 0.1 and T = 0.25 and two vortices passing the aerofoil (as for case 2) but with a target value of the lift of $Lr = 0.474$, 25% higher than the value for uniform flow.

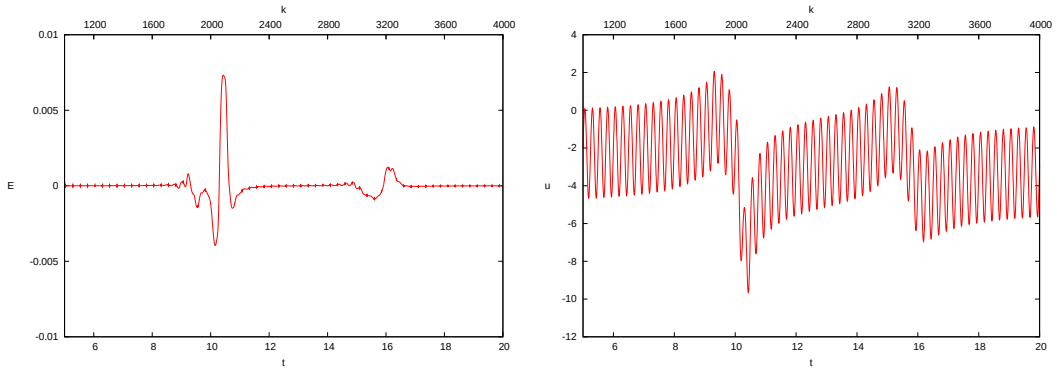

Figure 3.21: Case flow-8 for oscillatory flow with 2 vortices and 25 % increase in L_r, with two-term ILC applied. (a) Error E^k (b) Actuation u^k

This figure is similar to that for the case with the original (lower) reference value, and gave similar values for the performance measures, (case 6, Table 5.2), where the values of the measures with no control were obtained from a simulation with the value for the actuation $u^k = 2.616$, which produces the target value in the case with uniform flow (no vortices and $V_{0x} = 1$). Figure 3.21(b) shows the control signal u^k for this case. It is very similar to the case with the original reference value, but displaced downwards to compensate for the increase in the target value.

3.4.5 Multiple Vortices (Case Flow-9)

For all the results presented so far, only a few strong vortices have been used, generating large disturbances in the flow. Figure 3.22 shows the fluctuation in the lift for a run with 12 relatively weak vortices ($\Gamma_j = \pm 0.005$) as the vortices pass the airfoil when there is no actuation ($u^k = 0$), and period of $T = 20$ and a 5% amplitude in the freestream velocity oscillation ($A = 0.05$). In this case, the vortices generate relatively weak changes in the lift, superimposed on the oscillation from the unsteady nature of the freestream. Figure 3.23 shows the error in the lift with the two-term ILC. Again there is a two order of magnitude reduction in $\mathcal{L}_2$, but only an order of magnitude reduction in $\mathcal{L}_\infty$ (case 6, Table 4.3). The final level of the error signal is, however, similar to that found in other

cases with stronger disturbances, and is still acceptable. Figure 3.24 shows the control signal u^k for this case. It is similar in form to the error for the flow with no control, i.e. essentially oscillatory but with relatively short-scale fluctuations generated by the vortices.

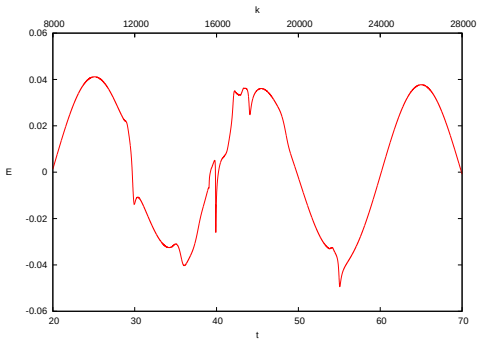

Figure 3.22: The error E^k for oscillatory flow past the airfoil at 0° AoA with 12 vortices, $T = 20$, and no control.

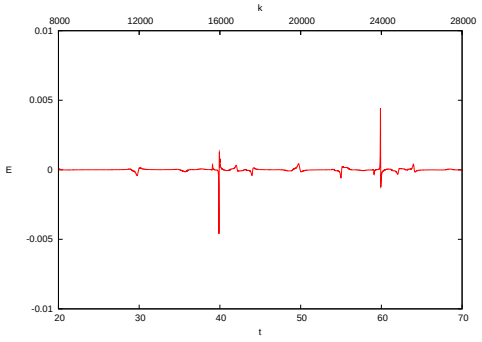

Figure 3.23: The error E^k for oscillatory flow past the airfoil at 0° AoA with 12 vortices, $T = 20$, and the controller (4.5)–(4.7) with $\mu_0 = 10$, $\Delta = 0$, and $\mu_1 = 20$.

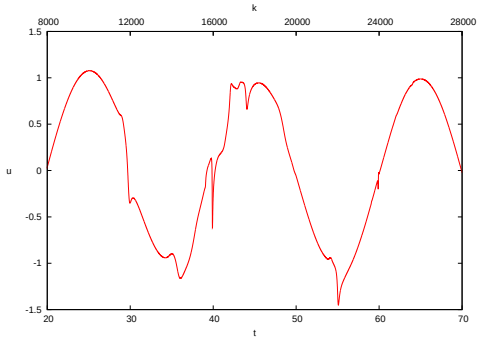

Figure 3.24: The control input u^k for oscillatory flow past the airfoil at 0° AoA with 12 vortices, $T = 20$, and the controller (4.5)–(4.7) with $\mu_0 = 10$, $\Delta = 0$, and $\mu_1 = 20$.

3.5 Real Turbine Data (Non-Deterministic)

This section focuses on integrating the previous sections sub-models of the smart rotor system. The fundamental flow physics remains the same but a complete model will consist of a realistic flow structure and representative sensor characteristics. The development of the complete model will consist of applying two-term ILC to (a) a realistic inflow disturbance of the freestream velocity; (b) the addition of multiple vortices in the inflow; and (c) replacing the direct lift with the lift estimator developed in section 3.5. The final model will include the effects of all sub-models (a)-(c) and enable a summation on the effectiveness of two-term ILC for attenuating disturbances in simple, attached flows representative of those experienced by wind turbine smart rotors. Evolving the analysis in this way enables insight into the coupling between assumptions made about the plant or controller model that may lead to inadequate performance. The development of a complete model for the non-wake flow model adds further verification of the plant and controller models in a computational efficient manner.

Using the non-dimensional method discussed in section 2.2, a smart rotor 2D cross section with a chord of 1m at an outboard radial blade position typical of a smart rotor would have a period of approximately 200t and above for the disturbance in freestream velocity. This timescale is very large and computational inefficient, therefore a representative period of T=20t will be used in this section. Figure 3.25 shows the real turbine data from Thomsen et al.(2008) scaled to an approximate period of T=20 and A=0.1 and the baseline two term ILC developed in section 3.2. The period and amplitude are fluctuating in a manor representative of actual turbine inflow data.

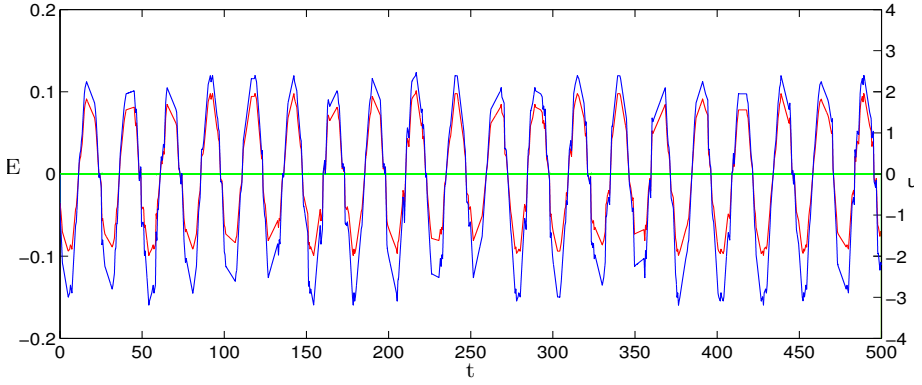

Figure 3.25: Two-term ILC applied to non-dimensionalised real turbine data (Case Flow-10) with $\mu_0 = 10$, $\Delta = 0$, and $\mu_1 = 20$, uncontrolled error (red), controlled error (green) and control input (blue)

A similar case has previously been analysed in section 3.4.6 and the data in Figure 3.25 similarly shows very good attenuation with performance metric ratios of 1.21% (L_2) and 0.11% (L_∞). It is reasonable to expect the controller to perform well with this inflow because analysis has already shown that the two-term ILC algorithm is adept at coping

with fluctuations in the freestream velocity period and amplitude variations aligned with those found in real turbine data.

The addition of vortices in previous sections has introduced stochastic effects into the system and the same method is applied here. Fifty vortices are introduced upstream of the aerofoil to ensure a vortex arrives at the aerofoil leading edge every $10t$. All vortices have the same strength of 0.01 and start every $10x$ on the horizontal position but the y starting position is randomised to ensure a random distribution of vortices above and below the aerofoil. Figure 3.26(a) shows the system response when the baseline two-term ILC is applied to the flow structure with fifty vortices. Figure 3.26(b) shows a more detailed plot of the inflow disturbance with and without vortices. The norms for this case are 1.9% (L_2) and 0.8% (L_∞) which is only a small increase compared to the metrics found for the non vortex case.

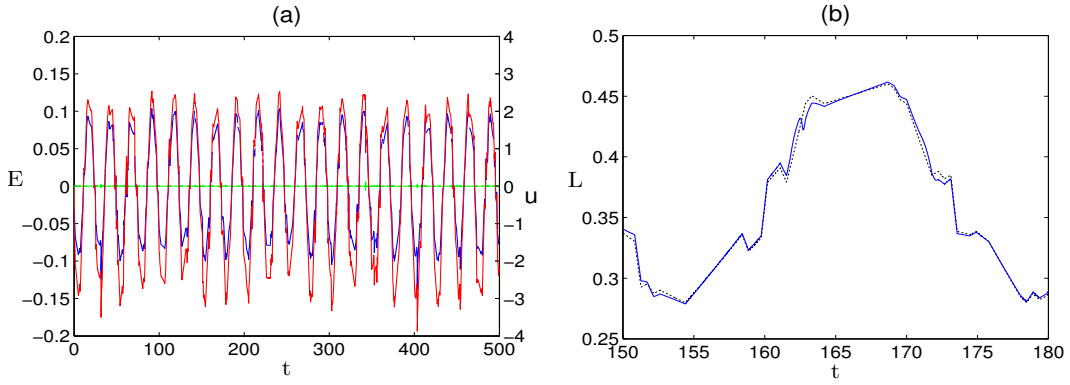

Figure 3.26: (a) Two-term ILC ($\mu_0 = 10$, $\Delta = 0$, and $\mu_1 = 20$) applied to real turbine data with fifty vortices uncontrolled error (red), controlled error (green) and control input (blue). (b) Lift disturbance no vortices (dashed grey), vortices (blue)

The controller used in all of the simulations in this section thus far have utilised the direct lift from the model. In section 3.5, a 12 sensor array was developed and the same sensor array is now used in the two-term ILC algorithm in the presence of the flow disturbance shown in Figure 3.26. Figure 3.27 shows the system response when replacing the direct lift with the estimated lift. As expected the level of attenuation drops when compared to the direct lift control but performance metrics are still reasonable with values of 2.8% (L_2) and 3.2% (L_∞).

3.6 Summary

Section 3 has successfully applied different forms of ILC to a range of flow conditions with the additional of smart rotor sensor dynamics. The flow model is a simple vortex

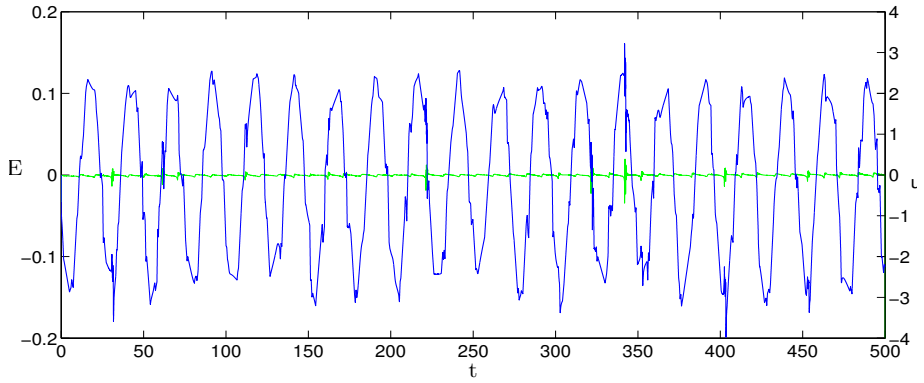

Figure 3.27: Two-term ILC ($\mu_0 = 10$, $\Delta = 0$, and $\mu_1 = 20$) applied to real turbine data with fifty vortices using a lift estimate as the controller input, controlled error (green) and control input (blue)

panel method without a wake model that is only suitable for attached flow but stochastic aerodynamic effects have been introduced to the system with the incorporation of upstream discrete vortices. The flow model is rudimentary in comparison to the full wake model developed in section 4. However, analysis using this model has value in verifying the base flow model, controller model development, lift estimation techniques and establishing different flow conditions. The simple non-wake model has the advantage of fast computation for a large number of flow and controller permutations. The principle reason for including this model in the thesis is to gain evidence that the flow model calculates circulation correctly for a range of flow conditions and that ILC can be applied to a flow model successfully. Section 4 then develops these principles using a more physically representative flow and smart rotor system model.

Initially Integral-type and phase-lead ILC were developed and applied to simple oscillatory disturbances in the freestream velocity. These algorithms were adequate when attenuating a simple deterministic system but performance significantly reduced with the introduction of stochastic vortices. A solution was developed to combine the two forms of ILC into a two-term ILC algorithm that could account for the vortical disturbances using the Integral-type ILC and the freestream oscillations using the phase-lead ILC. The simple structured two-term ILC performed well when considering the system outputs only. The results indicate good two-term ILC performance across a range of stochastic flow conditions. The same controller was tested for approximately 100 flow test cases with various different combinations of period, amplitude and vortex distribution. All performance measures fell below 10% of the uncontrolled case.

Chapter 4

ILC Applied to 2D Wake Vortex Model

4.1 Oscillatory Flow (Deterministic)

4.1.1 Flow Structure (Case Flow-11)

This section develops the aerodynamic plant model to include the effect of the aerofoil wake. The wake model is discussed in detail in section 2. The addition of the wake effect enhances the dynamic response of the plant model and enables physically meaningful conclusions to be drawn. This section will develop in a similar manner to section 3 with an array of additional deterministic and non-deterministic flow structures. As in section 3, consider the case with no vortices hence the variation in the lift comes from that in the free stream velocity, and the aim is to damp this fluctuation. The flow past the airfoil is assumed to be periodic with velocity,

$$V_{0x} \;=\; 1 + A\sin(2\pi t/T) \tag{4.1}$$

where A is the amplitude of the oscillation and T its period. A time step of $t = 0.005$ is used, with amplitude $A = 0.1$, and a period of $T = 2.5$. A period 10 times greater than in the previous chapter is used because it represents a more realistic case (i.e. the period is approximately 1/3 of the time taken for the lift to reach steady state) without significantly increasing computational effort. This condition is still not representative of a real turbine, as the turbine period is much larger than the time taken for the lift to reach steady state (i.e. the Wagner effect) but this initial condition represents an extreme case for the controller to be tested within reasonable computational requirements. The initial vorticity on the airfoil is preset to the vorticity expected for the target lift under steady conditions. This is an assumption that the starting vortex has passed far enough

downstream to assume the bound vorticity on the airfoil is constant and equal to that expected at the target lift. Hence the Wagner effect is not present at the start of the simulations, which is suitable as this work focuses on a wind turbine during continuous operation.

4.1.2 Proportional Controller

Previous work (Tutty et al., 2013) and Chapter 3 used an Integral-type ILC controller as an initial approach to attenuate the periodic disturbance in (4.1). This control scheme is essentially an integral type controller and simulates a wake type effect in the model. The present flow model now includes a wake model, therefore using an integral type controller again would lead to double counting of the wake effect and the model delivering unreliable results. Consequently a proportional controller is initially used to attenuate the periodic disturbance. The addition of the wake model means the system is fully nonlinear and at each time step the latest values are used to update the control input,

$$u^k = \mu E^{k-1} \tag{4.2}$$

where u^k is the control input for step k, and E^k is the error for step k given by

$$E^k = L^k - L_r \tag{4.3}$$

where L^k is the lift at step k and L_r is the target value for the lift, obtained by taking $A = 0$ in (4.1).

Figure 4.1 shows the control input u_k and the error E^k for the controller (4.2) with $\mu = 50$. Also shown is the error with no control. Improved attenuation is obtained with a larger gain of $\mu = 240$, as shown in Figure 4.2. Taking a gain much larger causes the scheme to become unstable. The effect of the wake model can be seen in the phase difference between the control input and the error for the uncontrolled cases in Figures 4.1 and 4.2.

4.1.3 Phase-lead ILC

The flow has a forced oscillatory component, the effect of which is only partially damped by the proportional control. This operates over N_c steps where $N_c = T/\Delta t$. The cycles are labelled as j, $j = 0, 1, \ldots$, and the step within a cycle as k_c, $k_c = 0, 1, \ldots, N_c - 1$, so that $k = jN_c + k_c$. Consider phase-lead ILC of the form

$$u_j^{k_c} = u_{j-1}^{k_c} + \mu E_{j-1}^{k_c+\Delta} \tag{4.4}$$

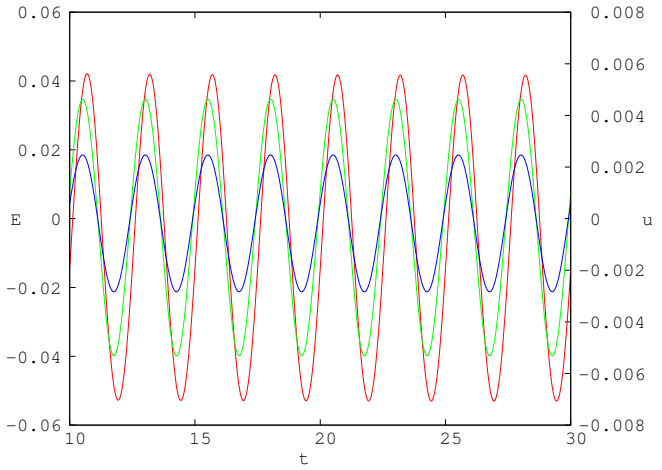

Figure 4.1: Controller (4.2) with $\mu = 50$. Error E^k with no control, $u^k = 0$ (red). Error E^k with control (blue). Control input u^k (green)

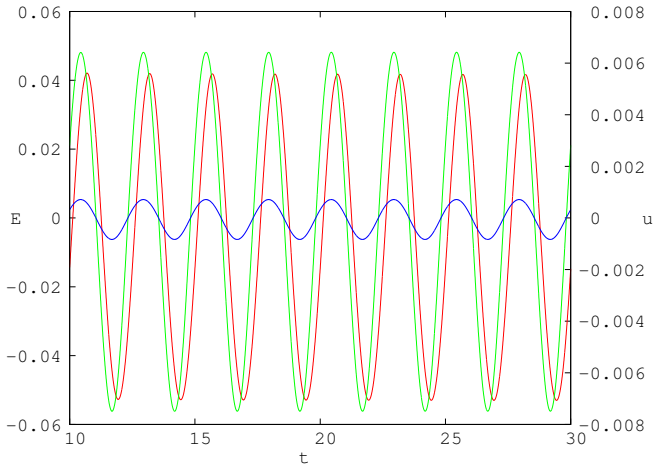

Figure 4.2: Controller (4.2) with $\mu = 240$. Error E^k with no control, $u^k = 0$ (red). Error E^k with control (blue). Control input u^k (green).

where the shift caused by Δ is allowed since the complete signal involved is already known (one of the critical features of ILC; such control action has found widespread use in many successful applications as described in the survey papers Ahn et al. (2007) and Bristow et al. (2006)). The performance of the control with $\Delta = 0$, $\mu = 5$ and $\mu = 25$ is shown in Figure 4.3. Increasing the value of μ improves attenuation but for values of μ above 25 the controller becomes unstable.

4.1.4 Variable Δ

It has been shown in previous work (Tutty et al., 2013), that for a linear aerodynamic model, the system becomes unstable for all conditions where $\Delta \neq 0$. As the aerodynamic model is now fully nonlinear, it is no longer possible to perform a suitable stability analysis therefore a few cases with different values of Δ are simulated with results for

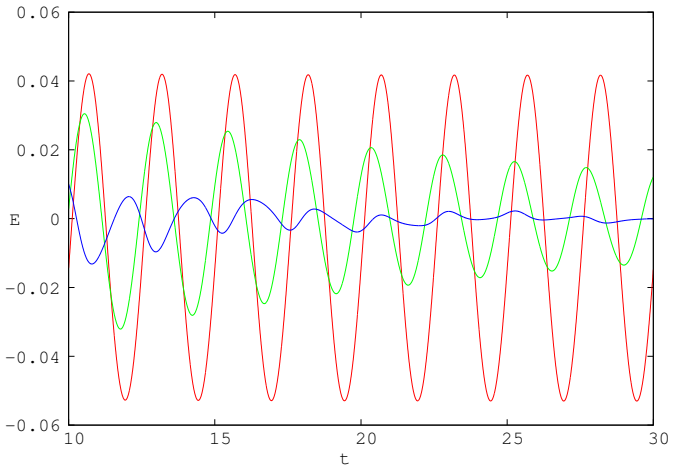

Figure 4.3: Controller (4.4) showing error E^k for no control $u^k = 0$ (red), $\mu = 5$ (green) and $\mu = 25$ (blue).

$\Delta = 4$ and $\Delta = 8$ shown in figure 4.4 for controller (4.4) with $\mu = 25$. Above values of $\Delta = 8$ the controller starts to become unstable and negative values of Δ indicate a deteriation in performance. However, a greater level of robustness to varying values of Δ is observed when the wake is accounted for in the flow model. A number of simulations were performed with different parameters (amplitude A, period T, and gain μ) and for all cases with $\Delta > 8$, the same pattern was found, with initial decay followed by uncontrolled growth. Meanwhile negative values of Δ resulted in reduced attenuation.

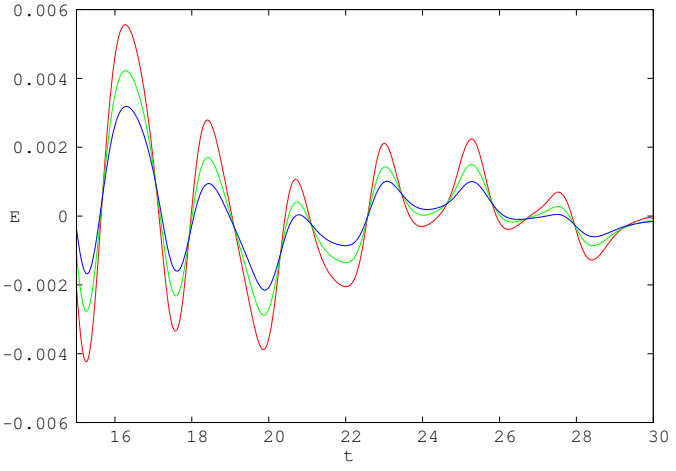

Figure 4.4: Controller (4.4) showing Error E^k with $\mu = 25$ and $\Delta = 0$ (red), $\Delta = 4$ (green) and $\Delta = 8$ (blue)

A comparison of the error E^k for the different controllers is illustrated in Figure 4.5, showing the superior performance of the ILC control. In the following, $\mu = 25$ and $\Delta = 0$ will be used for the ILC control as it provides good attenuation of the error but with an allowance for nonlinear effects.

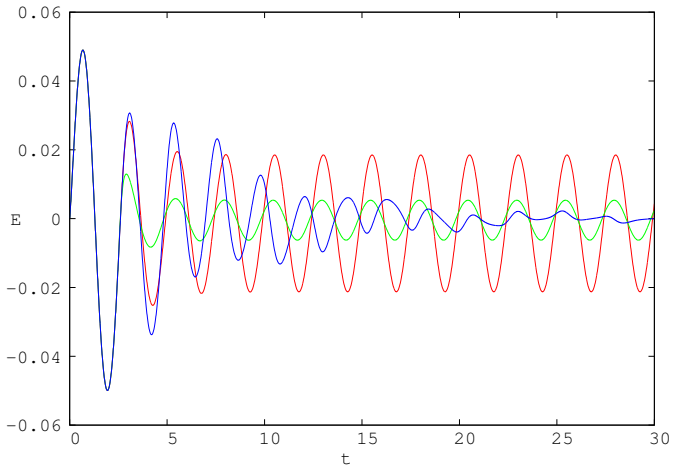

Figure 4.5: Controller (4.2) showing error E^k with $\mu = 50$ (red) and $\mu = 240$ (green). Controller (4.4) showing error E^k with $\mu = 25$ and $\Delta = 0$ (blue).

4.2 Vortical Flow (Non-Deterministic)

4.2.1 Flow Structure (Case Flow-12)

As developed in section 3, vortices will be introduced into the flow hence it is no longer periodic, although it still has a periodic component from the free stream. The response with the wake model is similar to the non-wake model. The main difference been the scales used as discussed in section 4.1.1 and the difference in the control schemes developed and their respective gains. Consider the flow with an oscillatory free stream with $A = 0.1$ and $T = 2.5$, and with two vortices introduced into the flow upstream of the airfoil, one with strength $\Gamma_1 = \frac{1}{10}$ placed at $\mathbf{x}_{v1} = (-30, 0.25)$ and the other also with strength $\Gamma_2 = \frac{1}{10}$ but at $\mathbf{x}_{v2} = (-20, -0.35)$ at the start of the simulation ($t = 0$). As mentioned previously, the period is x10 larger than the non-wake case to ensure the full effects of the wake model can be considered. With these starting values, vortex 1 will pass above the airfoil and vortex 2 below it, generating a significant disturbance in the lift in addition to that from the oscillation in the free stream velocity. Figure 4.6 shows the error for this flow with no control for the time that the vortices are passing the airfoil (approximately $t = 20$ and $t = 30$). In addition to the oscillation in lift arising from the freestream, large disturbances are generated by the vortices.

The ILC controller (4.4) with $\Delta = 0$ and $\mu = 25$ and a target value of the lift for undisturbed flow ($L_r = 0.379$) was applied to this flow. This suppressed most of the effect of the oscillation in the free stream, but not the disturbance due to the vortices. In fact, values of $\mu < 25$ gave better levels of attenuation when vortices are present, as can be seen in figure 4.7. Values of $\mu > 25$ led to unstable control schemes, therefore a value of $\mu = 15$ will be used in all forthcoming simulations.

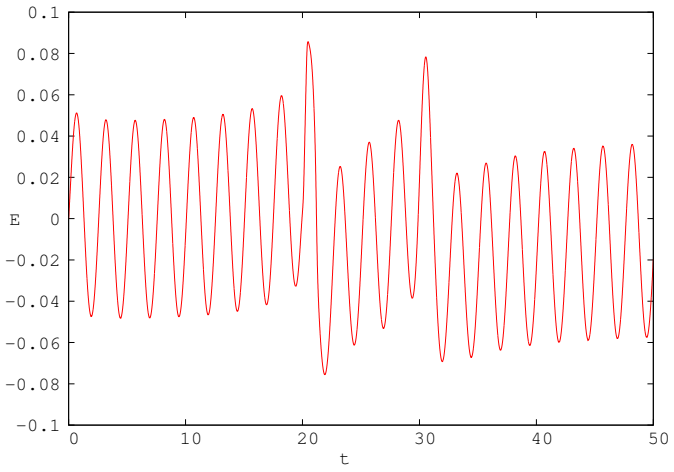

Figure 4.6: Error E^k for oscillatory flow past the airfoil with two vortices with no control (case 8)

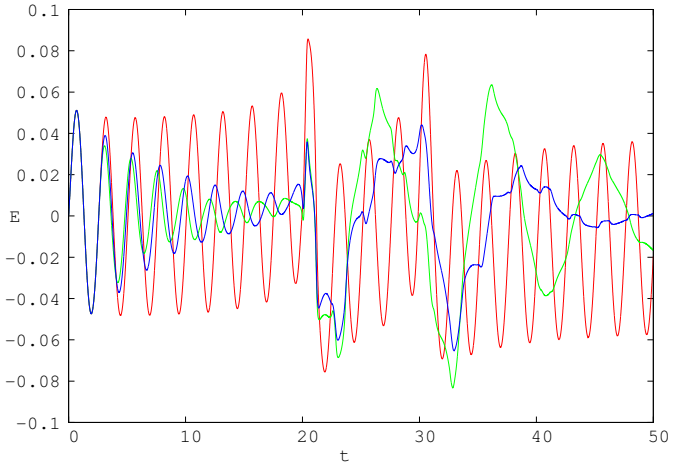

Figure 4.7: No control error E^k for case 7 (red). Error E^k for controller (4.4) with $\Delta = 0$, $\mu = 25$ (green) and $\mu = 15$ applied to case 8 (red)

4.2.2 Two-term ILC

The controller (4.2) reduced the magnitude of the fluctuations in the lift when applied to the oscillatory flow (Figures 4.1 and 4.2). When applied to the current case with two vortices, it damps much of the disturbance generated by the vortices but leaves a residual oscillation, as shown for $\mu = 240$ in Figure 4.8.

As in the non-wake case, this residual oscillation can be largely suppressed by applying a controller incorporating both proportional and phase-lead ILC, also referred to as two-term ILC. Specifically,

$$\hat{u}_j^{k_c} = u_{j-1}^{k_c} + \mu_0 E_{j-1}^{k_c+\Delta} \tag{4.5}$$

$$\bar{u}^k = \mu_1 E^{k-1} \tag{4.6}$$

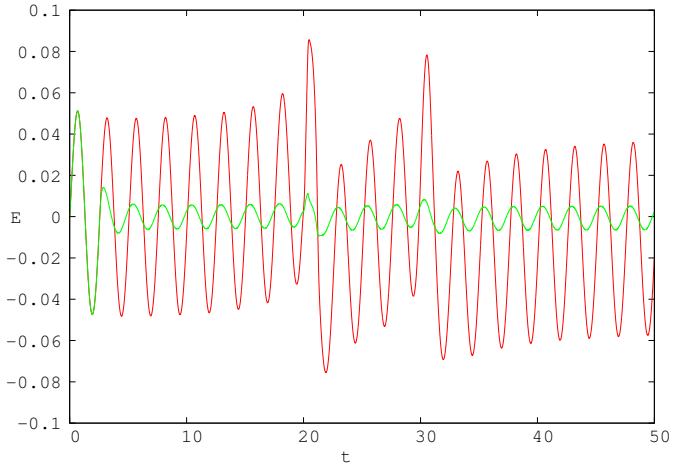

Figure 4.8: No control error E^k for case 1 (red). Error E^k for controller (4.2) with $\mu = 240$ applied to case 1 (green)

and

$$u_j^{k_c} = \hat{u}_j^{k_c} + \bar{u}^k \tag{4.7}$$

$k = jN_c + k_c$ as discussed previously in section 4.1.3. The two-term ILC algorithm is a function of both the control input and error from the same point in the previous cycle and just the error in the previous time step. The error for this controller with $\mu_0 = 15$, $\Delta = 0$ and $\mu_1 = 240$ is shown to be unstable. Reducing the value of μ_1 improves the stability with a value of $\mu_1 = 90$ producing optimum attenuation, as shown in Figure 4.9. The oscillatory component of the fluctuation has been almost completely eliminated, while the disturbance from the vortices has been heavily damped. The control input u^k, shown in Figure 4.10, closely tracks the lift for the uncontrolled flow, generating a counterbalancing force to the inherent fluctuation in the lift.

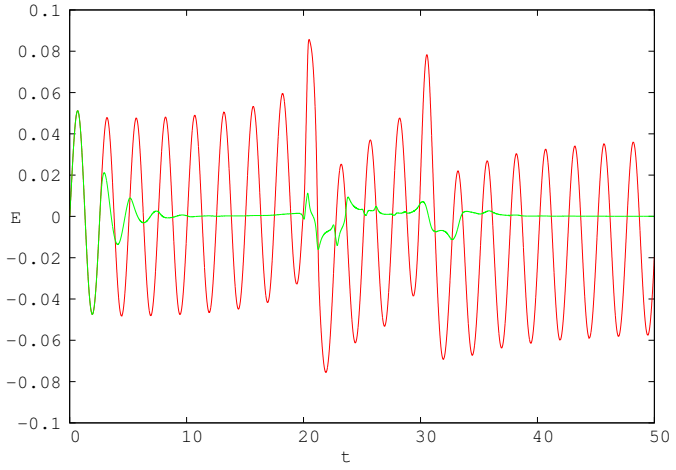

Figure 4.9: No control error E^k for case 1 (red). Error E^k for controller (4.5)-(4.7) with $\mu_0 = 15$, $\Delta = 0$ and $\mu_1 = 90$ applied to case 1

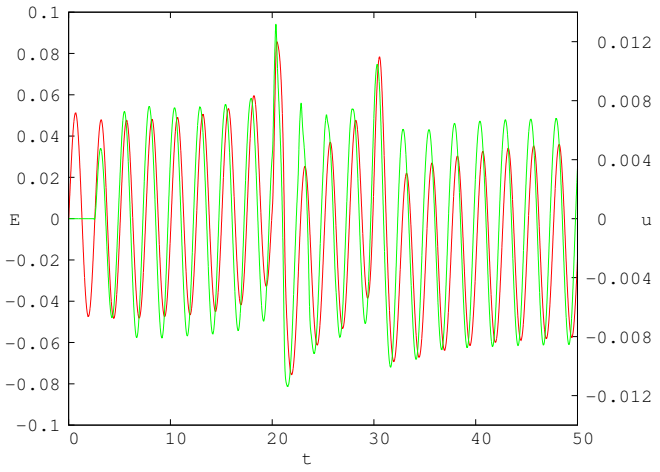

Figure 4.10: No control error E^k for case 1 (red). Control input u^k for controller (4.5)-(4.7) with $\mu_0 = 15$, $\Delta = 0$ and $\mu_1 = 90$ applied to case 1.

Increasing the values of the gains above these values did not significantly affect the performance of the controller and taking $\Delta \neq 0$ did not give significantly improved attenuation but remained stable for $\Delta < 8$, as for the case of pure oscillatory flow.

4.3 Composition Flow (Harmonic and Non-Harmonic)

Results so far have assumed a single fundamental frequency in the freestream velocity fluctuation. Real data from an actual turbine will not contain a perfectly sinusoidal fluctuation in the freestream velocity as previously assumed. Realistic inflow conditions will contain a range of other frequencies of velocity disturbance and signal noise. When implementing a smart rotor system, it would be possible to add low pass filters to enable the ILC algorithm to ignore the higher frequency disturbances but this section investigates ILCs ability to attenuate disturbances with a combination of both harmonic and non-harmonic composite fluctuations in the freestream velocity before proceeding to the more realistic case when using real turbine data. Throughout this chapter harmonic implies composite frequencies that are harmonics of the fundamental frequency. Unless otherwise stated the fundamental frequency is taken as the frequency used to represent the turbine frequency. Flow structures that are described as harmonic therefore contain frequencies that repeat exactly within a single cycle of the representative turbine period. The composite frequencies are locked to the cycle of the representative turbine frequency. Flow structures that are described as non-harmonic contain higher frequencies than the baseline fundamental frequency that do not repeat an integer multiple of times within the base turbine cycle.

4.3.1 Flow Structure (Harmonic) (Case Flow-14A)

Theoretically, harmonic disturbance configurations should attenuate more effectively than non-harmonics with ILC as harmonic disturbance will lead to more predictive fluctuations in the lift and the nature of ILC is to take advantage of disturbances that are deterministic. Figure 4.11 shows two harmonic inflows, one with a fundamental harmonic of 0.4Hz (the baseline period of T=2.5) and second and fourth harmonics of 0.8Hz and 1.6Hz respectively. The second, Figure 4.11(b), shows an inflow with a fundamental harmonic of 0.033Hz and a twelfth harmonic of 0.4Hz (the baseline period of T=2.5). These two flow structures are representative of conditions that might be expected on an actual turbine. Figure4.11(a) representing local gusts and Figure 4.11(b) representing slower moving shifts in the freestream velocity.

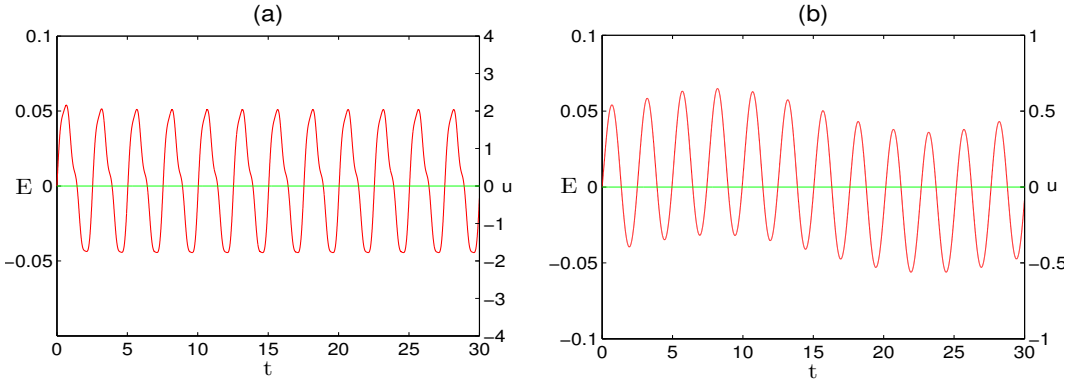

Figure 4.11: Error (red) for a composite inflow with harmonic frequencies of (a) f = 0.4Hz, 0.8Hz and 1.6Hz with A = 0.1, 0.02, 0.01 respectively and (b) f = 0.4Hz and 0.033Hz with A = 0.1 and 0.02 respectively

4.3.2 Two-Term ILC (Harmonic Flow)

Taking advantage of the fast computation of the non-wake flow model developed in section 3, the ability of the ILC algorithm to attenuate harmonic composition flows can be analysed efficiently. The reference periods in the ILC algorithm for both harmonic flows is the baseline reference period. In the non-wake model in section 3 this is T=0.25 (4Hz). The reference period in the ILC algorithm is matched to the fundamental frequency that represents the period of rotation for the turbine. When the frequency used in the ILC algorithm matches the fundamental frequency, as in 4.12(a), the ILC attenuates well with both norm ratios less than 0.1%. There are some oscillations within the first 2t but the ILC responds by reducing the error to almost 0.

The baseline two-term ILC is less capable of attenuating the disturbance when the frequency in the ILC algorithm doesnt match the fundamental frequency but instead matches a higher order harmonic, as in Figure (3.8(b)). This is a reasonable expectation because of the harmonic nature of the inflow, the ILC algorithm can increasingly perfect

the latest control input using predictable data captured from cycle error and controller values. The case where the ILC frequency doesnt match the fundamental flow frequency, as shown in 4.12(b), shows some attenuation but a significant amount of fluctuation is still present. It is clear that the effect of the 4Hz harmonic component is still present. This is understandable because the ILC algorithm matches the fundamental disturbance frequency (0.1Hz) so the calculation will effectively jump over approximately 40 of the smaller period harmonics in obtaining values for the present controller input. Improved attenuation is achieved when matching the ILC frequency to the 4th harmonic (4Hz) of the flow that represents the turbine period of rotation, as shown in Figure 4.13.

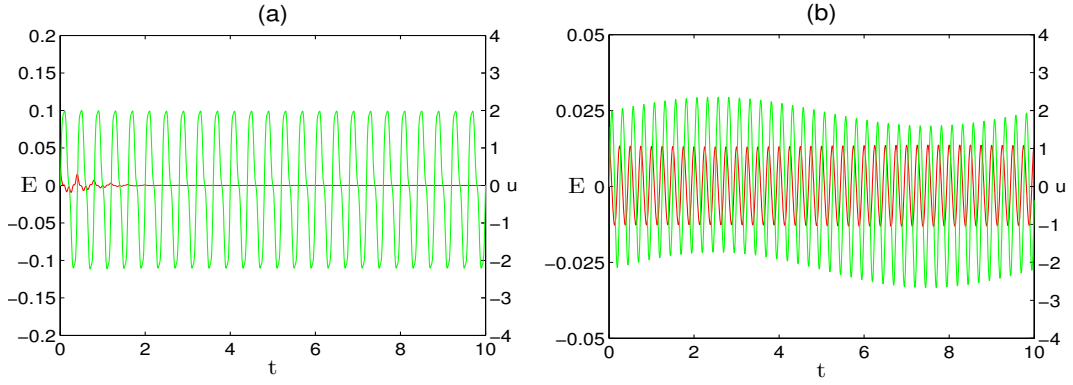

Figure 4.12: Error (red) and control (green) for Two-term ILC, with gains $\mu_0 = 10, \Delta = 0, \mu_1 = 20$, applied to harmonic inflow fluctuations shown in (3.8) for (a) fundamental frequency = 4Hz (b) Fundamental frequency = 0.1Hz

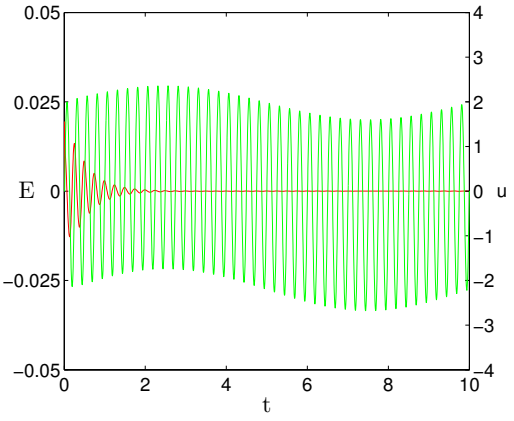

Figure 4.13: Two-term ILC, with gains $\mu_0 = 10$, $\Delta = 0$, $\mu_1 = 20$, applied to the disturbance with a fundamental frequency of 0.1Hz with ILC reference frequency of 4Hz

The performance metric ratios for this case are 0.045% (L_2) and 0.056% (L_∞). It is logical that the error is significantly reduced when compared to the control applied in Figure 4.12(b), where the control references the fundamental frequency of 0.1Hz, because the algorithm now captures the fluctuations generated by the 4th harmonic and ensures the fundamental harmonic is attenuated by sensing the larger period drift in the phase-lead and Integral-type aspects of the two-term ILC.

Applying the same principle to the harmonic flows with the wake model and using the benchmark two-term ILC developed in previous sections, (equations 4.9 to 4.11), with gains $\mu_0 = 15, \Delta = 0, \mu_1 = 90$ and target lift $L_\tau = 0.379$, is shown in 4.14. The reference frequency in the ILC algorithm for both cases is the fundamental flow frequency (0.4Hz) and results indicate significant attenuation when using the baseline flow frequency that represents the turbine period of rotation.

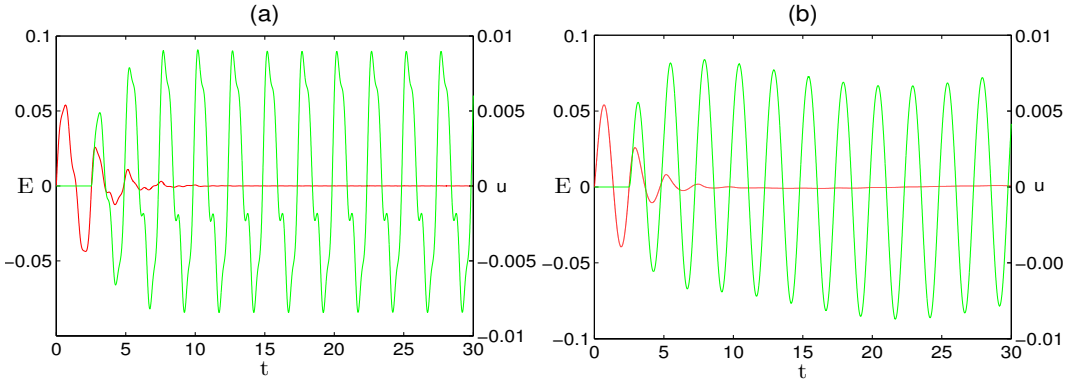

Figure 4.14: Error (red) and control (green) for Two-term ILC, with gains $\mu_0 = 15, \Delta = 0, \mu_1 = 90$, applied to harmonic inflow fluctuations shown in Figure 4.11 for (a) fundamental frequency = 0.4Hz (b) fundamental frequency = 0.033Hz

4.3.3 Flow Structure (Non-Harmonic) (Case Flow-14B)

Simple harmonic compositions are unlikely to occur on a real turbine and are more suitable for theoretical analysis. Real turbine data is more likely to compose of non-harmonic frequencies that will enter the system from a range of sources and result in relative aperiodic signals. These sources could be either external, from the flowfield (e.g. wind gusts), or internal, from the blade position itself (e.g. generator friction, blade instabilities). Either source results in a range of different frequency disturbances in the aerodynamic lift at a specific blade position. This section determines ILCs ability to attenuate disturbances that are a composition of non-harmonic frequencies and therefore aperiodic in nature within the relative timeframe of the representative turbine frequency. Figure 4.15 shows the uncontrolled inflow disturbances for non-harmonic compositions with approximate fundamental frequencies of 0.4Hz (a) and 0.035Hz (b). The term approximate fundamental frequencies is used because the flows are non-harmonic and strictly speaking a fundamental frequency does not exist within the relative timeframe. A fundamental frequency will exist that contains harmonics of the composition frequencies chosen but at a much lower value than the frequency range used in this analysis. The composite frequencies of oscillation are arbitrary and the amplitudes remain the same as in the previous section.

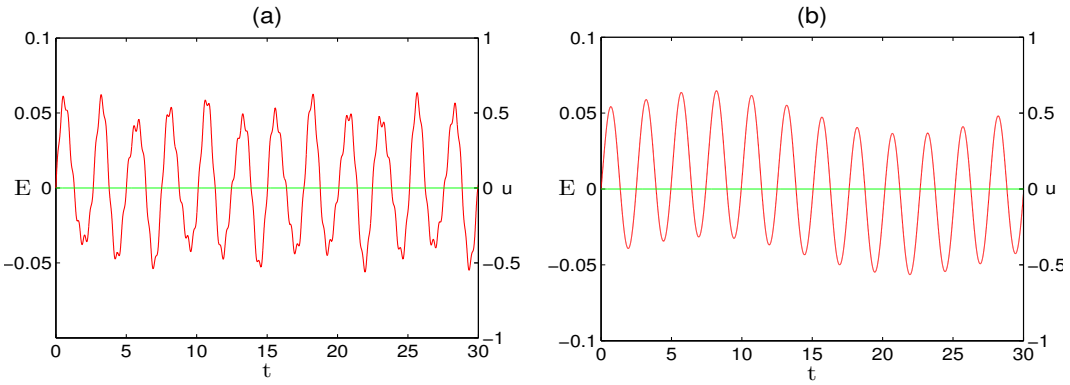

Figure 4.15: Error (red) for an inflow velocity fluctuation with three composite frequencies of (a) 0.4Hz, 0.675Hz and 2.584Hz with A = 0.1, 0.02, 0.01 respectively and (b) T = 0.4Hz and 0.035Hz with A = 0.1 and 0.02 respectively

The non-harmonic nature can be seen in the error plots in Figure 4.15 as the inflow appears to be non-deterministic. This will make it harder to achieve low performance metrics using the two-term ILC.

4.3.4 Two-Term ILC (Non-Harmonic Flow)

The benchmark two-term ILC developed in previous sections, (equations 4.9 to 4.11), with gains $\mu_0 = 15, \Delta = 0, \mu_1 = 90$ and target lift $L_\tau = 0.379$, was applied to both non-harmonic flow structures. 4.16 shows the control of both non-harmonic composite flow cases with this controller. The reference periods in the ILC algorithm for both flow conditions are 0.4Hz, i.e. fundamental flow frequency that represents the turbine period of rotation.

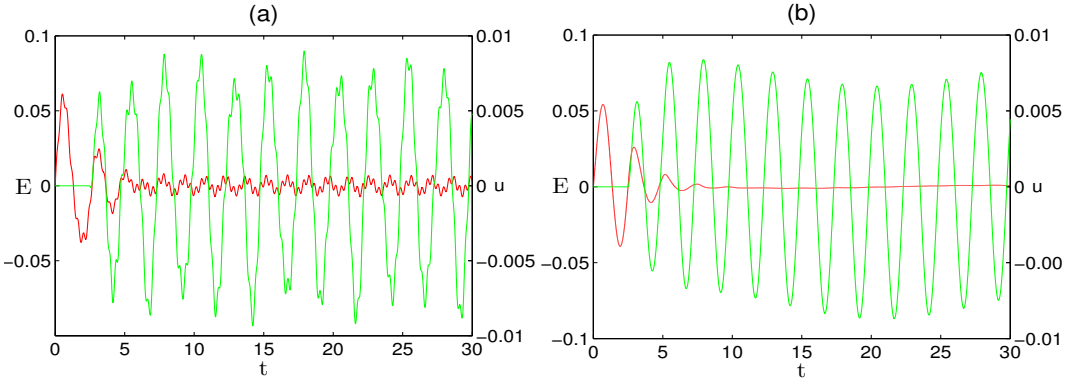

Figure 4.16: Two-term ILC, with gains $\mu_0 = 15$, $\delta = 0$, $\mu_1 = 90$, applied to non-harmonic composite inflow fluctuations shown in Figure 4.15 for (a) fundamental frequency 0.4Hz (b) fundamental frequency 0.035Hz

Figure 4.16(a) shows a residual oscillation in the lift error. The performance metric ratios are still reasonable, 12.6% (L_2) and 14.7% (L_∞), but further attenuation can

be achieved by tuning the two-term ILC gains. Figure 4.17 shows the response of the two-term ILC with gains $\mu_0 = 20$, $\Delta = 0$, and $\mu_1 = 110$.

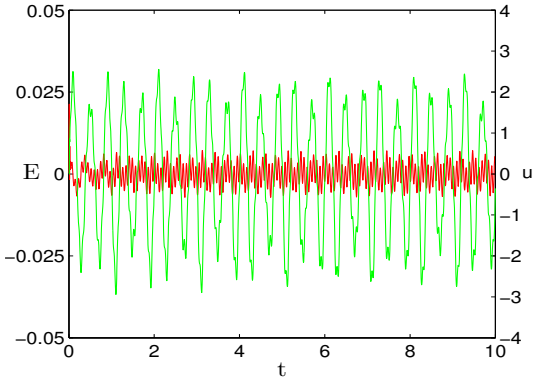

Figure 4.17: Two-term ILC, with gains $\mu_0 = 20$, $\Delta = 0$, $\mu_1 = 110$, applied to the non-harmonic composite inflow shown in 4.16

While a small level of lift disturbance still remains, the attenuation has improved with an increase in gains with performance metric ratios of 6.32% (L_2) and 7.46% (L_∞). A further increase in the gains leads to instabilities in the response and the error becoming uncontrollably large.

The non-harmonic disturbances controlled thus far in this section have contained periods of lift disturbance in the freestream velocity that are much smaller than would be expected on an actual turbine, while the amplitude remains reasonably representative. These smaller periods have been used during initial controller performance analysis because they offer high levels of computational efficiency and represent worse case scenarios. Figure 4.3.4 shows an uncontrolled case with larger non-harmonic periods with the same amplitudes and the system response when applying the standard two-term ILC to this more representative turbine case.

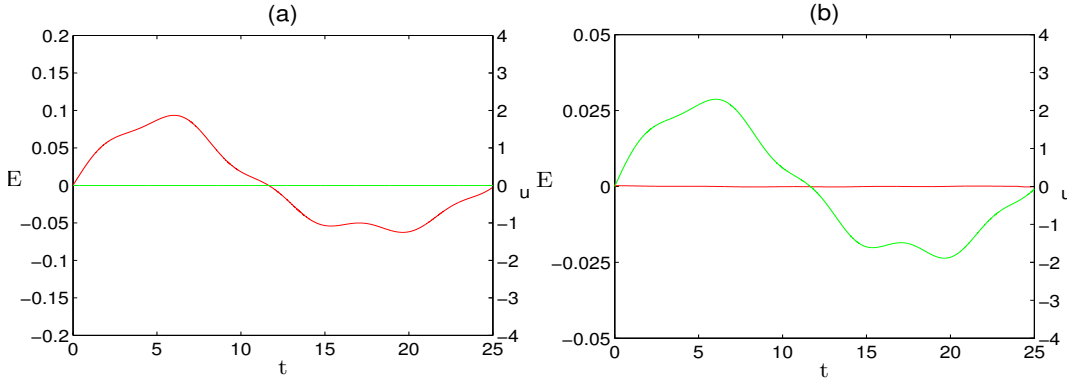

Figure 4.18: Uncontrolled error (red) and controlled error (green) for inflow disturbance in the freestream velocity with non-harmonics of T = 24, 14,23 and 5.33 and amplitudes of A = 0.1, 0.02 and 0.01. Two-term ILC with gains $\mu_0 = 15$, $\Delta = 0$, $\mu_1 = 90$

The performance metrics are reduced to almost zero and the fluctuations are almost fully attenuated. Reducing the non-harmonic periods further towards the previous response seen in Figure 4.17 is shown in Figure 4.19. Again, there is almost full attenuation of the inflow disturbance.

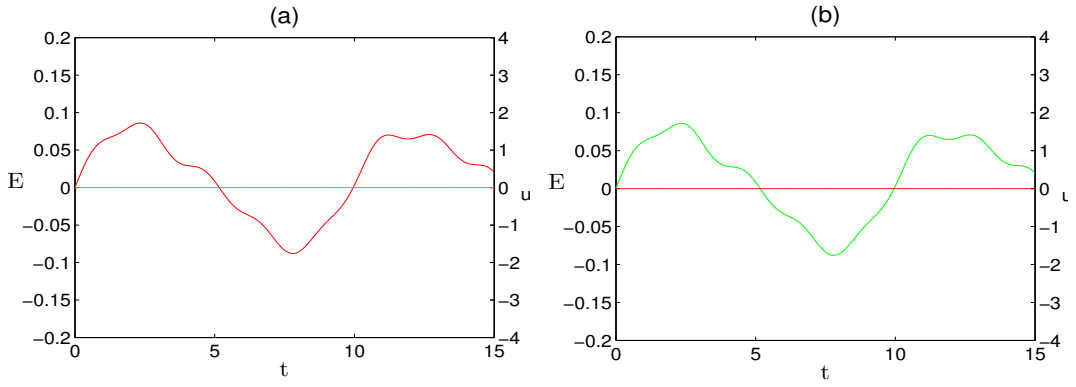

Figure 4.19: Uncontrolled error (red) and controlled error (green) for inflow disturbance in the freestream velocity with non-harmonics of T = 10, 4.75 and 2.07 and amplitudes of A = 0.1, 0.02 and 0.01. Two-term ILC with gains $\mu_0 = 15$, $\delta = 0$, $\mu_1 = 90$

It is evident that reducing the periods of the non-harmonic oscillations reduces the ability of the ILC to attenuate the lift disturbances. This is logical because reducing the periods means the ratio between the period and amplitude increases, so when the ILC takes the values from the previous cycle, they are more likely to be further away from the position that would provide the ideal control input. In reality a turbine inflow disturbance is more likely to show behaviour similar to Figure 4.3.4 and Figure 4.19 but with the addition of smaller scale noise. As discussed previously, these noise sources could be both internal and external to the system.

Figures 4.3.4(a) and (b) show the baseline non-harmonic inflow disturbance in 4.19 with the addition of a random noise on the inflow signal every time step (dt = 0.005). This random noise is modelled as an addition to the mean freestream velocity, with the three non-harmonics, of a random number in the range of +/- 0.01.

The ILC algorithm attenuates the non-harmonic oscillations, as seen previously in Figure 4.19, but has little effect on the signal noise. The scale of the noise applied at every time step is unrealistic for an actual turbine (dt=0.005 equates to noise every 0.00008 seconds for a cross section near the tip at nominal operating conditions). This frequency of noise would not be captured by a sensing system. Applying noise at a reduced sampling rate is shown in Figure 4.3.4 at a frequency of every 10t.

This reduced frequency equates to a random offset on the freestream velocity every 0.17 seconds for a cross section near the tip at nominal operating conditions. The noise is still present so we can conclude the ILC algorithm does not attenuate this specific noise profile. This is expected when analysing the ILC algorithm because the random noise

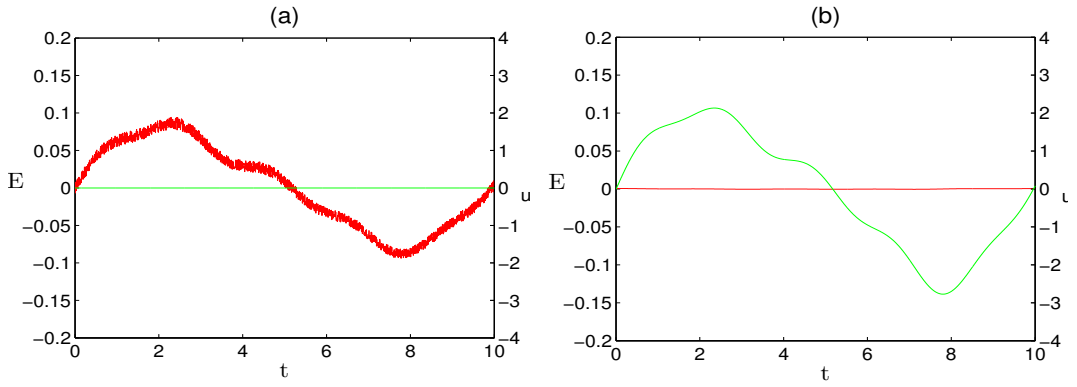

Figure 4.20: Uncontrolled error (red), controlled error (green) and control input (blue) for inflow disturbance in the freestream velocity with non-harmonics of T = 10, 4.75 and 2.07 and amplitudes of A = 0.1, 0.02 and 0.01 and an additional noise factor within the range +/- 0.01 every time step. Two-term ILC with gains $\mu_0 = 10$, $\Delta = 0$, $\mu_1 = 20$

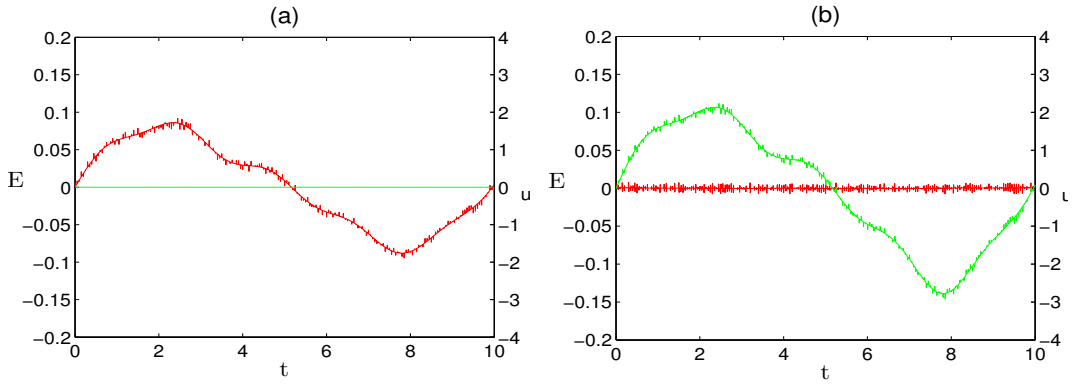

Figure 4.21: Uncontrolled error (red), controlled error (green) and control input (blue) for inflow disturbance in the freestream velocity with non-harmonics of T = 10, 4.75 and 2.07 and amplitudes of A = 0.1, 0.02 and 0.01 and an additional noise factor within the range +/- 0.01 every 10 time steps. Two-term ILC with gains $\mu_0 = 10$, $\Delta = 0$, $\mu_1 = 20$

offset is generated within the same time step that the control output is calculated. The critical understanding gained from this section is that the ILC algorithm does not appear to become unstable when noise is present in the inflow freestream velocity signal. For implementation purposes this noise can be removed by using a low pass filter.

4.3.5 Flow Structure (Real Turbine Input) (Case Flow-4C)

The freestream velocity profile in Figure 4.22 represents a typical inflow disturbance for a turbine at 40m span during nominal operation. The data varies in both period and amplitude and is based on actual turbine data, Thomsen et al.(2008). The data has been non-dimensionalised and scaled to align with the flow configurations used in previous sections.

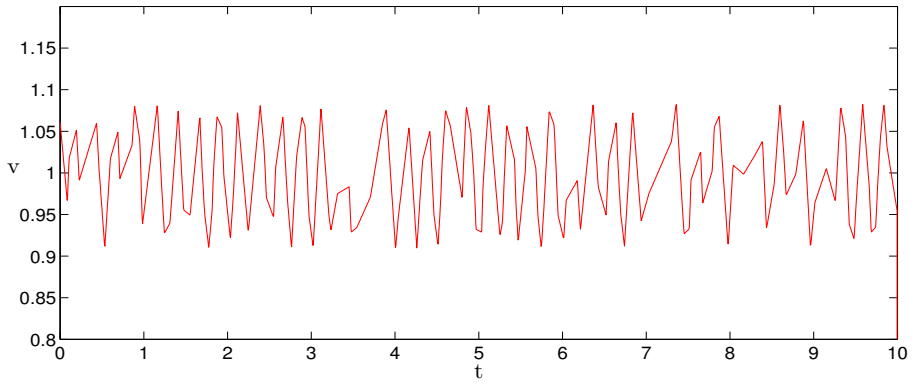

Figure 4.22: Non-dimensionalised freestream velocity disturbance based on real turbine data (Thomsen et al., 2008) with no control

4.3.6 Two-Term ILC (Real Turbine Input)

Figure 4.23 shows the response of the system using the baseline two-term ILC applied to this inflow condition using an averaged reference period in the controller of T=25.

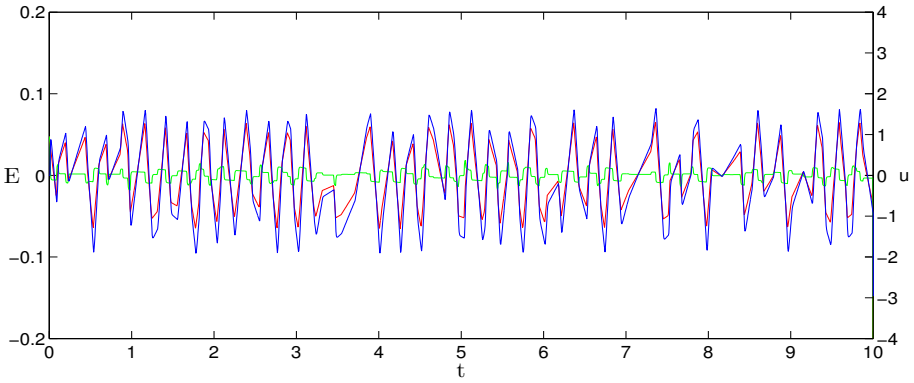

Figure 4.23: Error (green) and control input (blue) for non-dimensionalised (see section 2.2) freestream velocity disturbance based on real turbine data (Thomsen et al., 2008) with two-term ILC applied with gains $\mu_0 = 10$, $\Delta = 0$, $\mu_1 = 20$. Uncontrolled error shown in (red)

The controller attenuates the majority of the disturbances resulting in performance metrics below 10%.

4.4 Variable Period Flow (Non-Deterministic)

4.4.1 Flow Structure (Case Flow-13)

On a real turbine the period of the freestream velocity fluctuation T will vary around a target value. As discussed in Section 1.5, the target period of rotation is determined by the tangential tip speed required to maintain an optimum tip speed ratio for varying

wind speeds. The power coefficient of a given turbine is dependent on the tip speed ratio, with an approximate optimal value of $\omega R/v = 7$ for maximum power for large scale wind turbines, where ω is the rotor rotational speed in rads/sec, R is the rotor radius in metres and v is the axial wind speed in m/s. Changes in the axial wind speed will have a direct impact on the period of rotation. At higher wind speeds it becomes unrealistic to maintain a tip speed ratio of 7 as the centrifugal forces and noise levels become too large. Typical periods of rotation fall in the range of 3 to 7 seconds. This period is driven by the changing axial wind speed therefore the period will change over a reasonably large timescale.

For results so far with the wake flow model, the ILC controller has dealt with velocity fluctuations in the baseline flow of constant period. In turn the ILC algorithm has used the same constant period in the phase lead contribution in the two term ILC, j in equation (4.5). The following section analyses the robustness of the controller to a drifting value of T.

The variable period input signal used in the present section is shown in Figure 4.24 along with a scatter plot of the periods within the given time frame. The period drifts around a target period of $T = 2.5$ and an amplitude of approximately $A = 0.1$. The period variation is obtained from a pseudo-random number generator.

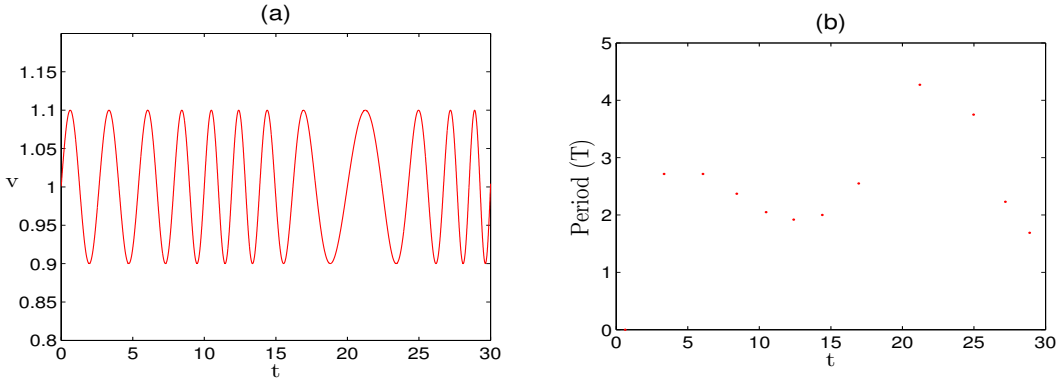

Figure 4.24: (a) Variable period velocity disturbance for a case with a large variation in the period at approximately t=20. (b) period distribution for inflow case (a)

4.4.2 Two-term ILC

The period variation introduced means a modification to the baseline two-term ILC is required. To account for the varying period, and effectively varying speed of rotation of the turbine, the time step used in both parts of the ILC algorithm are modified to become a function of the speed of rotation. This is implemented by obtaining the angle covered per time step across an average sinusoidal oscillation (in this case T = 2.5t) and dividing by the current angular velocity. This ensures that the control input to the flow

model will varying depending on the speed of rotation. A level of gain optimisation is also required to ensure maximum attenuation. For the flow case outlined in Figure 4.24 two-term ILC gains of $\mu_0 = 15$, $\Delta = 0$, and $\mu_1 = 120$ are used and the results shown in Figure 4.25.

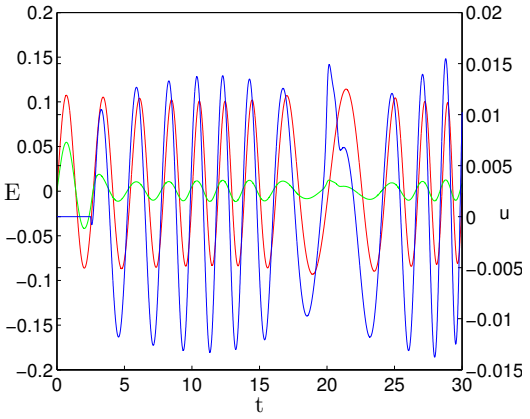

Figure 4.25: Two-term ILC ($\mu_0 = 15$, $\Delta = 0$, and $\mu_1 = 120$) applied to case flow-13 (large fluctuations in the freestream disturbance period). Uncontrolled (red), controlled (green) and control input (blue)

The performance metrics are low considering the significant fluctuation in the freestream period. The metrics are considerably lower, 5.2% (L_2) and 14.1% (L_∞), than would be expected without the modification to the time step.

The influence of a non-constant period can be seen in the perturbations that remain. Attempts were made to attenuate these peak errors in a number of ways but all methods employed generally had an insignificant effect or initiated instabilities within the controller. A method investigated was to make the gains variable as they approached the minimum and maximum error locations based on blade position. A combination of smaller and larger gains in these regions had little effect on the performance metrics with some instances causing large scale instabilities.

4.5 Lift Estimator

4.5.1 Lift and Pressure Correlation

As in the previous chapter, a Pearsons correlation factor r_{pL} is used to establish the correlation between the global lift and panel pressures across the aerofoil using equation 3.12.

Figure 4.26(a) shows the correlation for 3 flow cases with different vortex strengths and Figure 4.26(b) the same cases with two term ILC applied. Note that the steady state lift value and flow behaviour is different when the wake model is included which will

ultimately result in different array coefficients. As discussed in section 4.2, a steady state lift with the inclusion of the wake model has an approximate non-dimensional value of 0.370 at an angle of attack of 0°.

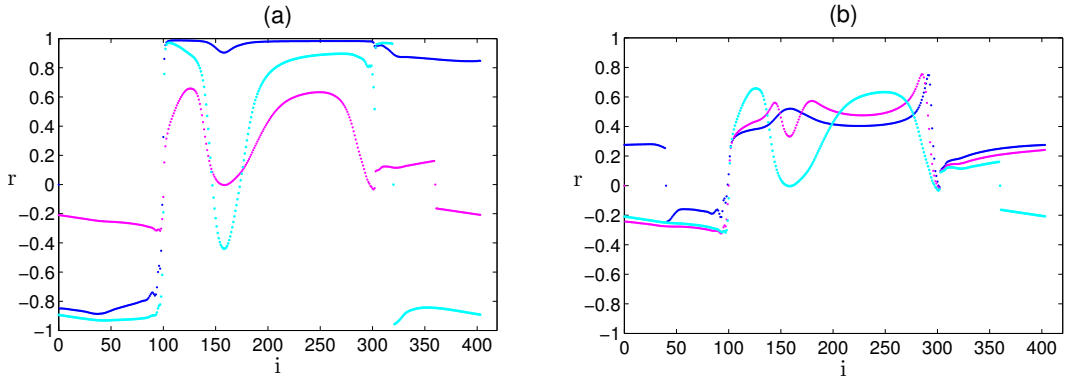

Figure 4.26: Correlation factors for three different strength vortices (a) with no control and (b) with control

Correlations have not been calculated for linear flow cases (i.e. freestream fluctuation and no vortices) because previous results in section 3.5.1 have shown linear flows result in perfect correlation. Correlations for variation in angle of attack and vortex strength show a similar behaviour as shown in Figure 4.26. In general, good correlation is achieved for pressure points around the middle to leading edge suction side. As previously discussed, correlation reduces as approaching the leading edge as the panels tend towards a more vertical position. The leading edge pressure side of the aerofoil indicates poor correlation for all flow configurations (around panel i=150). Correlation is very good for the remaining areas on the pressure side and correlation drops again as approaching the trailing edge. Correlation for the suction side middle to trailing edge is reasonable. Figure 4.5.1 visualises these pressure sensor array conclusions. The array is similar to that found in section 3 with the significant difference of removing the pressure sensor found on the pressure side mid-leading edge (i.e. the poorly correlated panel at i=150). The number of averaged pressure differences used to calculate the lift estimate is now 30 (5 pressure side and 6 suction side sensors).

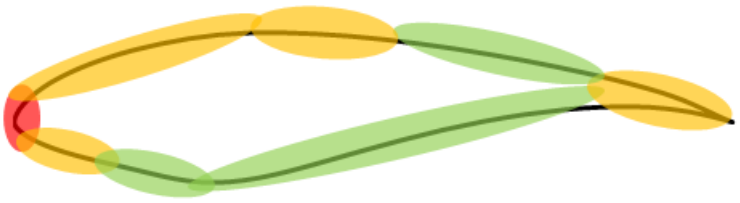

Figure 4.27: Optimal pressure sensor array designed for lift estimation as an input to the ILC algorithm

As concluded in the lift estimation work in section 3, it is critical to place an even spread of pressure sensors across both upper and lower surfaces to ensure the effect of vortices passing the aerofoil are adequately captured.

4.5.2 Pressure Sensor Arrays

As in section 3.5.2, pressure coefficients are calculated for each pressure difference between upper and lower panel pressures shown in Figure 4.5.1, for a steady flow with no disturbances or control. These coefficients vary from the non-wake model case and are shown in table 4.1.

		Pressure Panel Number				
		107	129	195	242	272
Suction Panel Number	95	1.130	2.053	1.647	1.004	0.907
	73	0.654	0.885	0.800	0.610	0.573
	45	0.586	0.765	0.700	0.550	0.520
	7	0.723	1.015	0.904	0.669	0.625
	364	0.942	1.508	1.277	0.853	0.782
	334	1.074	1.876	1.531	0.959	0.871

Table 4.1: Coefficients for 11 sensor array

The lift is then estimated from these pressure coefficients and pressure differences as previously defined in equation 3.13.

4.5.3 Validation

In order to validate the accuracy of the lift estimator developed for the wake flow model, the estimated lift is compared to the direct lift for a range of flow cases with initially no control, as shown in Figure 4.28. These figures indicate that the estimator developed adequately estimates the lift for a ramped lift and a freestream periodic fluctuation. These flow cases are relatively simple and do not include the significant stochastic effect of a passing vortex. Figure 4.29 shows the estimated lift against the direct lift for two flows with vortices. The estimate is slightly offset from the direct lift but not substantially and the sensor arrays provides an adequate estimate that can be investigated with the ILC algorithm and wake flow model.

Figure 4.30 shows the lift estimate when applying two term ILC to a flow with no disturbance and a flow with a periodic freestream fluctuation and two vortices. The simple case showing the effect of the wake model (i.e. the Wagner effect) shows near perfect lift estimation (4.30(a)) but when flow disturbances are introduced a fluctuation remains in the lift estimate (4.30(b)).

Figure 4.31 shows a simple periodic disturbance in the freestream with ILC application and a comparison of the estimated and direct lift. There is clearly a phase difference between the control input and the estimated lift. Closer analysis of Figure 4.31 indicates the lift estimate lags behind the control input by approximately 450 times steps (1 time

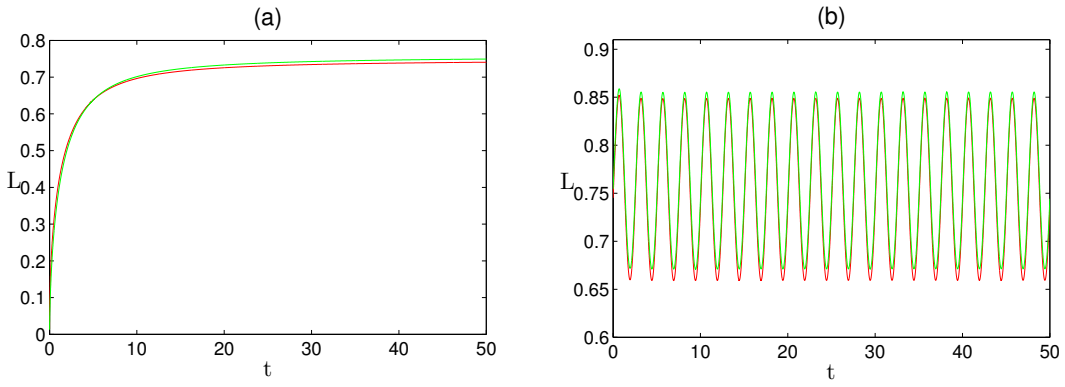

Figure 4.28: Direct lift (red) and 11 sensor estimated lift (green) for a flow with no control - (a) initialisation to show the Wagner effect of the wake model. (b) periodic fluctuation in the freestream velocity

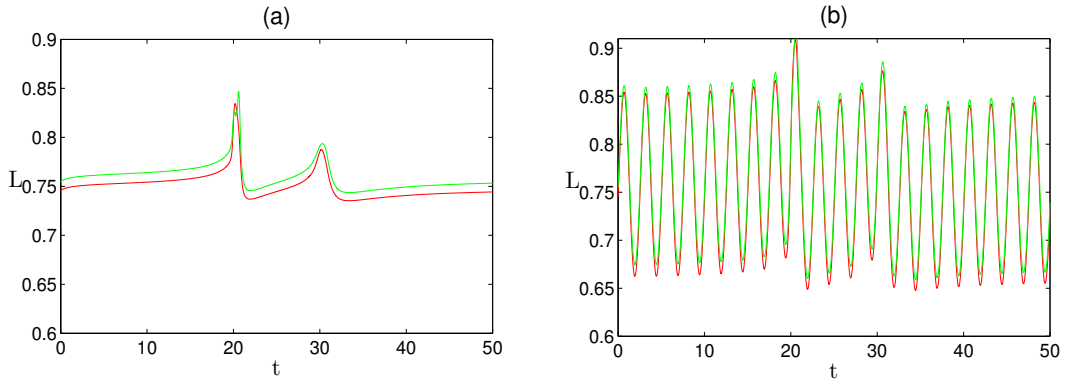

Figure 4.29: Direct lift (red) and 11 sensor estimated lift (green) for a flow with no control - (a) two upstream vortices (b) periodic fluctuation in the freestream velocity and two upstream vortices

step = 0.005t). This is approximately the time constant of the lift to reach its target value when accounting for the Wagner effect in the wake model.

The proposed solution is to account for the wake effect by subtracting a weighted and delayed function of the control input from the lagged lift estimate as shown in (4.10),

$$L_e = L_{e0} - Cu^{k-d} \tag{4.8}$$

Where C = coefficient and d = delay factor to account for the Wagner effect. A range of C and d values were tested for flows with periodic disturbances, vortical flows and a combination of both. The optimum results were values of $C = 0.9$ and $d = 450$. Applying these values to the lift estimate in equation (4.10) results in significantly reduced oscillations in the lift estimate as shown in Figure 4.32.

The delay factor used in Figure 4.32 of $d = 450$ corresponds to the Wagner effect time constant, i.e. the time for a trailing edge vortex to travel 6 or 7 chord lengths. This

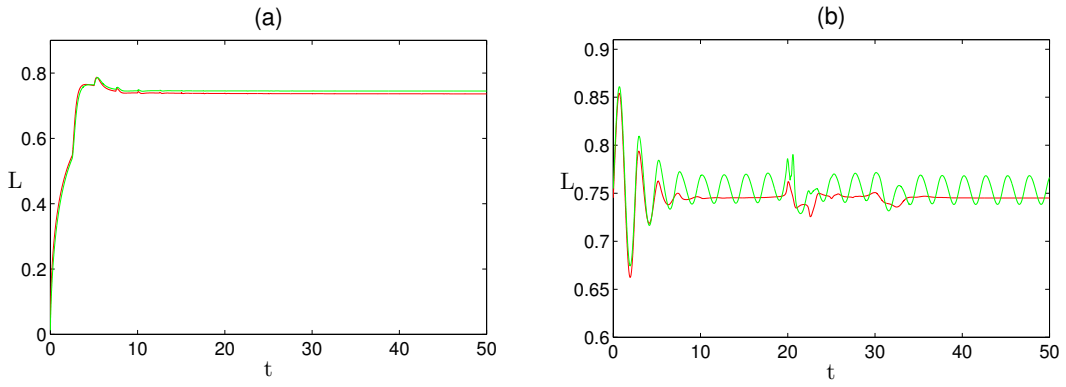

Figure 4.30: Direct lift (red) and 11 sensor estimated lift (green) for a flow with two-term ILC (a) initialisation to show the Wagner effect of the wake model (b) periodic fluctuation in the freestream velocity and two vortices

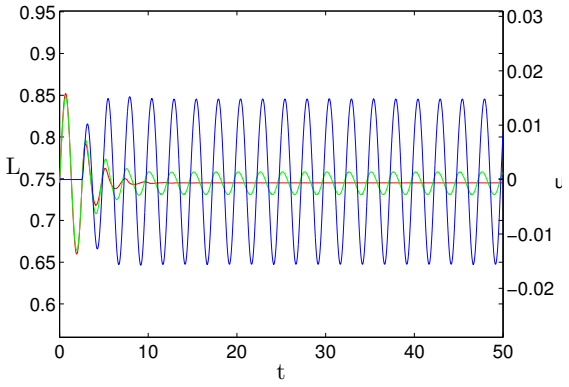

Figure 4.31: Periodic disturbance with baseline two-term ILC using direct lift input (red), 11 sensor estimated lift (green) and control input for 11 sensor estimator (blue)

estimator correction produces reasonable lift estimates for a range flow configurations and will be used to investigate application as an input to two term ILC in the next section.

4.5.4 Two-term ILC (Case Flow-12)

The lift estimation used in Figure 4.32 is now used as the controller feedback for Case Flow-12 (periodic disturbance and two vortices) with the wake flow model and results shown in Figure 4.5.4.

It is evident that the controller becomes unstable at approximately t=35. Attempts were made to tune the controller gains to remove the instabilities but stable, adequate attenuation was not possible. Further examination of the estimation modification in equation (4.10) indicates that the estimation at a particular time step could contain an error that could amplify when considering only a single point when subtracting the

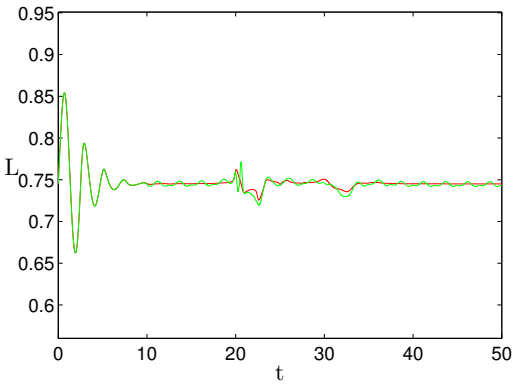

Figure 4.32: Direct lift (red) and modified 11 sensor estimated lift (green) from equation (4.10) using $C = 0.9$ and $d = 450$ for flow conditions and controller from Figure 4.30

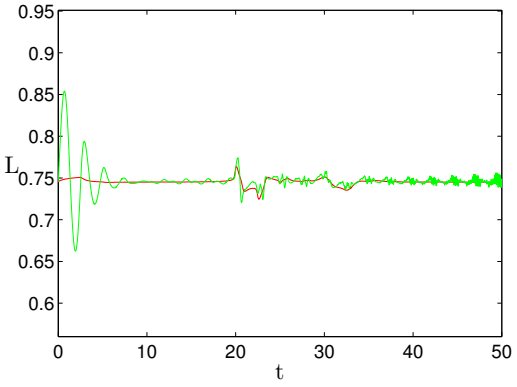

Figure 4.33: Resultant lift when applying two-term ILC ($\mu_0 = 15$, $\Delta = 0$, and $\mu_1 = 90$) to Case Flow-12 (oscillating freestream and two upstream vortices) with (a) direct lift (red) and (b) estimated lift from Figure 4.32 (green) in the feedback loop for the ILC algorithm

weighted controller term. The instability observed in Figure is driven by this poor spatial sampling. A sample size of one inherently leads to poor state estimation and consequently equation (4.10) is now modified to consider multiple previous controller inputs in the lift estimation calculation,

$$L_e = L_{e0} - C\left\{\frac{\sum[(u^{k-d_1}) + (u^{k-d_2}) + ...(u^{k-d_n})]}{n}\right\} \tag{4.9}$$

Where d_n = positon of the nth reference point and n = total number of reference points. A number of averaged controller input reference point configurations were tested with Case Flow-12 with the most optimum configuration consistent of 11 references at $d_1 = 400$, $d_2 = 410$, $d_3 = 420$, $d_4 = 430$, $d_5 = 440$, $d_6 = 450$, $d_7 = 460$, $d_8 = 470$, $d_9 = 480$, $d_10 = 490$ and $d_11 = 500$. This ensures that controller inputs either side of the wagner time constant of t=450 are considered and allows for fluctuations in the

wake time constant. The results using this modified lift estimator are shown in Figure 4.34.

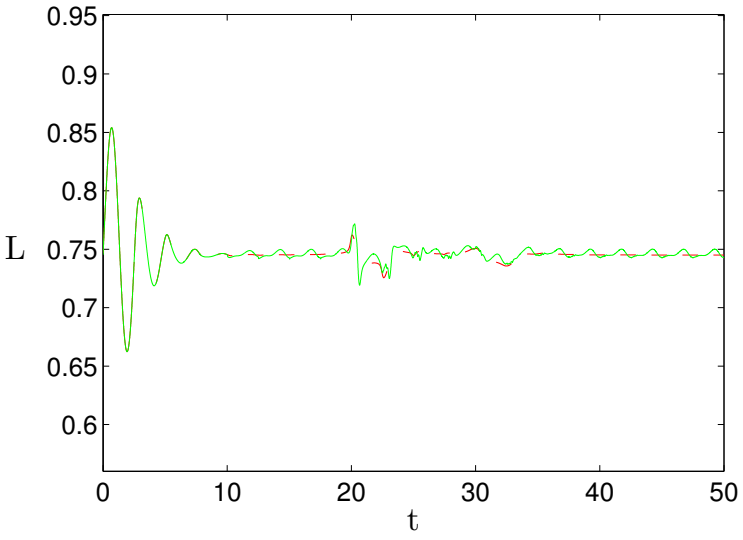

Figure 4.34: Resultant lift when applying two-term ILC ($\mu_0 = 15$, $\Delta = 0$, and $\mu_1 = 90$) to Case Flow-12 (oscillating freestream and two upstream vortices) with (a) direct lift (red) and (b) estimated lift from equation 4.9 with 11 averaged control input values (green) in the feedback loop for the ILC algorithm

4.6 Actuator Dynamics

4.6.1 First-Order Lag

Work in the previous sections has assumed an instantaneous response from the modelled actuator. This is not realistic behaviour for a physical smart rotor system and in reality there will be a lag between the controller calculating the control input and the actuator producing the circulation change required. This is where implementation and the feasibility of the system in terms of realistic actuation mechanisms is assessed. If the actuation is too slow then the circulation change will not act quickly enough and the disturbance will pass over the aerofoil uncontrolled with a control effect passing into the system too late. This will potentially cause instabilities in the system and have a detrimental effect on the performance metrics. Modelling the lag on the actuation with a first-order lag with no wake effects gives the advantage of introducing nonlinear effects in a computationally efficient manner. To model this system lag a first-order lag will be used to model the actuator dynamics. Specifically,

$$u = \hat{u}(1 - e^{-\lambda t}) \tag{4.10}$$

where u is the actual control input due to the lag, $\hat{u}$ is the target control input, λ is the reciprocal of the time constant and determines the speed of the response. With a constant input $\hat{u}$, the system exhibits a standard first order lag with exponential behaviour in u. A measure of the actuator response is given by the time it takes u to reach 90% of $\hat{u}$ when $\hat{u}$ is constant. In non-dimensional terms, this is $2.3/\lambda$. Increasing the value of λ will result in a quicker actuator response. The differential of u will be used to implement the lag,

$$\begin{aligned} \frac{du}{dt} &= \hat{u}\lambda e^{-\lambda t} \\ &= \lambda(\hat{u} - u) \\ &= \lambda\hat{u} - \lambda u \end{aligned} \tag{4.11}$$

Therefore

$$\frac{u^k - u^{k-1}}{\Delta t} = -\frac{\lambda}{2}(u^k + u^{k-1}) + \lambda\hat{u}$$

Hence

$$u^k = \frac{u^{k-1}(1 - \lambda\frac{\Delta t}{2}) + \lambda\hat{u}\Delta t}{(1 + \lambda\frac{\Delta t}{2})} \tag{4.12}$$

Introducing a lag on the controller input models the effect of the actuator dynamics. If we assume the smart rotor system uses a traditional trailing edge flap actuation system, the lag is driven by physical characteristics such as the inertia of the actuator and the time taken for the motor, that moves the actuator, to get up to speed. The actuator responds immediately but has a phase lag that means the actual position lags the commanded position. This is the first order lag modelled above.

Two other types of physical limits are present on a physical smart rotor actuator that are not modelled in this thesis. They can be described as system bounds, limits or clipping and will be discussed here in terms of a trailing edge flap actuation system. Firstly, there is a limit on the maximum angle achievable. The output is effectively clipped in line with the maximum control surface deflection angle. This is typically in the range of +/- 20 degrees. The system reaches a physical limit, the commanded circulation change to counteract the disturbances cannot be met and the system becomes non-linear in its response. The second system limit is the rate of change of circulation. For a trailing edge flap this represents a limit on the rate of change of the flap angle. This is typically driven by the maximum motor/pump speed that drives the actuator.

These two limits break the linearity of the system if the demanded angle and/or rate of change of angle meet or exceed the limits. If the demand falls within the two limits then the linear dynamics of the system is free to respond without any constraints on achievable circulation. This is the assumption made in this thesis. It is assumed that the increase in circulation and rate of change of circulation are unbounded. In the example of a trailing edge flap, the maximum deflection angle and the rate of change of angle is unbounded. If these two limits were considered and implemented into the model, it is possible that the performance metric values would increase. Further investigation of specific actuator systems would be required to implement this analysis.

4.6.2 Two-term ILC with Actuator Dynamics Applied to Case Flow-12

Figure 4.35 illustrates the response of the actuation to a step input of $u = 0.01$ at time $t = 2.5$, for a flow with no disturbances or upstream vortices, for values of $\lambda = 1, 10$ and 100.

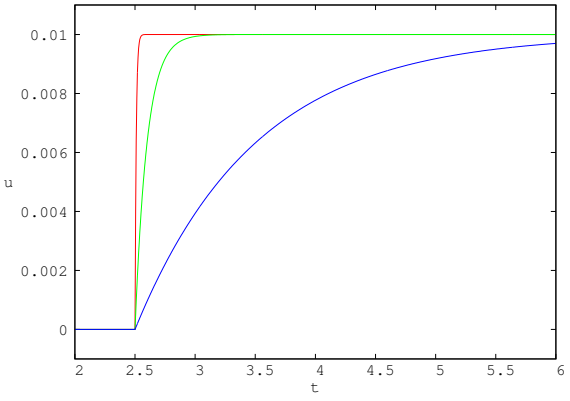

Figure 4.35: Control response for a step input of $u = 0.01$ with $\lambda = 100$ (red), 10 (green) and 1 (blue).

For values of $\lambda > 1000$ the response becomes underdamped and the response becomes unstable as shown in Figure 4.36 for a simple oscillating freestream inflow condition. This is because the actuator response becomes underdamped and overshoots, as shown in Figure 4.37.

The limiting upper value of λ for which the response starts to become unstable is the same across all cases but increasing the period of the freestream fluctuation means the controller is able to remain stable for these higher values of λ. For implementation purposes, a filter could be used to attenuate these initial overshoots and produce a response that tends towards a first order response.

To avoid unnecessary fluctuations in the initial response and potential instabilities, values of $\lambda < 1000$ will be used. Calculating the time taken to reach 90% of the demanded control gives an indication of how quick the actuator response is. Values of

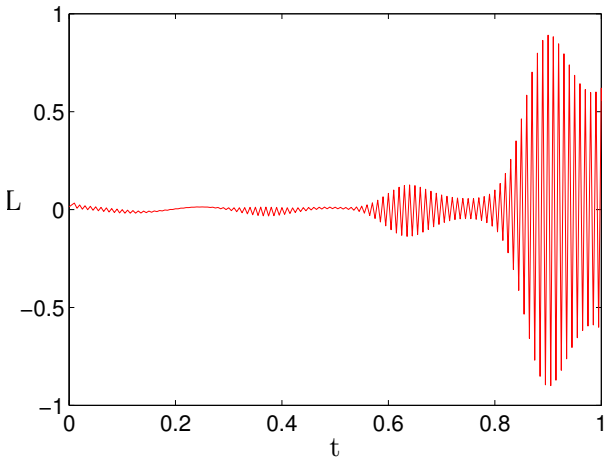

Figure 4.36: Instabilities at large values of λ

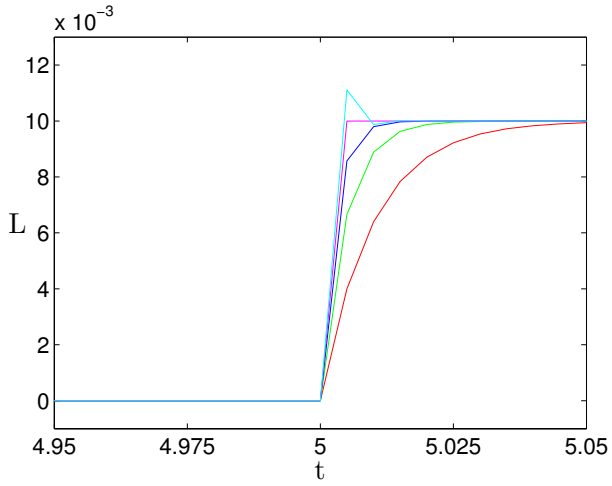

Figure 4.37: Overshoot at large values of λ

$\lambda = 100, 10, 1, 0.1$ and 0.01 will be investigated and their times taken to reach 90% of the demanded control input are 0.02t, 0.23t, 2.30t, 23t and 230t respectively. It is important to understand these lags in relation to the dimensional and non-dimensional periods of rotation as this will indicate the levels of attenuation possible for considering the actual smart rotor response rates.

Figure 4.38 shows the error for the two term ILC ($\mu_0 = 15$, $\Delta = 0$ and $\mu_1 = 90$) when applied to the disturbance in case flow-12 (T=2.5,amp=0.1, 2 vortices, 0° AoA) with actuator lag values $\lambda = 100$ and 10.

The results illustrate that the value of $\lambda = 100$ produces an attenuation very close to that of the instantaneous controller and $\lambda = 10$ results in poorer performance as the effects of the vortices and periodic disturbance in the flow become more pronounced in the error response. Reducing the value of λ further reduces the level of attenuation and results in an error signal similar to the uncontrolled flow, as shown in Figure 4.39. This

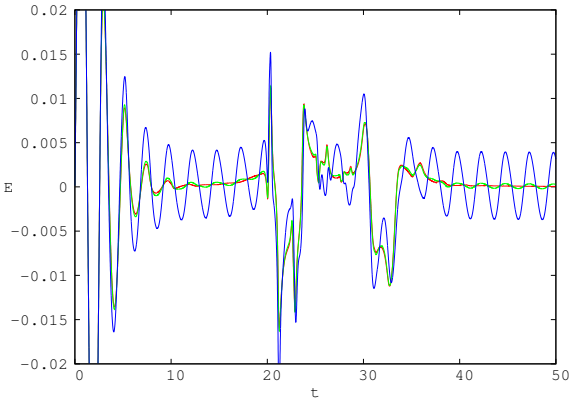

Figure 4.38: Error E^k for controller (4.5)-(4.7) with $\mu_0 = 15$, $\Delta = 0$ and $\mu_1 = 90$ applied to Case Flow-12 with no lag (red), $\lambda = 100$ (green) and $\lambda = 10$ (blue).

is an indication that the amount of actuator lag is a limiting factor in achieving the desired attenuation.

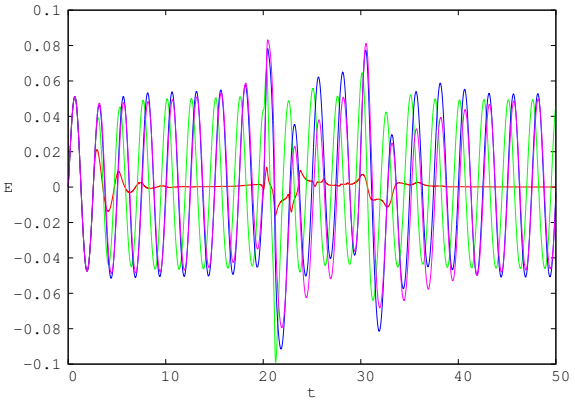

Figure 4.39: Error E^k for controller (4.5)-(4.7) with $\mu_0 = 15$, $\Delta = 0$ and $\mu_1 = 90$ applied to Case Flow-12 with no lag (red), $\lambda = 1$ (green), $\lambda = 0.1$ (blue) and $\lambda = 0.01$ (magenta).

Figure 4.40 illustrates the different control input responses for the λ values in Figures 4.38 and 4.39. The controller is activated after one full period has elapsed (2.5t in this case). As expected, increasing the value of λ results in a faster control response with $\lambda = 100$ producing an almost identical control input to the idealised instantaneous actuator. Decreasing values of λ results in a much slower response, hence the reduced levels of attenuation for smaller values of λ as the flow field does not change quick enough to counteract the flow disturbances.

Figure 4.41 illustrates the performance metrics ratios, $\mathcal{L}_2$ and $\mathcal{L}_\infty$, for Case Flow-12, Flow-15A and Flow-16 (See Tables 4.2 and 4.3) with different values of λ using the two term ILC controller ($\mu_0 = 15$, $\Delta = 0$ and $\mu_1 = 90$).

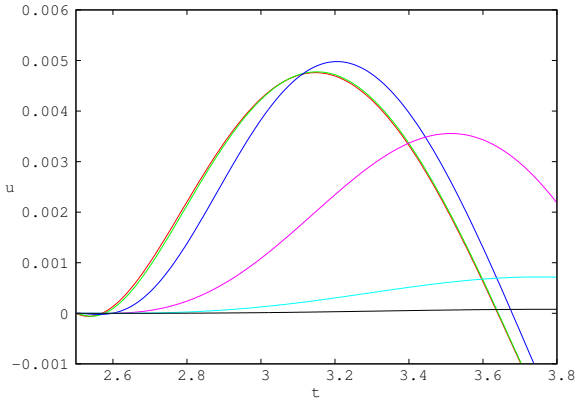

Figure 4.40: Control inputs u^k for the actuator lags λ in Figures 4.38 and 4.39. No lag (red), $\lambda = 100$(green), $\lambda = 10b$ (blue), $\lambda = 1$ (magenta), $\lambda = 0.1$ (light blue), $\lambda = 0.01$ (grey).

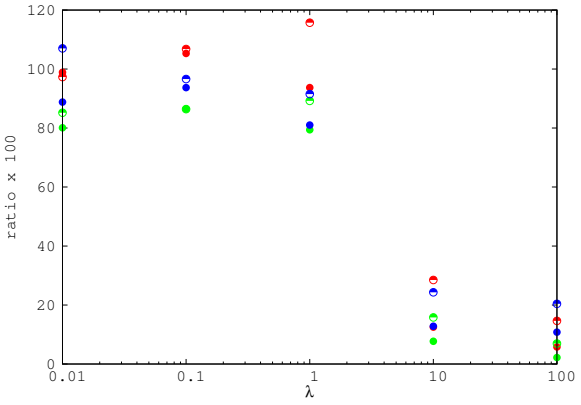

Figure 4.41: $\mathcal{L}_2$ (solid colour) and $\mathcal{L}_\infty$ (partial colour) norms for controller (4.5)-(4.7) with $\mu_0 = 15$, $\Delta = 0$ and $\mu_1 = 90$ applied to Case Flow-12 (red), Flow-15A (green) and Flow-16 (blue) with $0.01 \leq \lambda \leq 100$.

The figure illustrates a common conclusion across all cases that $\lambda \geq 10$ give significantly improved attenuation when compared to $\lambda \leq 1$. $\lambda = 10$ produces metric values within approximately 4% of instantaneous actuator results for all three cases, with only Case Flow-12 $\mathcal{L}_\infty$ metric increasing by approximately 10%. The performance metrics shown in Figure 4.41 are for flow cases with a relatively small period of $T = 2.5$. As discussed previously, this represents a very fast spinning turbine and is not physically realistic. Increasing the value of T gives a more realistic representation of the turbine dynamics and a more pragmatic analysis of the actuator requirements can be performed.

Figure 4.42 illustrates the error signals when applying the two term controller to Case Flow-19 ($T = 20$ with 12 vortices, Table 4.2) with actuator lag values of $0.01 \leq \lambda \leq 100$.

Greater attenuation is achieved when comparing the same λ values for an increased period which suggests that a defined level of attenuation, in terms of the performance

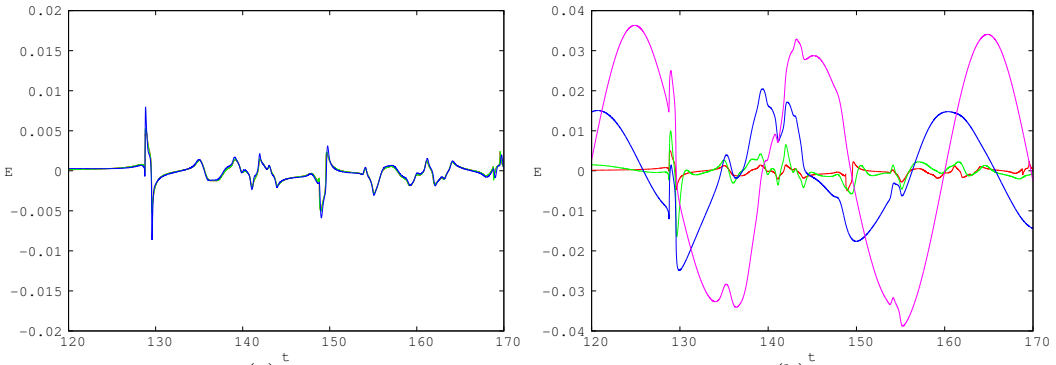

Figure 4.42: Error E^k for controller (4.5)-(4.7) with $\mu_0 = 15$, $\Delta = 0$ and $\mu_1 = 90$ applied to Case Flow-19 with (a) no lag [red], $\lambda = 100$ [green] and $\lambda = 10$ [blue] and (b) no lag [red], $\lambda = 1$ [green], $\lambda = 0.1$ [blue] and $\lambda = 0.01$ [magenta]

metrics, can be achieved with smaller λ values. In terms of smart rotor application, this indicates that as the non-dimensional period increases, more lag on the actuator response is acceptable. This result also holds true for cases flow-17A and flow-17B as shown in Figure 4.43. The λ threshold for reasonable performance (approximately a reduction of the metrics to 20% of the uncontrolled case) has reduced by an order of magnitude when considering these higher period flow regimes. Performance only significantly deteriorates for $\lambda \leq 0.1$. Figure 4.42(b) illustrates the error becomes larger still and drifts out of phase as the value of λ is reduced to 0.01.

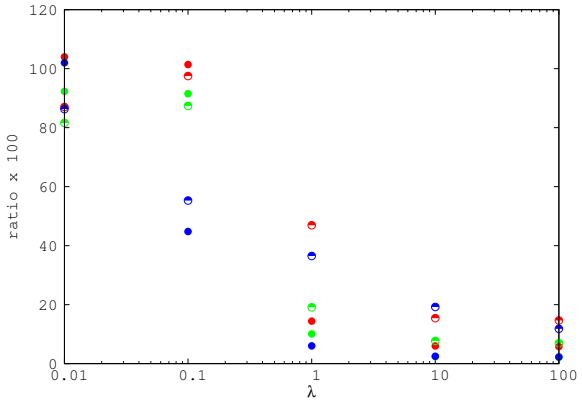

Figure 4.43: $\mathcal{L}_2$ (solid colour) and $\mathcal{L}_\infty$ (partial colour) norms for controller (4.5)-(4.7) with $\mu_0 = 15$, $\Delta = 0$ and $\mu_1 = 90$ applied to Case Flow-17A (red), Flow-17B (green) and Flow-19 (blue) with $0.01 \leq \lambda \leq 100$.

For Case Flow-19 (T=20, 12 vortices) a value of $\lambda = 1$ produces a reasonable level of attenuation. The performance metric used to estimate the fatigue loading on the blade $\mathcal{L}_2$ is reduced to 6% of the uncontrolled case and the extreme load metric $\mathcal{L}_\infty$ is reduced to 36.5% of the uncontrolled case. This value of λ represents an actuator with a response time to 90% of the demanded control of 2.3t. This corresponds to 11.5% of the non-dimensional period. Translating this ratio to an actual turbine, to achieve the level of

attenuation shown for Case Flow-19 with $\lambda = 1$, the actuator would be required to reach 90% of its steady state value in approximately 0.6 seconds. This speed of actuation is possible with the application of modern trailing edge devices (Berg et al., 2009).

4.7 Flow Configurations

The analysis of the more physically realistic plant model covered in section 4 has expanded on simple flow structures to include variable period flow in addition to the deterministic and non-deterministic flows defined in section 3. Additionally, the modelling of actuator dynamics has enhanced the analysis further with an appreciation of how the control system would perform with imposed hardware restrictions. In a similar manor to the flow configuration analysis in section 3, this section will test the robustness of the controller for a range of variation in flow parameters. Each parameter will be varied in turn and results for the complete model are shown in section 4.8 which include the addition of actuator dynamics. Table 4.2 shows the parameter settings for the representative test cases (note the flow cases numbers are a continuation from the previous sections). Initially, the same two-term ILC as described in previous sections is applied ($\mu_0 = 15$, $\Delta = 0$ $\mu_1 = 90$) using the direct lift and no actuator lag. The lift estimator and actuator lag are reintroduced in section 4.8 (complete model). Note baseline Case Flow-12 has performance metrics of 5.6%(L_2) and 13.1%(L_∞).

Case	Description	Vortex Strength	*AoA*	Amplitude	Period	Target Lift
15A	AoA+	medium	7°	0.1	2.5	0.745
15B	AoA-	medium	−7°	0.1	2.5	-0.014
16	Vortex Strength	strong	7°	0.1	2.5	0.745
17A	Period+	medium	0°	0.1	20	0.370
17B	Period+, AoA+	medium	7°	0.1	20	0.745
18	Target lift	medium	0°	0.1	2.5	0.471
19	Multiple vortices	weak x12	0°	0.1	20	0.370

Table 4.2: Parameters for selected cases using the baseline two-term ILC

Table 4.3 presents the performance metrics and ratios for the flow configurations outlined in figure 4.2. Flow configuration variables are discussed in the sub-sections below.

4.7.1 Steady State Angle of Attack (Case Flow-15A and 15B))

For Case Flow-12 (section 4.2), the two term ILC produces a reduction of two orders of magnitude in L_2 (5.6%), and a value of L_∞ less than 20% of that for the uncontrolled flow (13.1%), and is the flow condition used in the previous two chapters. The aerofoil is at zero degrees angle of attack in Case Flow-12. Pitch control (adjusting the AoA) can be used in order to maintain a near constant loading on the turbine as the mean flow rate varies so it is likely the aerofoil will operate across a range of different angles of attack. For 7^o AoA, with the same flow parameters as above and two vortices starting

case	norm	no control	control	ratio×100
15A	$\mathcal{L}_2$	0.0901	0.0038	4.2
	$\mathcal{L}_\infty$	0.1642	0.0188	11.5
15B	$\mathcal{L}_2$	0.015	0.002	14.1
	$\mathcal{L}_\infty$	0.064	0.018	28.2
16	$\mathcal{L}_2$	0.0926	0.0097	10.4
	$\mathcal{L}_\infty$	0.2605	0.0533	20.5
17A	$\mathcal{L}_2$	0.0440	0.0025	5.8
	$\mathcal{L}_\infty$	0.1389	0.0203	14.6
17B	$\mathcal{L}_2$	0.0970	0.0021	2.2
	$\mathcal{L}_\infty$	0.2117	0.0146	6.9
18	$\mathcal{L}_2$	0.105	0.006	5.9
	$\mathcal{L}_\infty$	0.182	0.002	11
19	$\mathcal{L}_2$	0.0239	0.0006	2.6
	$\mathcal{L}_\infty$	0.0449	0.0051	11.3

Table 4.3: Performance metrics for selected cases using the two-term ILC

in the same positions, the values of L_2 and L_∞ slightly improve with an increase in reduction to 4.2% (L_2) and 11.5% (L_∞). The change in AoA in the non wake flow model in section 3 exhibited a similar change in performance metrics in response to a change in angle of attack. The principle reason for the reduction in the performance metric ratio is the fact the uncontrolled error metrics are significantly higher when the AoA is increased. The target lift value ($Lr = 0.745$) is obtained from running the code with undisturbed flow, $V_{0x} = 1$ and 7^o AoA. Repeating the simulation with the same conditions and controller with the exception of the AoA been set to -7^o, results in much higher performance metrics. This is understandable because the initial no controller case metrics are much smaller. The controller appears to be stable across different steady state changes in AoA with a similar level of effectiveness when vortices are present for the non-wake and wake flow models. The range of AoA chosen roughly represents the typical range the aerofoil will operate in under normal conditions with attached flow.

4.7.2 Vortex Strength (Case Flow-16)

A more extreme case is obtained by changing the strength of vortex two to $\Gamma_2 = -\frac{4}{10}$. As this vortex contains (in magnitude) over a quarter of the circulation of that bound to the airfoil in the reference condition, this case can be regarded as a severe test of the control scheme. There is now a much larger deviation from the reference value of the lift, with the maximum value of the lift more than double the reference value, reflecting the strength of vortex 2, but, again, given the extreme nature of this test, the control performs well. The effect of the much stronger second vortex can be seen in the performance metrics with both ratios approximately doubling when compared to the baseline vortex strengths to 10.4% ($\mathcal{L}_2$) and 20.5% ($\mathcal{L}_\infty$).

4.7.3 Variable Period Flow (Case Flow-17A and 17B)

As mentioned earlier, both the chord length H and the reference velocity V_∞ will vary along a turbine blade, which implies an increase in the non-dimensional period of the oscillation T, moving towards the tip (as $t^* = \frac{H}{V_\infty}t$). All the calculations so far have used $T = 2.5$, which represents a relatively fast rotating turbine (approximate period of 0.04 seconds). This enabled the interaction between the forced oscillation, the convective disturbance represented by the vortices and the control scheme to be investigated with a relatively small computational effort. In practice, T would be much larger. Figure 4.44 shows the error for a run with two vortices, no control, 0° AoA and $T = 20$ over the time that the vortices pass the airfoil (case 17A). Figure 4.44 also shows the two-term ILC controlled case with $\mu_0 = 15$ and $\mu_1 = 90$. The vortices now start much further upstream, at $(-125, 0.25)$ and $(-119, 0.25)$, with strengths $\Gamma_1 = 0.1$ and $\Gamma_2 = -0.1$. Again there is a relatively large fluctuation as the vortices pass, but this now occurs over a short time relative to the period of the blade rotation. The disturbances are largely attenuated, with a two and one order of magnitude reduction in $\mathcal{L}_2$ and $\mathcal{L}_\infty$ respectively, 5.8% and 14.1%. The airfoil is then pitched to 7° AoA and the control works very well with two orders of magnitude reduction in the error (case 17B, Table 4.3), 2.2% ($\mathcal{L}_2$) and 6.9% ($\mathcal{L}_\infty$).

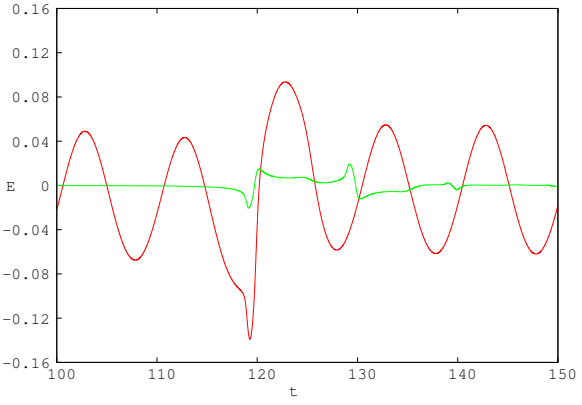

Figure 4.44: No control error E^k for Case Flow-17A (red). Error E^k for controller (4.5)-(4.7) with $\mu_0 = 15$, $\Delta = 0$ and $\mu_1 = 90$ applied to Case Flow 17A (green).

4.7.4 Target Lift (Case Flow-18)

The reference value used in the results presented above is the lift on the aerofoil with a steady mean velocity, but there is also interest in using smart blades to increase aerodynamic performance, particularly at low speeds. A number of simulations were run using a different value as the target lift. Figure 4.45 shows the error when the control is applied to a flow with A = 0.1 and T = 2.5 and two vortices passing the

aerofoil (as for case flow-12) but with a target value of the lift of $Lr = 0.474$, 25% higher than the value for uniform flow.

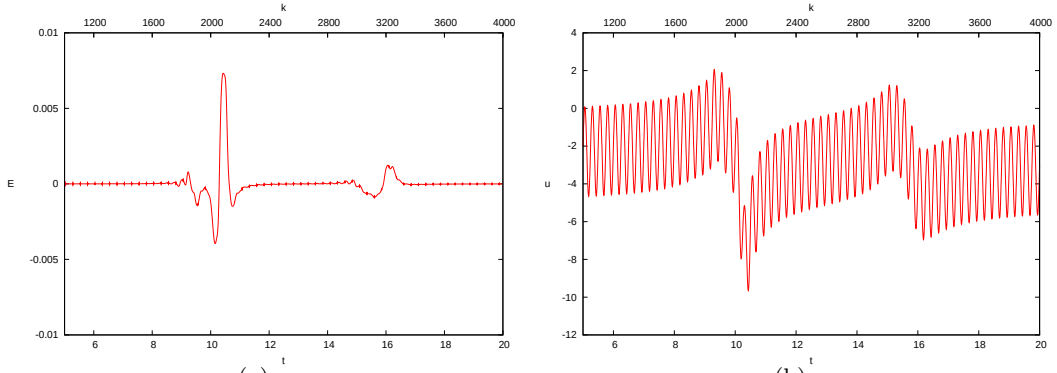

(a) (b)

Figure 4.45: Case flow-18, oscillatory flow with 2 vortices and 25 % increase in L_r, with two-term ILC applied. (a) Error E^k (b) Actuation u^k

This figure is similar to that for the case with the original (lower) reference value, and gives similar values for the performance measures of 5.9% ($\mathcal{L}_2$) and 11% ($\mathcal{L}_\infty$). Figure 4.45 shows the control signal u^k and it is very similar to the case with the original reference value, but displaced downwards to compensate for the increase in the target value. Similar performance for variable target lift was seen with the non-wake flow model.

4.7.5 Multiple Vortices (Case Flow-19)

For all the results presented so far in the wake flow model section, only a few strong vortices have been used, generating large disturbances in the flow. Figure 4.46 shows the fluctuation in the lift for a run with 12 relatively weak vortices ($\Gamma_j = \pm 0.01$) as the vortices pass the airfoil when there is no actuation ($u^k = 0$), a period of $T = 20$ and a 10% amplitude in the free stream velocity oscillation ($A = 0.1$). In this case, the vortices generate relatively weak changes in the lift, superimposed on the oscillation from the unsteady nature of the free stream. 4.46 shows the error in the lift with the application of two-term ILC and the control input. Again there is a two order of magnitude reduction in $\mathcal{L}_2$, and just above a 10% reduction in $\mathcal{L}_\infty$ (case flow-19, Table 4.3). The attenuation level of the error signal is similar to that found in other cases with stronger disturbances, and is still acceptable. Figure 4.46 highlights the ability of the ILC algorithm to track the lift disturbance as the control input response is the same shape as the disturbance, essentially oscillatory but with relatively short-scale fluctuations generated by the vortices.

In addition to the six cases listed in Table 4.2, well over a 100 other runs were performed, with different amplitudes and periods of oscillations, numbers and strengths of vortices, at $-7°$, $0°$ and $7°$ AoA. The values given in Table 4.3 are representative.

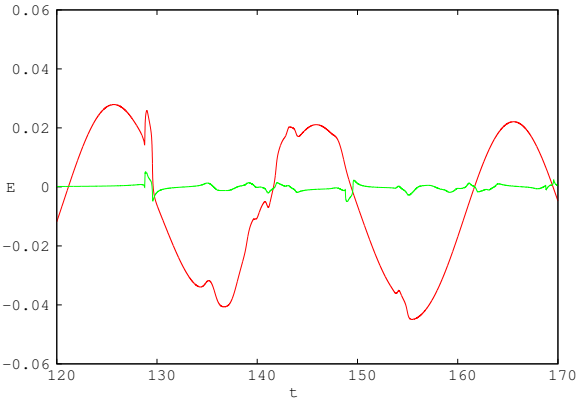

Figure 4.46: No control error E^k for Case Flow-19 (red). Error E^k for controller (4.5)-(4.7) with $\mu_0 = 15$, $\Delta = 0$ and $\mu_1 = 90$ applied to Case Flow-19 (green).

4.8 Real Turbine Data (Non-Deterministic)

In a similar manor to section 3.8, this section focuses on integrating the previous subsection models to obtain an understanding of ILC performance in a realistic flow that represents a turbine smart rotor with wake effects and representative actuator and sensor characteristics considered. The development, in order, of the complete model will consist of applying two-term ILC to (a) a realistic inflow disturbance of the freestream velocity; (b) the addition of multiple stochastic vortices in the inflow; (c) replacing the direct lift with the lift estimator developed in section 4.5 and (d) integrating the actuator dynamics to represent a realistic lag in the actuator response. Evolving the analysis in this way enables insight into the coupling between assumptions made about the plant or controller model with wake and actuator dynamic effects now included.

As in the previous non-wake model analysis a representative period of $T = 20t$ will be used in this section. The computation takes longer for the flow model with the inclusion of the wake model therefore the runtime for the cases in this section has been reduced to $200t$. This runtime is still adequate to capture the controller dynamics and stability as the runtime will allow for 10 periods of freestream velocity oscillations. Table 4.4 summarises the performance metrics for the flow cases discussed in this section.

case	norm	ratio×100
(a) Real inflow	$\mathcal{L}_2$	1.3%
	$\mathcal{L}_\infty$	2.1%
(b) (a) + vorts	$\mathcal{L}_2$	5.2%
	$\mathcal{L}_\infty$	3.4%
(c) (b) + lift estimator	$\mathcal{L}_2$	6.8%
	$\mathcal{L}_\infty$	7.2%
(d) (c) + actuator delay ($\lambda = 1$)	$\mathcal{L}_2$	14.7%
	$\mathcal{L}_\infty$	21.5%

Table 4.4: Performance metrics for complete wake flow model iterations

Figure 4.36 shows the real turbine data from Thomsen et al.(2008) scaled to an approximate period of T=20 and A=0.1 with the baseline two term ILC developed in section 4.2. The period and amplitude are fluctuating in a manor representative of actual turbine inflow data.

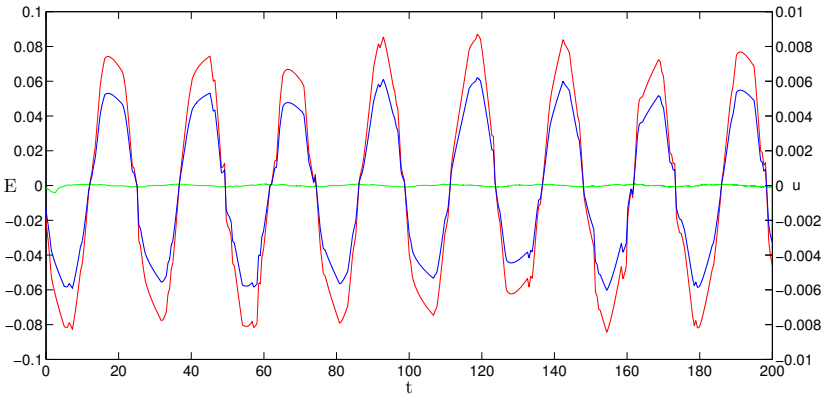

Figure 4.47: Two-term ILC applied to non-dimensionalised real turbine data (Case Flow-20) with $\mu_0 = 15$, $\Delta = 0$, and $\mu_1 = 90$ uncontrolled error (red), controlled error (green) and control input (blue)

The results shown very good attenuation with performance metric ratios of of 1.3% (L_2 and 2.1% ((L_∞). It is reasonable to expect the controller to perform well with this inflow because analysis has already shown that the two-term ILC algorithm is adept at coping with fluctuations in the freestream velocity period and amplitude variations aligned with those found in real turbine data with the additional of a wake model.

The addition of vortices in previous section has introduced additional stochastic effects into the system and the same method is applied here. Twenty vortices are introduced upstream of the aerofoil to ensure a vortex arrives at the aerofoil leading edge every 10t. All vortices have the same strength of 0.02 and start every $10x$ horizontally upstream of the aerofoil but the y starting position is randomised to ensure a random distribution of vortices above and below the aerofoil. Figure 4.37(a) shows the system response when the baseline two-term ILC is applied to the flow structure with twenty vortices. Figure 4.37(b) shows a more detailed plot of the inflow disturbance with and without vortices. The performance metrics for this case are 5.2% (L_2 and 3.4% ((L_∞) which are only slightly higher than the case with no vortices.

Figure 4.48: (a) Two-term ILC ($\mu_0 = 15$, $\Delta = 0$, and $\mu_1 = 90$) applied to real turbine data with x20 vortices uncontrolled error (red), controlled error (green) and control input (blue). (b) Lift disturbance no vortices (dashed grey), vortices (magenta)

The controller used in all of the simulations in this section thus far have utilised the direct lift from the model. In section 4.5, a 11 sensor array was developed and the same sensor array is now used in the two-term ILC algorithm in the presence of the flow disturbance shown in Figure 4.37. Figure 4.38 shows the system response when replacing

the direct lift with the estimated lift. As expected the level of attenuation drops when compared to the direct lift control but performance metrics are still reasonable with values of 6.8% (L_2) and 7.2% (L_∞).

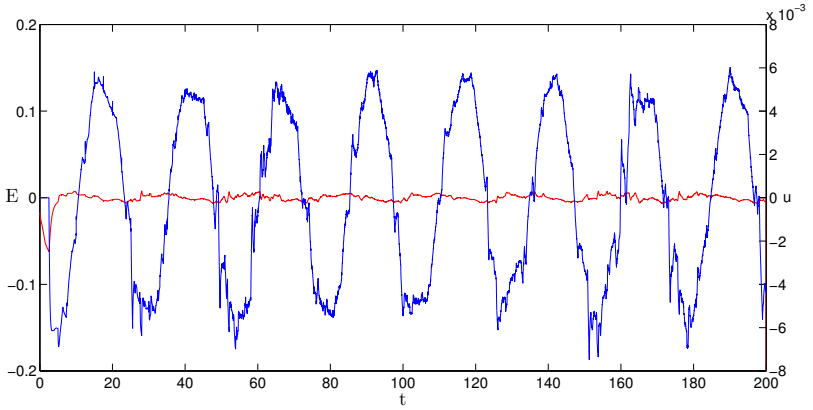

Figure 4.49: Two-term ILC applied to non-dimensionalised real turbine data with $\mu_0 = 15$, $\Delta = 0$, and $\mu_1 = 90$, estimated lift from a 11 sensor array. Controlled error (red), control input (blue).

The next stage in developing a representative complete model is to integrate the lag of the actuator response to a commanded control input. Sections 3.6 and 4.6, have shown that increasing the speed of the actuator response results in an increase in performance and reduction in the performance metrics for both the wake and non-wake model. To gain an understanding of the effect of the actuator response rate on the configuration developed in Figure 4.38, a range of actuator lags are modelled in Figures 4.39 to 4.41. The simple actuator model developed in section 4.6 is used with values of $\lambda = 100$, 10, 1, 0.1 and 0.01.

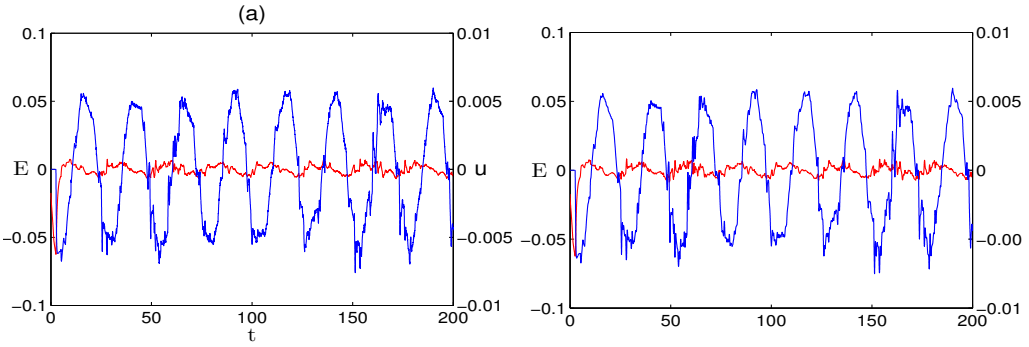

Figure 4.50: Two-term ILC ($\mu_0 = 15$, $\Delta = 0$, and $\mu_1 = 90$) applied to real turbine data with twenty vortices using a lift estimate as the controller input and an actuator lag of (a) $\lambda = 100$ and (b) $\lambda = 10$. Controlled error (red), control input (blue).

The results seen in sections 3.6 and 4.6 hold true for the specific flow configuration and system model in this section. As the value of λ decreases and the actuator response becomes slower, the level of attenuation decreases. Figure 4.41 shows that a value of $\lambda = 0.01$ produce poor attenuation because the flow field responds very slowly to the

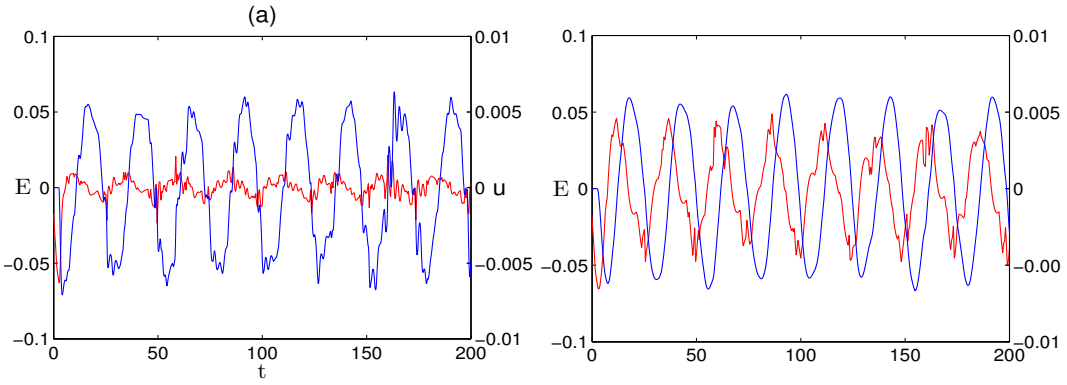

Figure 4.51: Two-term ILC ($\mu_0 = 15$, $\Delta = 0$, and $\mu_1 = 90$) applied to real turbine data with twenty vortices using a lift estimate as the controller input and an actuator lag of (a) $\lambda = 1$ and (b) $\lambda = 0.1$. Controlled error (red), control input (blue).

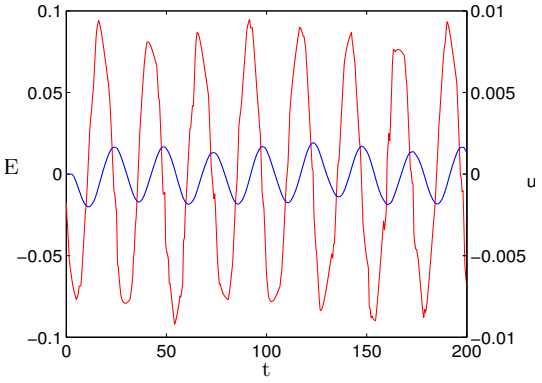

Figure 4.52: Two-term ILC ($\mu_0 = 15$, $\Delta = 0$, and $\mu_1 = 90$) applied to real turbine data with twenty vortices using a lift estimate as the controller input and an actuator lag of $\lambda = 0.01$. Controlled error (red), control input (blue)

required circulation change demanded and within half a cycle the control does not have time to create any significant effect on the flow field before the controller is demanded a circulation change in the opposite direction. It is unlikely this actuator lag would cause any significant instabilitys or non-minimum phase behaviour but the attenuation level will always be poor. Reasonable attenuation is achieved for values of $\lambda >= 1$ with performance metrics of 14.7% (L_2) and 21.5% (L_∞). This equates to an actuator response time of approximately 10% of the fluctuation period in the freestream velocity. If investigation yielded that the demanded control outputs were not possible in terms of circulation change generated by the chosen actuator then the control inputs would be clipped and result in reduced attenuation and an increase in the performance metrics.

4.9 Summary

The analysis path in section 4 has followed a similar route to that found in section 3 but with more detailed plant and controller modelling. This is a deliberate attempt to highlight the implications of including a more detailed wake model in the flow model when applying ILC. A comparison of the two sets of results can be found in the conclusion (section 5). Section 4 provides evidence of success in applying different forms of ILC to a range of flow conditions with the additional of smart rotor sensor and actuator dynamics. The flow model is a simple vortex panel method with a wake model that is only suitable for attached flow but stochastic aerodynamic effects have been introduced to the system with the incorporation of upstream discrete vortices in addition to the wake vortices leaving the trailing edge. The success of the controllers ability to attenuate disturbances in lift has been measured by using performance metrics L_2 and L_∞ as a representation of the fatigue and extreme loading respectively.

Initially a proportional controller and phase-lead ILC were developed and applied to simple oscillatory disturbances in the freestream velocity. These algorithms were adequate when attenuating a simple linear, deterministic system but performance significantly reduced with the introduction of stochastic vortices. A solution was developed to combine the two forms of ILC into a two-term ILC algorithm that could account for the vortical disturbances using the proportional controller and the freestream oscillations using the phase-lead ILC. The simple structured two-term ILC performed well when considering the system outputs only. This ensures simple hardware implementation as there is no requirement for a state space model.

The results indicate good two-term ILC performance across a range of nonlinear and stochastic flow conditions with the inclusion of the wake model. The same controller and flow model with the wake model was tested for approximately 20 flow test cases with various different combinations of period, amplitude and vortex distribution. All performance measures fell below 30% of the uncontrolled case.

After simulation of perfectly sinusoidal disturbances in the freestream velocity, the analysis then considered wake flows with a variable period (section 4.3) and harmonic/non-harmonic composition flows (section 4.4) in freestream velocity disturbances. The real turbine data is the closest to reality in as this data has been taken from an instrumented turbine and contains actual variations in the turbine period of oscillation, amplitude and noise. The same two-term ILC algorithm was applied to this range of flow conditions and good levels of attenuation were still possible.

The system outputs considered by the ILC algorithm in the applications mentioned above have all derived the error from the direct lift and the control input. Section 4.5 considers the implications of applying the two-term ILC that references an estimated lift in the error calculation. This step moves the analysis towards practical implementation

because measuring direct lift on a wind turbine smart rotor section would be problematic. The lift estimation generated is based on a pressure sensor array. The design of an adequate array has been outlined with the effects on the performance metrics quantified. The wake model sensor array (4.5.2) is very similar to the non-wake sensor array (section 3.5.2) with the main difference been the removal of one leading edge pressure side sensor that gave poor lift correlation when including the wake model. As with the non-wake model, increasing the number of sensors improves the estimate with a preference to not position sensors on the leading and trailing edge extremities to avoid poor lift estimation. Replacing the direct lift with a pressure sensor derived lift estimate resulted in slightly reduced attenuation with a standard case dropping from performance metrics of 5.6% (L_2) and 13.1% (L_∞) to 7.6% (L_2) and 14.2% (L_∞).

Actuator dynamics have been integrated into the analysis by applying a first order lag onto the control input. This is a simplified method of capturing the fact the actuator device will take an amount of time to respond to a command and effect the aerofoil flow. It has been shown that increasing the time lag on the actuator has a detrimental effect on the ILC algorithms ability to attenuate disturbances both with a without the wake model. An approximate value of $\lambda = 10$ is the minimum value required to retain respectable attenuation with a period of $T = 2.5t$. This value of λ equates to approximately 10% of the period of oscillation. For a typical turbine operating at nominal conditions, this equates to a actuator response time of approximately 0.5 seconds which is feasible with modern actuation methods.

Performance metrics are reasonably consistent across all flow configurations analysed in section 4.7, with the highest performance metrics of 14.1% (L_2) and 28.2% (L_∞) for case flow-15B. Positive angle of attack variation (section 4.7.1), variable period freestream flow (section 4.7.3) and offset target lift (section 4.7.4) have minimal impact on the performance metrics when using the wake flow model. The ILC algorithm gains remain fixed throughout ($\mu_0 = 15, \Delta = 0, \mu_1 = 90$) and all simulations show a stable lift response with significant attenuation. The only increase in performance metrics values occurs when the angle of attack is made negative, the strength of the vortices are increased and multiple vortices are present. In the latter two instances the resultant effect on the uncontrolled lift fluctuation is significant vortex induced variations in the lift. For example, the increase in vortex strength in section 4.7.2 equates to approximately half of the circulation on the aerofoil. This is a very extreme case which in reality is unlikely to occur. Understandably there is a significant effect on the performance metrics for this case, with the value of (L_2) and (L_∞) approximately doubling. However, both metrics fall below 20% percent and importantly the system response remains stable under these extreme flow configurations. The intention of increasing the vortex strength is to show the controller design is robust and the results have shown this to be true. Making the angle of attack negative has a significant effect on the performance metric ratios but

this is largely driven by the low performance metrics values for the uncontrolled negative angle of attack case.

The above discussion focuses on varying flow parameters in isolation whereas section 4.8 considers the integration of all flow variables and the inclusion of sensor and actuator behaviour. The controller gains remain fixed to the baseline values of $\mu_0 = 15, \Delta = 0, \mu_1 = 90$ to avoid the need of applying variable gain controllers that are traditionally more complex and less robust to instabilities. The same controller design adequately controls the lift disturbances as the complexity of the flow model increases and actuator and sensor characteristics introduced. The simulations are run over a larger time scale of 200t to increase confidence in algorithm stability. With the vortices present, the system is stochastic so traditional analytical stability control techniques cannot be used. Real turbine data is used as the input disturbance in the freesream velocity and the controller attenuate well for the case with and without vortices. The vortex frequency is approximately twice per cycle and causes no issues with the ability of the ILC to attenuate well. Performance metrics fall below 6% for both non-vortex and vortex flow.

These performance metrics are based on idealised sensor and actuator behaviour, i.e. exact lift calculation and instantaneously responding actuation and circulation change on the aerofoil. This is clearly not realistic so the plant model is advanced to mimic the behaviour of an actual system. Replacing the direct lift with an estimated lift provided to the controller has little effect on the ILCs ability to attenuate. The estimator is adequate at providing accurate lift information to the controller for large periods and frequencies and strengths of vortices seen in Figure 4.37.

A decisive contribution to the effectiveness of a smart rotor system using ILC appears to be the response rate of the actuation system. A first order lag is applied to the control input and applied to the flow configuration of the complete model using lift estimation as a control input. Figures 4.39 to 4.41 show the significance of reducing the speed of the actuator response and the fact a very slow actuator can lead to the circulation change having very little impact on the flow disturbances. The actuator needs to achieve a time constant of approximately 10% of the period of rotation in order to achieve satisfactory levels of attenuation. This is one of the advantages of localised actuation inherent in smart rotors, as they have a very good chance of achieving this response rate whereas full blade pitching would struggle.

Chapter 5

Conclusions

5.1 Summary of Contributions

This piece of research has contributed to the knowledge of Iterative Learning Control within the context of a fluid mechanics problem, specifically smart rotor systems on wind turbines to improve aerodynamic performance. Application of ILC in the field of aerofoil aerodynamics is rare and this work is the first known study into the feasibility of using ILC for wind turbine smart rotors. This is the first time a nonlinear vortex panel method has been used to accurately model a 2D wind turbine aerofoil with the application of ILC within the framework of typical wind turbine flow conditions. The uniqueness of the work presents a quantitative study of combining a simple ILC scheme that only considers the fluid mechanics plant model outputs with more traditional integral and proportional control. The principle advantage of the ILC investigated over more traditional PID control is the removal of the delay inherent in a closed loop feedback system. The ILC algorithm takes advantage of the data available from previous rotations of a wind turbine to efficiently iterate towards the ideal control command profile that will result in reduced blade loading.

The smart rotor concept provides significant advantage to wind turbine design but the standard methods of actuation, sensing and control have yet to be defined. This work considers a realistic and non-specific method of actuation and sensing in order to analyse the effectiveness of ILC with the primary objective of reducing fatigue and extreme loads experienced by a wind turbine during normal operation. The reduction of these loads leads to lighter, larger and more reliable turbines that will ultimately have the potential to reduce the cost of wind energy. This work does not provide evidence of improved control performance of smart rotor systems when compared to more traditional pitch control techniques as this is well established within the field.

A simple CFD model based on a panel method has been applied to the problem of oscillatory flow past an airfoil with vortical disturbances in the flow, interacting stochastically

with the airfoil, and with trailing edge vorticity or circulation generation for actuation, as a model of a section of a smart wing turbine rotor blade. The flow conditions have been extended to quantify the effect of variable period flow and composition flow with panel methods with and without a nonlinear wake model. These models have been used for a detailed initial investigation into the application of simple structure ILC in this area. The need to build a state-space representation of the dynamics was not required and the simple structure ILC laws can be designed by consideration of the system output. Two different measures were used to assess the ability of the method to damp the disturbances, an L_2 norm (fatigue load) and an L_∞ norm (extreme/peak load).

The research provides quantitative evidence on the suitability of ILC application for smart rotors and provides typical sub-system component limitations in terms of meeting the objective of reducing extreme and fatigue loading. It has been concluded that actuator dynamic response is a driving force in how much scope the smart rotor system has to attenuate lift disturbances. It has been estimated that the actuator time constant, in terms of creating the circulation demand required, needs to be less than 10% of the wind turbine period of rotation to have significant effect on the lift oscillations experienced by the turbine. However, the response time required to significantly damp out the effect of convective disturbances is much more demanding, approaching frequencies in the kHz range for a flow actuation device towards the tip of a 100m blade. The number of pressure sensors used in the lift estimation as the controller input is also identified as a key performance factor. Reductions in the L_2 and L_∞ norms for the two-term ILC case with a real turbine inflow disturbance, wake vortex panel method, stochastic vortices convected twice per period, a 11 pressure sensor lift estimator and an actuator with a response rate of 10% of the period, resulted in reductions to 14.7% (L_2) and 21.5% (L_∞) of the uncontrolled case. The effect of limiting the magnitude of the actuator control input has been discussed at the end of section 4.

The conclusions made for this research are only valid for 2D, attached aerofoil flow. Separated flow and 3D effects are likely to affect the conclusions made and is an obvious area of further research. While attention has been allocated to actuator and sensing performance, this analysis has been strictly in terms of the effect upon the ILC algorithms ability to attenuate flow disturbances. Only qualitive discussion has been provided on the impact of the control command in terms of actuator and sensor degradation.

Although this thesis has concluded that only the oscillatory disturbances can be significantly attenuated unless more advanced sensing and actuator methods are developed, ILC in principle would be capable of integrating with traditional control schemes to attenuate fast moving flow convected disturbances. In the context of a wind turbine, attenuating only the slower, large period oscillations effectively is still worthwhile because these disturbances contribute to most of the blade loading. The application of actual turbine data has shown that disturbance scales between periodic fluctuations, due to the atmospheric boundary layer, and small scale vortices can be attenuated using ILC

with realistic actuator and sensor specifications. An example of such a disturbance is a large scale gust. The ILC is inherently taking advantage of the dynamics of the turbine system by utilizing previous cycle control and error information. The results show stability over a wide range of flow disturbances, configurations and vortex strengths that add evidence to the robustness of the ILC algorithm for the application in question. The control laws in this thesis have simple hardware implementations, whereas model-based methods often require state estimation and added complexity to the local controller hardware. Model-based ILC design is mature and an obvious area for further research is to consider these techniques for this application by constructing a state-space model representation of the dynamics from the CFD-generated data. The results in this thesis provide a significant step towards quantifying the potential of ILC for smart rotor application before developing more complex model based designs and eventually experimental turbine testing.

5.1.1 Flow Model

The plant model used is of sufficient detail to gain confidence in the above conclusions. The vortex panel method considers the shape of the aerofoil as opposed to simpler methods (e.g. thin aerofoil theory) and is fully nonlinear when considering the wake effect of the vortices leaving the trailing edge every time step. The two main sections of the work have similar analysis structures with the intent of highlighting the significance of including the nonlinear wake model. The wake model is a more accurate representation of the actual conditions on the turbine so is the preferred model but it is inherently more computationally expensive, so advantages would be gained if the non-wake model was adequate in particular scenarios. An initial observation is that the inclusion of the wake model makes the ILC scheme more robust to variations in the previous time step offset, Δ. The non-wake flow model allows for very little change in the value of Δ before instabilities arise whereas the inclusion of the wake model enables the value of Δ to vary by $+/-8$ time steps. It is therefore recommended to avoid using the non-wake model when undertaking stability analysis and controller gain design because the flow model could drive instabilities that would not be present in the actual system. The stability margin seen in the wake model also provides robustness to system errors, such as cumulative electronic and mechanical component errors. The inclusion of the wake model effectively creates a lag on the lift change of the aerofoil due to flow disturbances. Results show that this means less aggressive changes in lift and an allowance for a slightly slower responding actuator. This lag effect is also responsible for the phase difference seen between the control input and the lift response when the wake model is introduced. Because the ILC algorithm accounts for the flow behaviour in previous cycles, the wake lag effect is automatically considered and no algorithm offset is required to avoid instability or poor performance.

The fidelity of the CFD model used could be improved to undertake more detailed study and is an opportunity for further work. More advanced CFD modelling techniques, such as direct numerical simulation, to replace the vortex panel method would likely uncover more insights into the suitability of ILC and wind turbine smart rotors. This approach would give more detail into the flow conditions and include all viscous effects and extend the validity of the analysis to non-attached flow. Additionally the flow characteristics of bespoke actuators and sensors could be analysed, their effects quantified and ultimately give results with greater confidence in smart rotor systems using ILC. Insights into flow phenomena such as separation bubbles, trailing edge separation or boundary layer interaction may or may not have a significant impact on ILC performance. It would also offer the opportunity to advance ILC schemes to include, for example, separation points as controller inputs.

The nature of the flow disturbances in the model offers another opportunity for further research. Currently only steady state variations in lift have been analysed. During a single rotation of a turbine blade, the angle of attack onto the blade varies. Modelling this within the current flow model would significantly increase computational effort but would give more insight into ILC schemes in the context of wind turbine applications. Moving the aerodynamic model into the 3D domain and coupling with a structural model would offer a new array of issues not tackled within the current work, predominately an insight into the link between load variations on a blade section and the forces at the blade hub. Forces generated at smart rotor locations at the tip would be larger but take longer to travel to the hub than devices further inboard, and would need to be considered when designing ILC algorithms with multiple inputs and outputs. A more detailed understanding of the vortex structures would be required in terms of frequency, magnitude and direction. Such 3D aero-elastic models would enable investigation of advanced topics such as blade to blade learning.

5.1.2 ILC

Sections 3 and 4 have quantified the effectiveness of ILC across the range of flow conditions relevant to wind turbine smart rotors. One of the early conclusions is that the ILC algorithm is effective at attenuating oscillations in the global lift caused by fluctuations in the freestream velocity, and the more traditional proportional type controller is suited to attenuating the stochastic disturbances from the discrete vortices. It has been shown that combining these two control philosophies results in an effective controller than can attenuate a range of flow disturbances typically experienced during normal wind turbine operation. The controller gains appear to be ok as fixed values, as opposed to requiring application of variable gains or gain scheduling. As discussed above, a value of $\Delta = 0$ is recommended, since this value allows for error while maintaining stability. When

analysing non-sinusoidal flows, it is apparent that the reference period in the ILC algorithm should be set to the value of smallest harmonic present. This value is expected to be the value of the period of rotation but there are scenarios where this may not be the case. For example, a faulty turbine might induce smaller harmonics within the system. Setting the ILC reference period to the smaller harmonics will ensure greater attenuation. The cut-off frequency would be set by the design engineer and deemed to be the frequency at which the effects of the disturbance on the blade fatigue loading are minimal. Because the application of ILC within the area is unique, there are a number of opportunities for further research. A 3D aero-elastic model, as discussed above, could be used to study the potential of using ILC for MIMO systems as a combination of multiple smart rotors, blade pitch control or both. This would also enable system level comparisons to other suitable control schemes (e.g. repetitive control, model predictive control, traditional PID control) that are at sufficient maturity in the context of wind turbine control. Further work at the 2D level could include a more detailed analysis of the control demand in terms of component wear and energy use. Solutions could include new controller objectives to offset wear and energy use against load reduction.

5.1.3 Smart Rotors

Simple specification requirements for smart rotor actuators and sensors have been developed but more detailed investigation is required into specific hardware devices. The lift estimator develop has successfully been used with the ILC algorithm to attenuate a range of flow disturbances. The level of attenuation is expectedly less than when using the direct lift from the vortex panel method. A critical point is the effect that introducing lift estimation has on the control input command profile. Integrating lift estimation into the control feedback results in a noticeably more aggressive control command profile. Whilst this is not quantified in this research, any further work on lift estimation would require consideration of the control input fluctuation and subsequent demand for actuator movement.

A general conclusion can be made from the results that periodic disturbances can be attenuated with fewer pressure sensors, compared to stochastic vortices. However, if the stochastic vortex effects are to be attenuated then the number of sensors needs to be increased. The sensor array design is an important consideration and poorly placed sensors can result in poor attenuation and potentially result in an unstable system. Recommendations across the non-wake and wake model are to avoid the leading and trailing edges, but ensure enough sensors are included to capture the movement and hence lift fluctuations generated by the vortices. A relatively even spread of sensors across pressure and suction surfaces is favourable over high density pressure sensor clusters. Areas with high density arrays tend to over-predict the influence of the vortex as it passes and underestimate the effect in less dense areas. If the fatigue loads are the design driver,

then potentially less pressure sensors can be deployed as the results indicate reasonable fatigue load reduction with fewer sensors. If extreme loads are the design driver, then more sensors would be required as Figure 3.17 indicates poor extreme load reduction for cases with four or less sensors. More advanced work with the pressure sensors could include system identification of flow disturbances and real-time on/off control of sensors.

One of the principle conclusions from this work is that traditional sensor and actuator characteristics means fast moving vortices convected with the wind cannot be attenuated significantly. It is unlikely refining the ILC scheme will yield any significant improvements with this current system specification. Either the sensing or actuation system needs to improve. A current research area within the wind turbine industry is LIDAR technology and an area for further research could be its application to ILC driven smart rotors. The LIDAR sensor would provide information of the disturbances that will interact with the blade before they arrive and give the actuation system more time to respond. Methods to improve the speed of the actuation method could include pre-layered composite structures that deflect into a predefined shape depending on the loads experienced. These devices would require very detailed analysis of the fluid-structure interaction behaviour and would not be suitable for analysis with the vortex panel method.

References

Ahn, H., Chen, Y., and Moore, K. (2007). Iterative learning control: brief survey and categorization 1998-2004. IEEE Transactions on Systems Man and Cybernetics Part C, vol. 37, p. 1099-1121.

Andersen, P. B. and Gaunaa, M. (2007). A dynamic stall model for airfoils with deformable trailing edges. Journal of Physics: Conference Series, Volume 75.

Andersen, P. B., Henricksen, L., Gaunaa, M. Bak, C. and Buhl, T. (2009). Deformable trailing edge flaps for modern megawatt wind turbine controllers using strain gauges. Wind Energy, Volume 13, Issue 2-3, p. 193-206, Special Issue: Smart Blades.

Andersen, P. B. (2005). Load alleviation on wind turbine blades using variable aerofoil geometry (2d and 3d study). MSc Thesis, DTU.

Andersen, P. B. (2010). Advanced load alleviation for wind turbines using adaptive trailing edge flaps: sensoring and control. PhD report: ISBN 978-87-550-3824-0.

Andersen, J. (1985). Fundamentals of aerodynamics. McGraw-Hill.

Barakos, G.N. (2005). CFD simulation of flow control devices for helicopter rotors. CEAS Conference on Key Aerodynamic Technologies, Bremen, Germany,

Barakos, G.N. (2006). Modelling 3d dynamic stall of helicopter blades using CFD and neural networks. Proceedings of the Institution of Mechanical Engineers, Part G: Journal of Aerospace Engineering June 1, 2006 vol. 220 p. 605-618

Barakos, G.N. (2009). Development and validation of a CFD technique for the aerodynamic analysis of HAWT. J. Sol. Energy Eng 131(3). doi:10.1115/1.3139144.

Barlas, T., Hulskamp, van Wingerden, J. W., Mroz, A., van Langen, P., Landa, M., and Apianiz, S. (2002-2006). Smart rotor blades and rotor control for wind turbines. UpWind funded under the EC 6th Framework Programme.

Barlas, T. and van Kuik, G. A. M. (2010). Review in state of the art in smart rotor control research for wind turbines. Progress in Aerospace Sciences. Volume 46, Issue 1, January 2010, Pages 127.

Behrens, T., Shen, W., Zhu, W., Srensen, N., and Srensen, N. (2011). Simulation of moving trailing edge flaps on a wind turbine blade using a navier-stokes based immersed boundary method. PhD thesis, dtu.

Berg, D. E., Wilson, D. G., Resor, B. R., Barone, M. F., and Berg, J. C. (2009). Active aerodynamic blade load control impacts on utility-scale wind turbines. FlexSys Inc., Ann Arbor, MI USA.

Bristow, Tharayil, and Alleyne (2006). A survey of iterative learning control. IEEE Control Systems, Volume:26, Issue: 3.

Buhl, T., Gaunaa, M., and Bak, C. (2005). Load reduction potential using aerofoils with variable trailing edge geometry. Journal of Solar Energy Engineering 127, p. 503-516.

Cai, Z. (2009). Iterative learning control: Algorithm development and experimental benchmarking. PhD thesis, University of Southampton.

Cesnik, C. (2009). Computational aeroelasticity of rotating wings with deformable airfoils. AHS International, the vertical flight society; 65th annual forum proceedings.

Chi, R., Hou, Z. and Xu, J. (2008). Adaptive ILC for a class of discrete-time systems with iteration-varying trajectory and random initial condition. Automatica. Volume 44, Issue 8, p. 2207-2213.

Chopra, I. (2002). Review of state of art of smart structures and integrated systems. AIAA Journal, Vol. 40, No. 11, p. 2145-2187.

Chopra, I. (2010). An examination of rotor loads due to on-blade active controls for performance enhancement using cfd/csd analysis. R. Jain, HyPerComp Inc.; H. Yeo, US Army AFDD.

Clarke, N. and Tutty, O. (1994). Construction and validation of a discrete vortex method for the two-dimensional incompressible navier-stokes equations. Computers Fluids, vol. 23, pp. 751-783.

Dieterich, O., Enenkl, and Roth, D. (2006). Trailing edge flaps for active rotor control aeroelastic characteristics of the adasys rotor system. Journal of aircraft. Vol.47, No.1.

Dimopoulos CA, Koulatsou K, Petrini F, Gantes CJ. (2015) Assessment of Stiffening Type of the Cutout in Tubular Wind Turbine Towers Under Artificial Dynamic Wind Actions. ASME. J. Comput. Nonlinear Dynamics.

Drella, M. XFOIL (1985). Harold Youngren, Aerocraft, Inc.

Eisele, O., Pechlivanoglou, F. P. G., Nayeri, C. N., and Paschereit, C. O. (2011). Experimental investigation of dynamic load control strategies using active microflaps on wind turbine blades. EWEA March 14.-17. 2011, Brussels, Belgium.

FlexSys, NASA, and Laboratory, U. R . (2012). Adaptive compliant trailing edge flight experiment. ACTE research.

Frederick, M., Kerrigan, E.C., Graham, J.M.R. (2010). Gust alleviation using rapidly deployed trailing-edge flaps. Journal of Wind Engineering and Industrial Aerodynamics, Volume 98, Issue 12, p. 712-723, ISSN 0167-6105.

Freeman, Lewin, and Rogers (2007). Further results on the experimental evaluation of iterative learning control algorithms for non-minimum phase plants. International Journal of Control, 80, (4), p. 569-582.

Garcia, N. R., Srensen, J. N., and Shen, W. Z. (2011). Quasi-3d aerodynamic code for analysing dynamic flap response. PhD thesis, Technical University of Denmark (DTU), Kgs. Lyngby, Denmark.

Gaunaa, M. (2006). Unsteady 2d potential flow forces on a thin variable geometry aerfoil undergoing arbitrary motion. Forskningscenter Risoe. Risoe-R; No. 1478 (EN).

Gaunna, M. and Andersen, P. B. (2009). Load reduction using pressure differences on an aerofoil for control of trailing edge flaps. European Wind Energy Conference and Exhibition.

Hand, M., Wright, A., Fingersh, L., and Harris, M. (2006). Advanced wind turbine controllers attenuate loads when upwind velocity measurements are inputs. 44th AIAA Aerospace Sciences Meeting and Exhibit, Aerospace Sciences Meetings.

Hansen, M. H., Gaunaa, M., and Madsen, A. H. (2004). A beddoes-leishman type dynamic stall model in state-space and indicial formulations. Forsknings center Risoe. Risoe-R; No. 1354.

Gomez-Iradi, S. and Barakos, G. N. (2008). Computational fluid dynamics investigation of some wind turbine rotor design parameters. UK Proceedings of the Institution of Mechanical Engineers, Part A: Journal of Power and Energy August 1, vol. 222 no. 5 p. 455-470

Gomez-Iradi, S. and Barakos, G. N. (2010). A CFD investigation of the near blade 3d bow for a complete wind turbine configuration. Proceedings of the 2012 ASEE North Central Section Conference.

Hernando, B.H., Martnez F. P., and Encabo, A. F. (2010). Wind Turbine Clutter, Radar Technology, Guy Kouemou (Ed.), InTech, DOI: 10.5772/7175.

Johnson, S. J., Case van Dam, C. P., and Berg, D. E. (2008). Active load control techniques for wind turbines. Sandia report: SAND2008-4809.

Johnston, C. (2003). Wings with conformal control surfaces for morphing aircraft. Journal of Aircraft, 40:1, p. 94-99.

Joncas, S., Bergsma, O., and Beukers, A. (2005). Power regulation and optimization of offshore wind turbines through trailing edge flap control. Proc. of the 43rd AIAA aerospace Science Meeting and Exhibit.

Kim, J. and Bewley, T. R. (2007). A linear systems approach to flow control. Annual Review of Fluid Mechanics. 39, p. 383-417.

Lackner, M. A., and Gijs van Kuik (2009). A comparison of smart rotor control approaches using trailing edge flaps and individual pitch control. 47th AIAA Aerospace Sciences Meeting including the New Horizons Forum and Aerospace Exposition, Orlando, Florida.

Lackner, M. A., and Gijs van Kuik (2010). The performance of wind turbine smart rotor control approaches during extreme loads. J. Sol. Energy Eng 132(1).

Lafountain, C., Cohen, K., and Abdallah, S. (2010). Use of xfoil in design of camber-controlled morphing UAVs. Computer Applications in Engineering Education. Volume 20, Issue 4, p. 673-680.

Larsen, J. W. (2007). Dynamic stall model for wind turbine aerofoils. Journal of Fluids and Structures. Volume 23, Issue 7, p. 959-982.

Luhur MR, Peinke JJ, Khn MM, Wchter MM. (2015) Stochastic Model for Aerodynamic Force Dynamics on Wind Turbine Blades in Unsteady Wind Inflow. ASME. J. Comput. Nonlinear Dynamics. doi:10.1115/1.4028963.

Potsdam, M., Fulton, M. V., and Dimanlig, A. (2010). Multidisciplinary CFD/CSD analysis of the smart active flap rotor. American Helicopter Society 66th Annual Forum, Phoenix, AZ.

MacDonald, M. (2010). Mott Macdonald Energy Review. DECC report June 2010.

Maheri, A. and Isikveren, A. T. (2009). Performance prediction of wind turbines utilising passive smart blades: Approaches and evaluation. Wind Energy. Volume 13, Issue 2-3, p255-265.

Marrant, B. and van Holten, T. (2006). Concept study of smart rotor blades for large offshore wind turbines. 47th AIAA Aerospace Sciences Meeting including the New Horizons Forum and Aerospace Exposition, Orlando, Florida.

Mateescu and Abdo (2003). Unsteady aerodynamic solutions for oscillating airfoils. 41st Aerospace Sciences Meeting and Exhibit. Reno, Nevada.

Ng, B. F., Palacios, R., Kerrigan, E. C., Graham, J. M. R., and Hesse, H. (2015a) Aerodynamic load control in horizontal axis wind turbines with combined aeroelastic tailoring and trailing-edge flaps. Wind Energ., 19: 243-263.

Ng, B. F., Hesse, H., Palacios, R., Graham, J. R., and Kerrigan, E. C. (2015b), Aeroservoelastic state-space vortex lattice modeling and load alleviation of wind turbine blades. Wind Energ., 18, p. 1317-1331.

PasupulatiS, V., Wallace J., and Dawson, M. (2005). Variable length blades wind turbine. IEEE Power Engineering Society General Meeting, p. 2097-2100 Vol. 3.

Peters, D. (2007). A state space airloads theory for flexible airfoils. Journal of the American Helicopter Society 52(4).

Peters, D. (2008). Two-dimensional incompressible unsteady aerofoil theory - an overview. Journal of Fluids and Structures. Volume 24, Issue 3, p. 295-313.

Politakis, G., Haans, W., and Bussel, G. (2008). 3d suppression of classical flutter using a smart blade. 46th AIAA Aerospace Sciences Meeting and Exhibit. Reno, Nevada

Port-Agel, F., Wu, Y.-T., Lu, H., and Conzemius, R. J. (2011). Large-eddy simulation of atmospheric boundary layer flow through wind turbines and wind farms. Journal of Wind Engineering and Industrial Aerodynamics, 99(4): p. 154-168.

R Steijl, M. W. and Barakos, G. (2010). CFD method for efficient analysis of rotors. Aeromechanics Meeting, San Francisco. AHS, p. 1.

Rice, J. and Verhaegen, M. (2010). Robust and distributed control of a smart blade. Wind Energy, Special Issue: Smart Blades, Volume 13, Issue 2-3, p. 103-116.

Saab, S. (2001). On a discrete-time stochastic learning control algorithm. IEEE Transactions on Automatic Control, vol. 46, no. 8, p. 1333-1336.

Saab, S. (2003). Stochastic p-type/d-type iterative learning control algorithms. International Journal of Control, Volume 76, Issue 2.

Sanders, Eastep, and Foster (2003). Aerodynamic and aeroelastic characteristics of wings with conformal control surfaces for morphing aircraft. Journal of Aircraft, Vol. 40, No. 1, p. 94-99.

Spentzos, A., Barakos G. N., Badcock K., Richards B. E., Wernert P., Schreck S., and Raffel M. Investigation of Three-Dimensional Dynamic Stall Using Computational Fluid Dynamics. AIAA Journal, Vol. 43, No. 5, p. 1023-1033.

Sorensen, N. (2010). CFD applications in wind energy. CFD for atmospheric flows and wind engineering. Von Karman Institute for Fluid Dynamics.

Stanewsky, E. (2001). Adaptive wing and flow control technology. Progress in Aerospace Sciences. Volume 37, Issue 7, p. 583-667.

Straub, F. K. (1996). A feasibility study of using smart materials for rotor control. Smart Materials and Structures, Vol 12, Issue 4.

Sutherland, H. J. and Mandell, J. F. (2004). The effect of mean stress on damage predictions for spectral loading of fiberglass composite coupons. EWEA, Special Topic Conference 2004: The Science of Making Torque from the Wind, Delft, p. 546-555.

Theodorsen, T. (1935). General theory of aerodynamic instability and the mechanisms of flutter.

Thomsen, S. C., Niemann, H., and Poulsen, N. K. (2008). Individual pitch control of wind turbines using local inflow measurements. Proceedings of the 17th World Congress, The International Federation of Automatic Control, Seoul, Korea. Rotor embedded actuator control technology.

Tutty, O., Blackwell, M., Rogers, E., and Sandberg, R. (2013). Iterative learning control for improved aerodynamic load performance of wind turbines with smart rotors. IEEE Transactions on Control Systems Technology.

Van der Wall, B. G. (1999). Experimental and numerical investigations on steady and unsteady behaviour of a rotor aerofoil with a piezoelectric trailing edge flap. American Helicopter Society 55th Annual Forum, Montreal, Canada.

Wang, N., Johnson, K. E., and Wright, A. D. (2012). Fx-rls-based feedforward control for lidar-enabled wind turbine load mitigation. Control Systems Technology, IEEE Trans- actions, Volume: 20, Issue: 5.

Wright, A. D. (2004). Modern control design for flexible wind turbines. NREL technical report: NREL/TP-500-35816.